Dissertation

submitted to the

Combined Faculty of Mathematics, Engineering and Natural Science

of Heidelberg University, Germany

for the degree of

Doctor of Natural Sciences

Put forward by

Daniel Ryklin

born in: Moscow

Oral examination: 9th of July, 2024

# bsEELS:

# A new method for

# Electron Energy Loss Spectroscopy

# on backscattered electrons inside a

# Scanning Electron Microscope.

Referees: Prof. Dr. Rasmus R. Schröder

Prof Dr. Wolfram Pernice

**bsEELS: Ein neue Methode zur Elektronen Energieverlust Spektroskopie in einen Rasterelektronenmikroskop.**

In dieser Doktorarbeit stelle ich eine neue Methode der Elektronen Energieverlust-Spektroskopie (EELS) an rückgestreuten Elektronen (RE) in einem Rasterelektronen Mikroskop (REM) vor, die wir "backscattered EELS" (bsEELS) nennen. Energieverlust-Spektren der RE werden bei extrem niedrigen Primärenergien bis zu 10 eV bei 1 nm Ortsauflösung aufgenommen. Das ermöglicht die abbildende spektroskopische Untersuchung großer Flächen von dicken Proben bei der die Signalinformation auf nur wenige Nanometer der Proben-Oberfläche limitiert ist. Dadurch können die Einschränkungen etablierter Methoden wie (Raster-)Transmissionselektronen Mikroskopie ((R)TEM) EELS und "high resolution" / Rückstreu (HR-/R-) EELS überbrückt und ergänzt werden. Die experimentellen Ergebnisse von unterschiedlichen nicht-organischen, Kohlenstoff- und organischen Materialien zeigen, dass bsEELS insbesondere geeignet ist den Bereich des niedrigen Energieverlustes mit Anregungen von Oberflächenplasmonen und Leitungsband Elektronen abzubilden. Derzeit ist die Methode vorwiegend durch mangelnde Energieauflösung eingeschränkt, die von dem gebeugten Strahlengang zum Gegenfeld Gitter-Spektrometer verursacht wird. Ein vorwärts Faltungs-Modell wird angewendet, um die experimentellen Daten zu interpretieren und mit spektroskopischen Referenzdaten (von UV-Vis, TEM EELS, HREELS) zu vergleichen. Schließlich werden Verbesserungen des derzeitigen Experiments diskutiert um in Zukunft hochaufgelöste bsEEL Spektren aufnehmen zu können.

**bsEELS: A new method for Electron Energy Loss Spectroscopy on backscattered electrons inside a Scanning Electron Microscope.**

In this doctoral thesis I introduce the novel approach of performing electron energy loss spectroscopy (EELS) on backscattered electrons (BSE) inside a scanning electron microscope (SEM), which we call backscattered EELS (bsEELS). EEL spectra from BSE are acquired at ultra-low primary electron energy down to 10 eV with 1 nm spatial resolution. This allows large area spectroscopic imaging studies on bulk materials with surface signal information confined to few nanometers, thereby complimenting and bridging the limitations of established (scanning) transmission electron microscopy ((S)TEM-) EELS and high resolution / reflective (HR/R-) EELS methods. The experimental data from a variety of inorganic, carbon, and organic materials prove that bsEELS is in particular suited to access the low-loss energy regime containing primarily surface plasmon and conduction band excitations. Current limitations concerning the energy resolution caused by energy spreading on the bent beam path towards a retarding grid potential spectrometer are discussed in detail. A forward convolution model is established to interpret the experimental data with respect to spectroscopic reference measurements (UV-Vis, TEM EELS, HREELS). Finally, improvements of the current experimental design are discussed to access high-resolution spectral information with bsEELS in the future.

# Contents


I Introduction and Motivation 10

1 Overview on High Resolution Characterization Methods 11

2 Is there a Need for another Electron Spectroscopic Approach? 13

3 Content and Outline of this Thesis 16

II Physical Background, Methods and Materials 18

4 Theoretical Background for Signal Generation in the SEM 19
4.1 Overview . . . . . . . . . . . . . . . . . . . . . . . . . . . . . . . . . 19
4.2 Backscattered Electrons . . . . . . . . . . . . . . . . . . . . . . . . . 20
4.2.1 Backscattering Coefficient . . . . . . . . . . . . . . . . . . . . 20
4.2.2 Interaction Volume and Electron Range . . . . . . . . . . . . . 23
4.2.3 Mean Energy of BSE . . . . . . . . . . . . . . . . . . . . . . . 25
4.2.4 Contrast Mechanisms . . . . . . . . . . . . . . . . . . . . . . . 26
4.3 Beam Damage, Charging, and Contamination . . . . . . . . . . . . . 27

5 Scanning Electron Microscopy 30
5.1 Overview on the Current State of SEM Applications . . . . . . . . . . 30
5.2 DELTA SEM . . . . . . . . . . . . . . . . . . . . . . . . . . . . . . . 32
5.3 Data Acquisition . . . . . . . . . . . . . . . . . . . . . . . . . . . . . 34

6 Samples and Evaluation Methods 37
6.1 Samples and Sample Preparations . . . . . . . . . . . . . . . . . . . . 37
6.1.1 Polycrystalline Gold . . . . . . . . . . . . . . . . . . . . . . . 37
6.1.2 Flat DNA Origami Platelets . . . . . . . . . . . . . . . . . . . 37
6.1.3 Exfoliated Graphene . . . . . . . . . . . . . . . . . . . . . . . 38
6.1.4 Printed Structure Containing Quantum Dots . . . . . . . . . . 38
6.1.5 Graphitized Cellulose Paper . . . . . . . . . . . . . . . . . . . 39
6.1.6 Tetra-Phenyl Cumulenes . . . . . . . . . . . . . . . . . . . . . 39
6.1.7 Polymere Microspheres . . . . . . . . . . . . . . . . . . . . . . 39
6.1.8 Printed PETA Structures with Fluorophores . . . . . . . . . . 40

6.2 Data Evaluation and Scripts . . . 40
6.2.1 Fluorescence Survival Rate Evaluation . . . 40
6.2.2 Protocol to Obtain bsEELS Spectra out of Image Raw Data . 41
6.2.3 Convolution Fit Procedure . . . 42

III Approaching Spectral Imaging with Ultra-Low Voltage SEM 43

7 Signal Collection of the Microscope Detectors 44

8 Challenges and Opportunities of Imaging at Ultra-Low Voltage 48
8.1 Handling Surface Contamination . . . 48
8.2 Examples of Unexpected Image Contrast and Surface Sensitivity . . . 52
8.2.1 Polycrystalline Gold . . . 52
8.2.2 Flat DNA Origami Platelets . . . 54
8.2.3 Graphene . . . 56
8.2.4 Summary of the ULV Imaging Observations . . . 58
8.3 Beam damage . . . 59

9 Spectroscopy with the Delta Detector 62
9.1 Energy Resolution and Energy Spread Function . . . 62
9.2 Ratio and Distinction of Backscattered and Secondary Electrons . . . 66
9.3 Backscattered EELS Spectra and the Energy Spread Function . . . 70

IV Experimental Results 74

10 Inorganic Samples 75
10.1 Polycrystalline Gold . . . 75
10.2 Qunatum Dot Fluorophores . . . 78

11 Carbon Materials 82
11.1 Graphene . . . 82
11.2 Graphitized Cellulose Paper . . . 89

12 Organic Samples 92
12.1 DNA and Fluorophores . . . 92
12.2 Tetra-Phenyl Cumulenes [3]PH and [5]PH . . . 101
12.3 Polymere Microspheres . . . 104
12.3.1 bsEELS . . . 104
12.3.2 Surface Charge Mapping with Secondary Electrons . . . 107

V Conclusion and Outlook 111

13 Summary, further Discussion and Conclusion 112

14 Outlook 120
14.1 Improvement of the Experimental Procedure . . . 120
14.2 Detector Update and Implementation of Neural Network for Data Analysis . . . 122

VI Appendix 125

A Figures 126

B Tables 129

C Scripts for Data Evaluation 131
C.1 Export Image Stack from Matlab File . . . 131
C.2 Replace Image Stack from Matlab File with Aligned Image Stack . . . 133
C.3 Export the Averaged Spectrum by Means of the Mapped Regions in the Mask-Files . . . 134
C.4 Script for the Convolution Fit . . . 136

D Lists 138
D.1 List of Figures . . . 138
D.2 List of Tables . . . 147

E Publications Including the Author of this Thesis 148

F Bibliography 151

G Acknowledgements 165

# Part I

# Introduction and Motivation

In the first part of this thesis I will discuss the topical context for this work and motivate the approach of developing a new characterization method in the field of electron energy loss spectroscopy (EELS). Further I will explain the outline of this thesis together with a list of acronyms and abbreviations.

# 1 Overview on High Resolution Characterization Methods

Characterization of materials is essential to understand physical and chemical properties and to drive material research and development in a meaningful and predictable way. I want to differentiate here between macroscopic methods on one hand, like UV/Vis or Raman spectroscopy, which give detailed insight into the electrochemical and atomic structure of a material or composite, however, with no – or very limited – spatial resolution and therefore are mainly applicable to homogeneous materials. On the other hand there are microscopic methods, which in the first instance are developed to give insight into the arrangement of different materials in a system, or they even determine the spatial arrangement of atoms in a material or material system. Since this work is about the development and application of a new microscopic method, I want to focus in this chapter on the current state of microscopic characterization.

Scientific breakthroughs often went hand in hand with the successful visualization of structures and objects, and light microscopy (LM) was of course historically the first method to lead the way. LM can visualize almost every material and structure by amplitude (absorption or scattering) contrast and/or phase contrast, however, it is limited in resolution by the Abbe limit. By implementing spectroscopy, LM can also measure properties such as specific absorption and fluorescence, which give insights into the electronic structure of the material. Fluorescence imaging (FM) also allows to 'overcome' the Abbe limit and achieve nominal resolutions down to pinpointing of single molecules with so called super-resolution microscopy (Schermelleh et al. [2019]). This high resolution is limited to fluorescent molecules which have suitable properties (excitation energy, lifetime of excited state, quenching, on/off switching, etc.) and structures which can bind these fluorescent labels.
With electron microscopy (EM) Ångstrom resolution can be achieved using amplitude and phase contrast as well as diffraction which allows to study the atomic composition of materials and structures. Electron energy loss spectroscopy (EELS) opens up the opportunity to combine this sub-atomic spatial resolution with characteristic material information similar to X-ray, UV-Vis and IR spectroscopy (Kim et al. [2023]). Modern scanning transmission electron microscopes (STEM) enable elemental and bond mapping with atomic resolution by measuring core-loss spectra at hundreds of electronvolt energy loss as well as surface plasmons and nanoplasmonics of (nano)materials in the range of tens of electronvolt (Colliex [2011]). But also low-loss, 10 meV to 100 meV excitations like phonons, excitons, and valence structures are accessible with high resolution EELS at atomic resolution (Hage et al.

[2020]), as well as short range order signals out to 12 keV at nanometer resolution with high energy EELS (Hart et al. [2023]). So (S)TEM EELS covers a large energy range for spectroscopy enabling studies and characterizations on a large variety of materials and structures.
X-ray characterization techniques are probably the main competitors of EM studies, as they have comparable approaches for characterization: X-ray diffraction versus electron diffraction, X-ray absorption spectroscopy versus EELS, X-ray fluorescence versus energy-dispersive X-ray spectrometry. The main disadvantages of EM against X-ray studies are the requirement for vacuum compatible samples, which strongly limits the use of in situ environment setups and the need for rather complex and often sophisticated sample preparation (like preparation of $< 100$ nm thick lamella) due to the low penetration depth of electrons (Mino et al. [2018]). EM probes currently still have better resolution compared to X-ray nanoprobes, however, if the current trend in improvement of X-ray lenses continues, future X-ray nanoprobes will include focusing devices with resolution better than 1 nm (Yan and Chu [2012], Mino et al. [2018]). X-ray absorption spectroscopy reveals the near edge structure, according to which chemical properties and the electronic structure of the matter can be determined, and fine structure containing the local structure of the materials or devices. Since vacuum is not neccessarily required for X-ray imaging, it is particularly suitable for organic and biological studies (Mino et al. [2018]).
In addition to better spatial resolution, EELS has the advantage that it can directly access the low-loss energy regime containing information on the electronic and energetic structure of the material system such as plasmon excitations and molecular interactions.
For completeness I want to mention ion and neutron microscopy as method for characterization. However, the application range for these methods is rather limited due to higher disruptiveness to samples and lower resolution for these probes, therefore, I will not go into more detail here.

# 2 Is there a Need for another Electron Spectroscopic Approach?

In the previous chapter I have given a short overview on different methods for high resolution material characterization and pointed out that with all improvements in all the different approaches, EM studies still have important advantages and will definitely contribute in various research areas going forward. But is there a need for another approach for electron spectroscopic studies? In this chapter I want to motivate our development of backscattered electron energy loss spectroscopy – the application and characterization of which is topic of this doctoral thesis.

One weakness of (S)TEM studies – especially for light atom (organic and biological) materials – is the beam damage induced by the high energy electrons (typically around 200 keV) leading to bond breaking and knock on damage (Egerton et al. [2004]). One approach to reduce the beam damage is to reduce the electron energy, which, however, requires dedicated instrumentation to correct for spherical and chromatic aberrations at these lower energies. The SALVE project, for instance, has implemented newly developed correctors in order to achieve atomic resolution TEM imaging from 20 keV to 80 keV reducing the knock on damage induced by the electrons (Linck et al. [2016]). Reducing the electron energy, however, runs into problems, since the mean free path decreases as well and samples need to be further thinned for TEM studies. At 20 keV to 80 keV the mean free inelastic path is about 20 nm to 70 nm in carbon (Burge and Misell [1968]). Below 3 keV electron energy the inelastic mean free path is smaller than 5 nm in carbon and other organic structures (Arakawa et al. [1985]). This restricts TEM studies at low energies to thin (well below 100 nm) material layers.
But even for sufficiently thin(ned) samples, the study of samples or devices with layered or mixed materials is problematic, since transmission images are always a projection through the sample. For homogenous single materials or atomic layers forming 2D materials, this is not a problem, since the projection does not mix signals from different materials, as it is illustrated in figure 2.1 a). For bulk material mixtures the projection causes signal mixing of overlapping material domains, so that the materials can not be distinguished anymore (figure 2.1 b)). This problem could in principle be overcome by recording a tomogram of the bulk material, this, however, severely increases the electron dose and introduces more beam damage.

If we change the setup from transmission to scanning electron microscopy (SEM), we gain two advantages: Firstly, we are no longer limited by the sample thickness and therewith, secondly, we now are able to further reduce the electron energy. Standard SEMs operate at 2 keV to 20 keV. At these energies the range or penetration

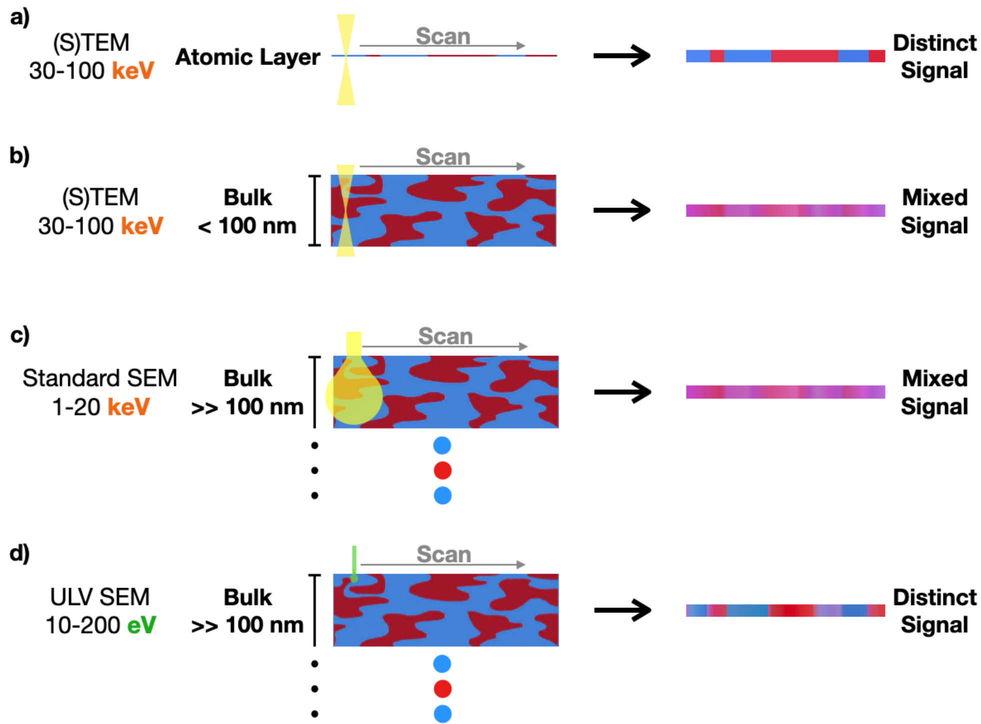


Figure 2.1: Illustration of the signal mixing when imaging bulk material mixtures with different TEM and SEM methods. a) (S)TEM imaging of atomic layers introduces no signal mixing and produces a distinct atomic resolution signal. b) Bulk material mixtures need to be thinned below 100 nm and the projection though the sample leads to mixing of the signal from overlapping areas. c) For Standard SEM energies the interaction volume due to multiple scattering is still large in order of tens to hundreds of nanometer leading to signal mixing if the domains are smaller. d) With ultra-low voltage (ULV) SEM the interaction volume decreases to nanometer size, allowing to distinguish material domains at the surface down to nanometer resolution.

depth of the electrons is still relatively large, i.e. $10\,\mu g\,cm^{-2}$ to $90\,\mu g\,cm^{-2}$ for 1 keV to 5 keV electrons which corresponds to a path length of about 40 nm to 400 nm in carbon (Böngeler et al. [1993]). If now the domains of a mixed material are smaller than the interaction volume, still a mixed signal will be measured in a SEM setup which is illustrated in figure 2.1 c). If the electron energy is now further reduced to 10 eV to 200 eV – to which we refer to as ultra-low voltage (ULV) SEM – the interaction volume shrinks to nanometer range and the surface domains of a material mixture can again be distinguished with that resolution (figure 2.1 d)). This enables high resolution analytical surface characterization of bulk materials. But can a spectroscopic analysis be implemented to this approach, analogous to EELS in the TEM?

At this point it is worth to mention, that reflective EELS (Wang and Cowley [1988]) and HR EELS (Ibach and Rajeswari [2012]) are well established surface sensitive electron spectroscopic methods, however, with no spatial resolution, which makes them only applicable to wide-spread, homogeneous films.
Up to now, SEM is mostly used 'only' for imaging, usually generating material contrast with backscattered electrons (BSE) caused by different backscattering coefficients from different atoms, or topographical contrast with secondary electrons (SE). Quantitative spectroscopic applications in the SEM are limited to secondary signals, e.g. electron-dispersive X-ray spectroscopy (EDX) and cathodoluminescence (CL). Spectroscopy on electrons in the SEM is so far limited to secondary electrons (e.g. Kazemian et al. [2007]), and was also successfully applied at ULV with the prototype instrument (DELTA SEM - which is used in this doctoral thesis) to reveal nanoscale surface morphology of functional organic blends (Kammerer et al. [2018]), or surface potentials (Zhang et al. [2021]).

Our goal is to perform electron energy loss spectroscopy on backscattered electrons in the ULV SEM. As forward scattered electrons in (S)TEM EELS experiments, BSE can undergo multiple elastic (no energy loss -> zero-loss peak) and inelastic (-> energy loss spectrum with characteristic peaks) scattering events. The momentum transfer is thereby very different for BSE (up to $180^\circ$) compared to transmitted electrons ($\approx 0^\circ$) which has influence on the cross-sections for the different elastic and inelastic scattering events (Kuhr and Fitting [1999]). This might lead to interesting physics such as backscattering on 2D materials with 'simultaneous' elastic/inelastic scattering on one atomic layer.
bsEELS will enable large area EELS analysis on bulk materials while using the strength of SEM with nanometer spatial resolution and surface sensitivity and thereby bridging the limitations of TEM and HREELS measurements and expanding the application of EELS with high spatial resolution.
A physical background to low energy imaging in the SEM will be given in Part II of this work, further discussing the possible advantages and disadvantages of performing EELS on backscattered electrons in the SEM in more detail. In the results and discussion parts IV and V I will show that we succeeded to develop backscattered EELS (bsEELS) in our ULVSEM. This is a great breakthrough in the field of material and sample characterization and expands the experimental application range of electron probe studies. We believe bsEELS has the potential to become a powerful characterization method, especially for organic and biological samples, complementing the current possibilities of material characterization with electrons and elsewise.

# 3 Content and Outline of this Thesis

For this thesis, I worked with a SEM prototype developed by Carl Zeiss Microscopy (Oberkochen, Germany) - the DELTA. It was originally constructed for high resolution imaging of beam sensitive samples at ultra-low electron beam energies down to 10 eV. In order to study the spectral electron signal in this ULVSEM, a retarding potential spectrometer was added to the detector setup. Instrument and project was funded by the BMBF grant ‘MorphiQuant-3D’ to the advisor of this thesis, Prof. Dr. Rasmus R. Schröder.
Since this represents a completely new approach, a significant portion of this work was dedicated to characterize and understand the detected signal. Therefore, a large spectrum of different materials and material systems were studied to explore the suitability for different applications and – even more importantly – to scan a wide parameter space to understand the microscope and detector characteristics.
Part II of this thesis will introduce the physical background for low energy electron microscopy and describe the used materials and methods for this work.
In Part III, I will explain the detector and microscope characteristics and properties which came out of experiments on different samples, introduce the complexities but also possibilities which arise with bsEELS experiments with this setup.
Part IV will contain all results of the performed bsEELS experiments divided in three material classes together with short discussions of the presented results. In the last Part V, I will bring all experiments together to put them into context and further discuss the collective results. Afterwards, I will formulate the conclusions of my thesis and give an outlook on possible instrumental improvements, possible future experiments and the future of bsEELS.

Table 3.1: List of acronyms and abbreviations.

| Acronym/Abbreviation | Meaning |
|---|---|
| ANN | Artificial Neural Network |
| AT | Array Tomography |
| BSE | Backscattered Electron |
| CL | Cathodoluminescence |
| CNN | Convolutional Neural Network |
| DD | DELTA Detector |
| EDX | Electron-Dispersive X-ray spectroscopy |
| EELS | Electron Energy Loss Spectroscopy |
| EM | Electron Microscopy |
| ESF | Energy Spread Function |
| FEG | Field Emission Gun |
| HREELS | High Resolution EELS |
| LLE | Low-Loss Electrons |
| LM | Light Microscope |
| LVSEM | Low Voltage SEM |
| MAG | Magnification of the microscope |
| PE | Primary Energy |
| SE | Secondary Electron |
| SEM | Scanning Electron Microscope |
| SNR | Signal to Noise Ration |
| SpS | Scans per energy Step (of the DD) |
| STEM | Scanning Transmission Electron Microscope |
| TEM | Transmission Electron Microscope |
| ULVSEM | Ultra-low Voltage SEM |
| UHV | Ultra High Vacuum ($<10^{-8}$ mbar) |
| WD | Working Distance |

# Part II

# Physical Background, Methods and Materials

# 4 Theoretical Background for Signal Generation in the SEM

## 4.1 Overview

Figure 4.1 illustrates the different types of interaction generating the signal in the SEM. Per definition of Seiler [1983], all generated electrons with an energy below

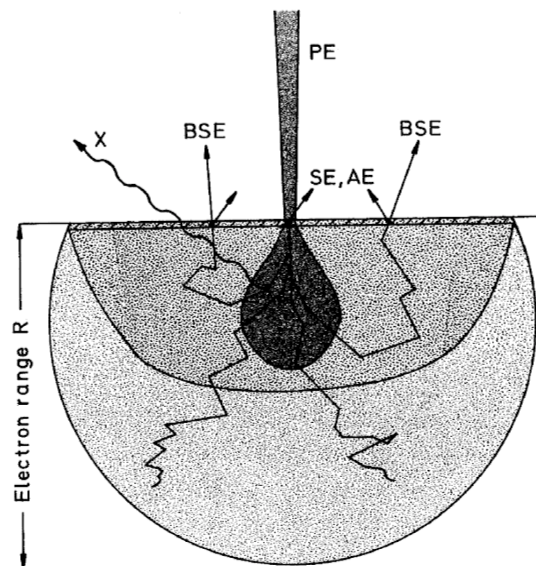


Figure 4.1: Interaction of the electron probe with the sample in the SEM, generating secondary electrons (SE), backscattered electrons (BSE), and Photons (X). Hawkes and Reimer [2013]

50 eV are called secondary electrons[1]. They are usually generated through interaction of the primary beam electrons with the electrons in the sample. Typically a cascade of electrons is released by the interaction, but only SEs generated close to the sample surface (5 nm to 15 nm in most materials Joy [1991]) can overcome the surface potential and leave the sample. Therefore most detected SEs come from the incident point of the beam (generally denoted as SE1). Secondary electrons, generated by a backscattered electron leaving the sample, can also come from regions

[1]With ULVSEM, this definition is not valid, since also BSE can be generated below 50 eV. In addition, charging can shift the SE signal to energies above 50 eV, as shown in the results in section 9.2

further away from the incident point (SE2).
In addition, photons and Auger electrons are generated from the beam interaction with the sample. Auger electrons are electrons emitted with a characteristic energy by an atom, when an inner shell vacancy of the atom is filled by an electron of an outer shell. Figure 4.2 shows a typical electron spectrum generated in a SEM.
I will focus on the signal of backscattered electrons in my work and I will go into more detail about their generation and properties in the following section.

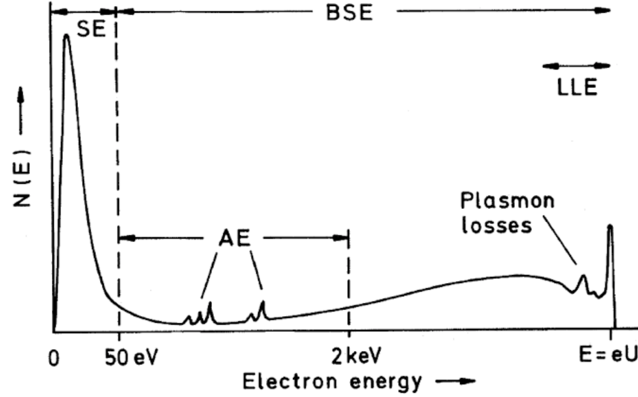


Figure 4.2: Electron spectrum generated in a SEM. SE: secondary electrons, AE: auger electrons, BSE: backscattered electrons, LLE: low-loss electrons. Hawkes and Reimer [2013]

## 4.2 Backscattered Electrons

### 4.2.1 Backscattering Coefficient

Backscattered electrons result from high angle scattering interactions of the incident primary beam electrons with a nucleus in the specimen. The backscattering coefficient (BSC) is defined as

$$\eta = \frac{I_r}{I_0}, \tag{4.1}$$

where $I_r$ ist the intensity of electrons scattered with an angle $\theta > 90°$ and $I_0$ is the incident electron intensity (Niedrig [1978]). Elastic backscattering can well be described by the first Born approximation of the Rutherford scattering cross section:

$$\left(\frac{\mathrm{d}\sigma}{\mathrm{d}\Omega}\right)_{RU} = \frac{Z^2}{64\pi^4 a_H^2}\left(\frac{\lambda}{\sin\frac{\theta}{2}}\right)^4, \tag{4.2}$$

with the solid angle $\Omega$, atomic number $Z$, Bohr radius $a_H = 0.0529\,\mathrm{nm}$, wavelength $\lambda$ and scattering angle $\theta$. When the sample thickness is smaller than $R/2$, $R$ being the

range of the electrons in the sample, single scattering can be assumed as predominant and the scattering intensity can be described as (Niedrig [1978])

$$\left(\frac{\mathrm{d}I}{\mathrm{d}\Omega}\right) = I_0 N_A D \left(\frac{\mathrm{d}\sigma}{\mathrm{d}\Omega}\right), \tag{4.3}$$

where $N_A$ is the number of Atoms in a unit volume and $D$ the sample thickness. Inserting the Rutherford cross section and integration over the backward half space gives the BSC

$$\eta = 2\pi N_A D \int\limits_{\theta>\pi/2}^{\pi} \left(\frac{\mathrm{d}\sigma}{\mathrm{d}\Omega}\right) \sin\theta \mathrm{d}\theta = \frac{\lambda^4}{16\pi^3 a_H^2} N_A Z^2 D. \tag{4.4}$$

For samples with thickness $D \gg R/2$ multiple scattering becomes important and the BSC $\eta_\infty$ for the bulk material has to be considered rather than that for a single atom. Still referring to Niedrig [1978],

$$\eta_\infty(\alpha) = \frac{1}{(1+\cos\alpha)^{9/\sqrt{Z}}} \tag{4.5}$$

with $\alpha$ being the incidence angle of the primary beam, describes experimental data quite well, however for primary energies above 10 keV only.

For energies below 10 keV Hawkes and Reimer [2013] amongst others have shown

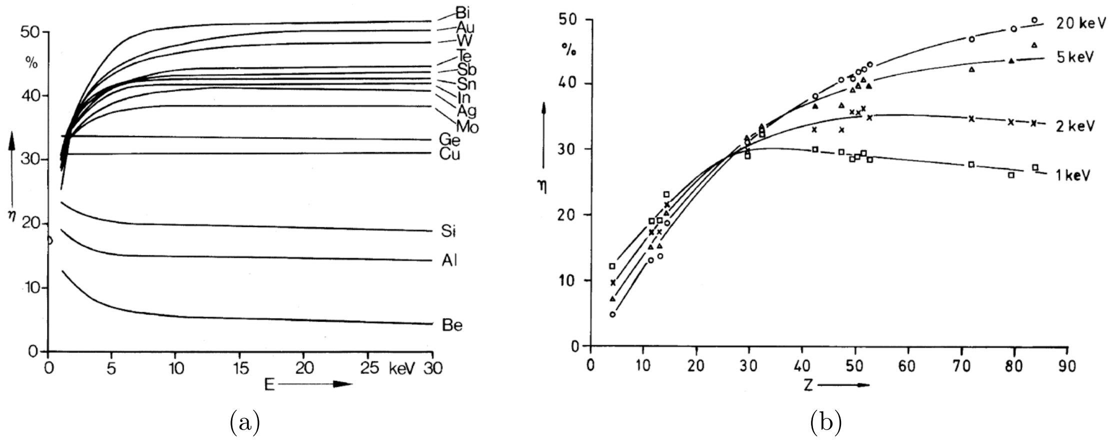


Figure 4.3: Backscattering coefficient as a function of (a) energy for different materials, (b) atomic number for different primary energies. Hawkes and Reimer [2013]

that the backscattering coefficient is strongly energy dependent, as shown in figure 4.3. The BSC decreases with lower energies for heavier materials and increases with lower energies for lighter materials.

Cazaux [2012] has stated an empirical expression to describe the experimental results on the backscattering coefficient at low energies:

$$\eta = a[1\,(\pm)\,e^{-bE^0}], \tag{4.6}$$

where $E^0$ is the incident electron energy and $a$ and $b$ are fit parameters. The sign '+' is for low-Z and '−' for high-Z elements. The fitted models to experimental references for carbon, silicon and gold are shown in figure 4.4. While it becomes clear that the

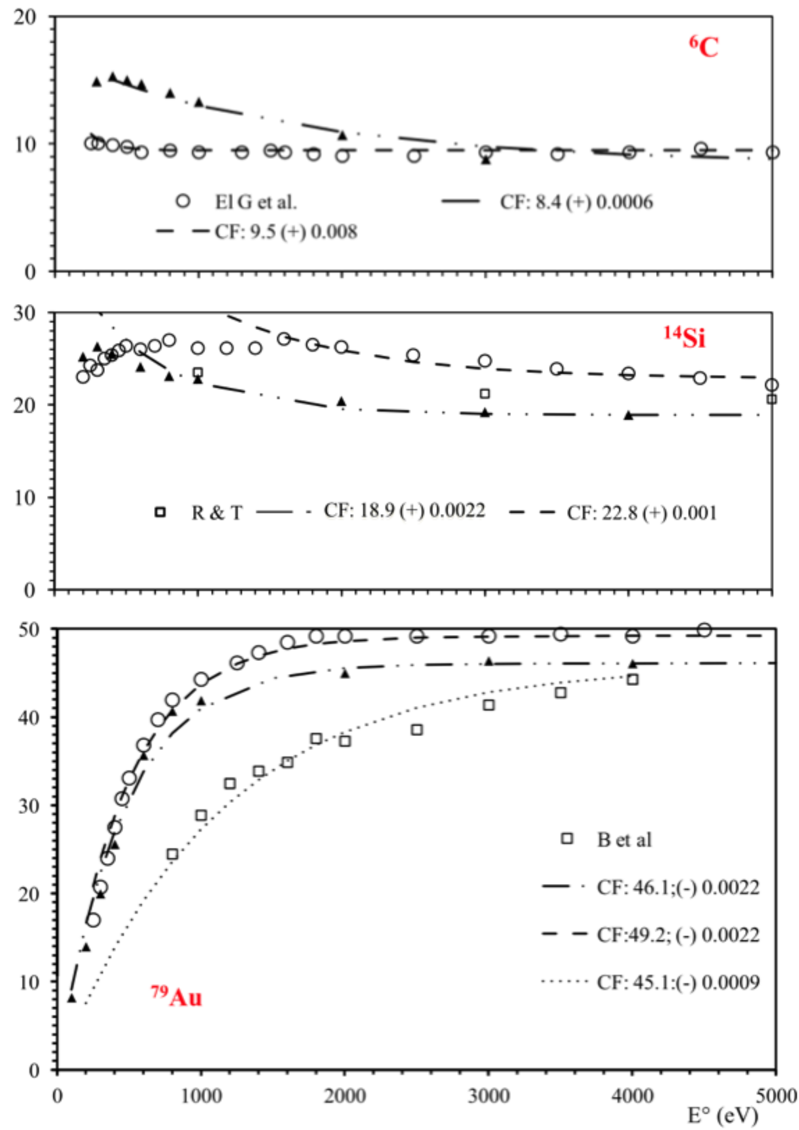


Figure 4.4: Backscattering coefficient fitted for several experimental references versus primary electron energy for carbon, silicon and gold from Cazaux [2012].

shown experimental references in the plots differ quite significantly from one another

– which Cazaux [2012] attributes to different states of oxidation and contamination – the model describes the relation of the BSC to the primary energy well. We can note here that the BSC for silicon increases with decreasing electron energy and is about twice as high compared to carbon even at lowest electron energies. The BSC of gold decreases drastically at lowest primary energy and becomes approximately equal to the BSC of carbon. The experimental results in this work will confirm this contrast relations in the BSE images of these materials (see section 11.1).

### 4.2.2 Interaction Volume and Electron Range

Electrons can be backscattered without any further interaction and loss of energy (zero-loss BSE), or undergo inelastic interactions on their way through the specimen and are therefore detected with an energy smaller than their primary energy, as shown in figure 4.5.

The range that electrons of energy $E$ can travel along a trajectory $s$ in the sample

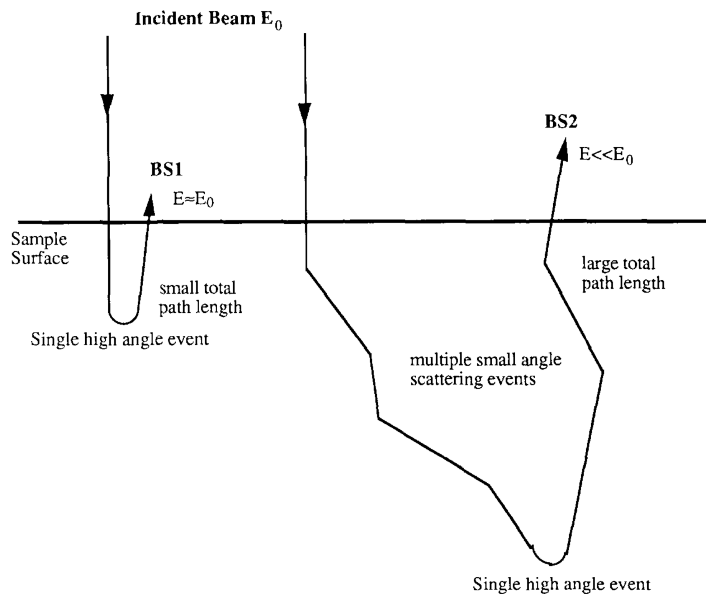


Figure 4.5: Origin of zero-loss BSEs (BS1) and BSEs with energy loss (BS2). Joy [1991]

depends on the stopping power $\frac{\mathrm{d}E}{\mathrm{d}s}$ of the sample. A convenient measure is the Bethe range

$$R_B = \int_{E_{min}}^{E_0} \frac{1}{-\frac{\mathrm{d}E}{\mathrm{d}s}} \mathrm{d}E, \tag{4.7}$$

where $E_0$ is the primary energy and $E_{min}$ a suitable lower energy limit for the integration (Joy and Joy [1996]). The stopping power for charged particles passing

through matter was first described by Bethe [1930] in the form of

$$\frac{\mathrm{d}E}{\mathrm{d}s} = -785\frac{\rho Z}{AE}\ln\left(\frac{1,166E}{J}\right)\mathrm{eV\,\mathring{A}}^{-1}. \tag{4.8}$$

$\rho$ is the density in $\mathrm{g\,cm^{-3}}$, $Z$ is the atomic number, $A$ is the atomic weight, and $J$ is the mean ionization potential of the material in eV.
According to Joy and Luo [1989], equation 4.8 describes the stopping power well for high electron energies. If the incident energy becomes $E \approx 5J$ or lower, which is in the range of 1 eV to 3 eV for most materials, equation 4.8 does not apply anymore. A more general form of the Bethe equation is

$$\frac{\mathrm{d}E}{\mathrm{d}s} = -785\frac{\rho Z}{AE}\sum_{n,l}\frac{f_{n,l}}{Z}\ln\left(\frac{2E}{A_{n,l}}\right), \tag{4.9}$$

where the target atom's $l$-th shell contains $n$ electrons, $f_{n,l}$ is the oscillator strength and $A_{n,l}/2$ is the ionization energy of the shell. This expression shows that the stopping power is a sum of core ionization, plasmon, and conduction electron excitations.
Starting from equation 4.9, Joy and Pawley [1992] performed Monte Carlo simulations of electron scattering in different materials and for different energies, exemplary shown in figure 4.6 for carbon. Since the stopping power rises with decreasing energy

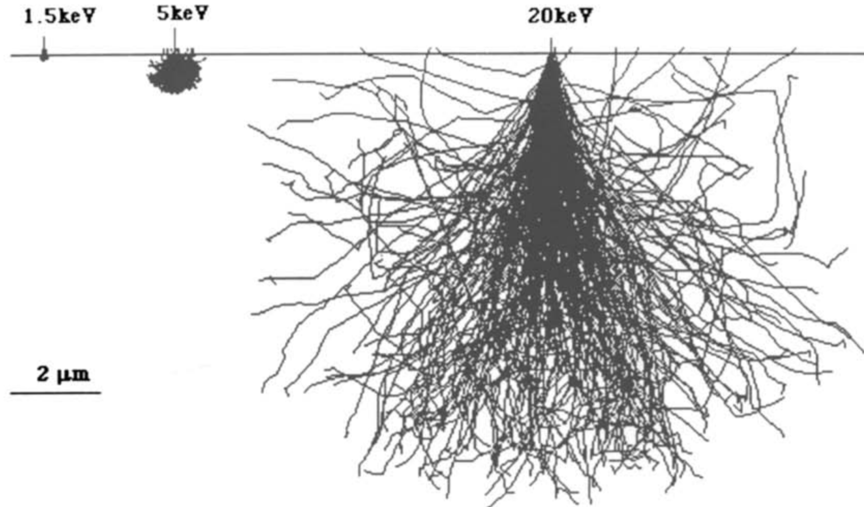


Figure 4.6: Monte Carlo plots of electron scattering in carbon at nominal density of $1\,\mathrm{g\,cm^{-3}}$ and for beam energies 1.5 keV, 5 keV and 20 keV. Joy and Pawley [1992]

of the electrons, as figure 4.7 (a) shows, the range of the electrons in the sample falls rapidly with lower beam energies down to tens of nanometers at energies below 1 keV, as shown in figure 4.7 (b). At energies of about 100 eV, electrons in all

materials have approximately the same range of about 10 nm - staying constant for even lower energies - since the stopping power has it's maximum at about 100 eV for most materials (Joy and Joy [1996]). Most of the BSE signal emerges from $\sim 0.2R_B$, which is only a few nanometer for low electron energies.

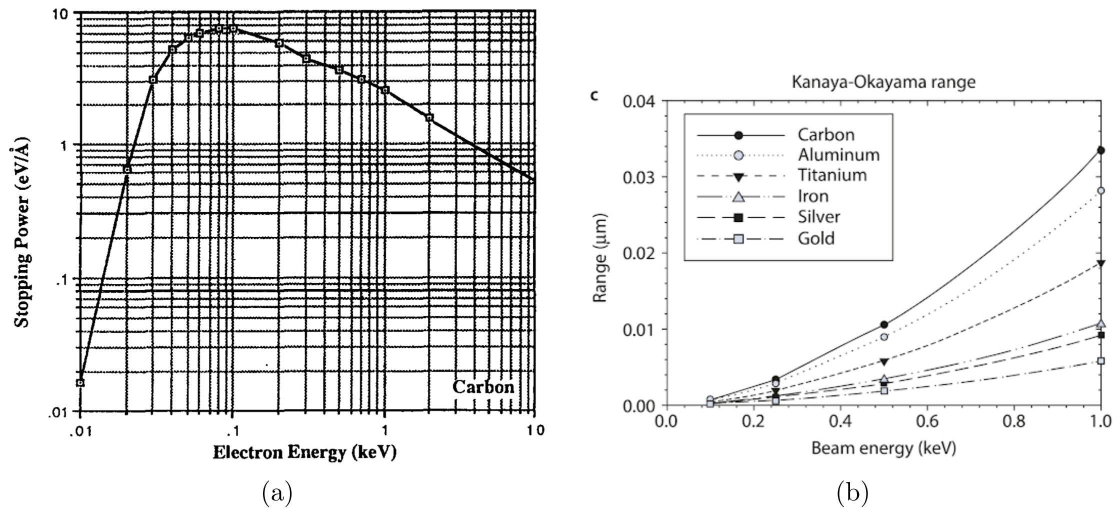


(a) (b)

Figure 4.7: (a) Stopping power variation as a function of energy for an electron traveling through carbon. Joy and Joy [1996] (b) Variation of electron range as a function of energy. Goldstein et al. [2017]

### 4.2.3 Mean Energy of BSE

As is implied in equation 4.9, core ionizations, plasmon losses and conduction electron excitations contribute to the energy loss of the incident electrons leading to a limited energy distribution of the inelastically scattered electrons. Of course, backscattered electrons leaving the sample can have undergone an inelastic scattering process as well, so that the BSE have lost a characteristic energy. To predict the energy distribution of scattered electrons, Monte-Carlo simulations are typically used, including elastic as well as inelastic scattering cross sections with momentum dependent energy loss functions (Kuhr and Fitting [1999]). For low energy electrons, the energy loss will depend to a great extend on the actual energy of the electrons since the maximal loss is limited to the incident electron energy and the loss function should be cut-off in a certain manner (Fitting [2004]).
The mean energy of scattered electrons derived by these Monte-Carlo simulations is shown in figure 4.8. This shows, that the mean energy loss of electrons decreases with smaller primary beam energy, not only because no sufficient energy is available for higher energy excitations, but also because the lower energy excitations, such as excitations of surface plasmons, becomes more likely for lower energy electrons (Kuhr and Fitting [1999]).

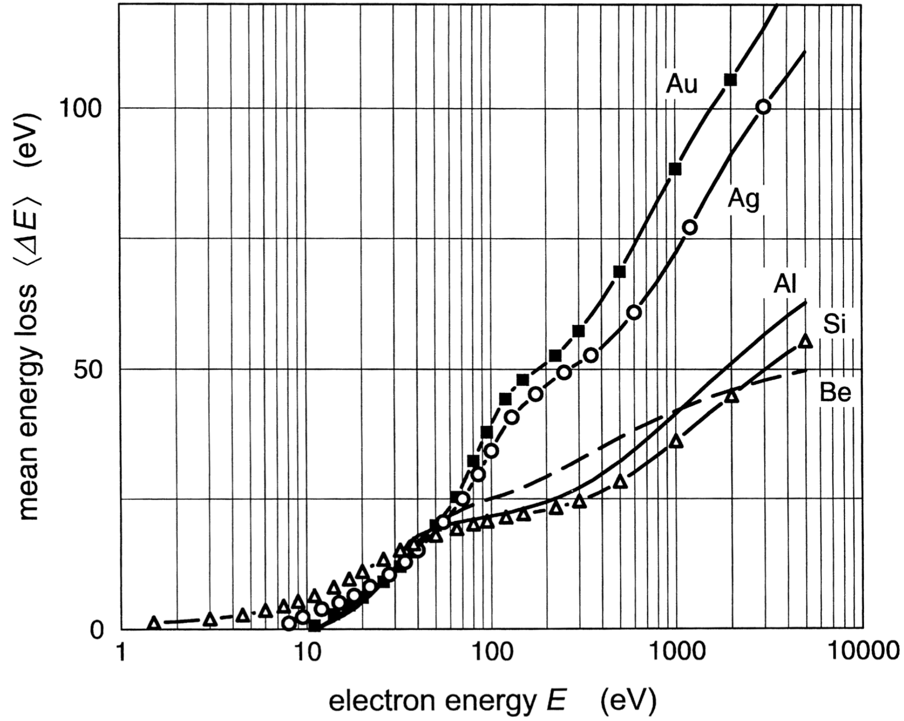


Figure 4.8: Mean energy loss of electrons with kinetic energy E in different elements (Fitting et al. [2001]).

### 4.2.4 Contrast Mechanisms

The obvious contrast mechanism using backscattered electrons in SEM imaging is the realization of different backscattering coefficient for different materials. For high energies and thin samples, i.e. $D \ll R/2$, equation 4.4 shows $\eta \propto N_A Z^2$, so variations of the atomic number and density within the sample lead to image contrast. Secondly, the backscattering coefficient is proportional to the sample thickness and therefore differences of the sample thickness directly lead to signal contrast in the image, too. For thin samples on a substrate, BSEs of both, sample and substrate contribute to the signal. For different backscattering coefficient $\eta_{\infty,s}$ of the substrate and $\eta_{\infty,a}$ of the sample, the total backscattering coefficient varies from $\eta_{\infty,s}$ to $\eta_{\infty,a}$ with increasing sample thickness $D$ and therefore variations in $D$ contribute also to the image contrast.
For $D \gg R/2$ and energies above 10 keV, $\eta$ still increases monotonically with the atomic number in form of $\eta \propto 2^{-Z}$ for normal beam incidence (equation 4.6), leading to Z-contrast in the SEM-image. For lower energies, however, the Z-contrast becomes less distinct, as figure 4.3 shows. At 1 keV the backscattering coefficient is nearly constant in terms of the atomic number for $Z > 20$. Jaksch [2011] and Jaksch [2012] show that bonding structure of outer shell electrons and plasmon losses are essential contrast mechanisms for low electron energies (under 2 keV) rather than atomic number or density.

## 4.3 Beam Damage, Charging, and Contamination

An electron beam can damage the sample in different ways, depending on the beam energy. In comparison to transmission electron microscopy, energies used in the SEM are too low to induce atomic displacement damage except for lightest atoms (Egerton et al. [2004]). The knock-on threshold for carbon lies between 40 keV and 60 keV, depending on the local bonding (Muller [2009]). But while the displacement damage for heavier atoms goes down with decreasing energy – figure 4.7 (a) shows that for decreasing incident energy – the energy transfer to the sample rises. Simultaneously the interaction volume decreases, so the beam damage per unit volume in the sample is greater for low energies[2] (Joy and Joy [1996]). Damage in biological samples occurs through electron excitations leading to bond breaking, which requires only an energy of a few electron volt. The change in electronic configuration leads to loss of fine structure in the electron loss spectrum and the bond breaking can thus lead to the escape of light atoms, particularly hydrogen, nitrogen and oxygen (Egerton et al. [2004]).
To reduce beam damage, the dose has to be reduced, which of course reduces the signal and therefore resolution. To overcome this conflict, high performance instrumentation is required to reach good resolution even at low electron dose.
Few experiments have been performed with beam energies far below 1 keV and the actual beam damage of biological samples at such energies has still to be investigated. Spence et al. [1994] have shown in TEM mode little damage on purple membrane at 100 eV with a dose of $10\,000\,e\,\text{Å}^{-1}$. Dapor et al. [2018] have performed spectral SE imaging of semi-crystalline polymers in a scanning electron microscope at 200 eV, intending to avoid significant ionization damage since the energy is below the ionization energy of the K-shell for carbon. However, they do not discuss any other possible damage of their sample. Referring to Joy and Joy [1996], damage should be completely eliminated at beam energies of 25 eV and lower, because then there are no more high cross-section inelastic events with sufficient energies to break bonds in the sample.
This is in agreement with HREELS experiments at 10 eV to 30 eV primary energy, where no sign of degradation is observed in the signal during the measurements on molecular monolayers of organic compounds (personal communication with Prof. Petra Tegeder, PCI, Heideberg University). In our work, we are trying to accomplish spectroscopy in the same energy range with little to no beam damage, however, with high spatial resolution inside a SEM.

If the specimen in the SEM ist not or poorly conducting, charging of the specimen can become a problem for imaging, since the electric field of the sample can interfere with the collection of secondary electrons, deflect the incident beam or even damage the sample. For a conductor, the current in the specimen can be written as

[2] The results will show, that we could not confirm this statement for our measurements on organic and biological samples with energies between 1 keV and 100 eV

$$I_B = \delta I_B + \eta I_B + I_{SC}, \tag{4.10}$$

where $I_B$ is the beam current, $\delta$ the SE yield, $\eta$ the backscattering coefficient and $I_{SC}$ the specimen current to the ground (Egerton et al. [2004]). For a non-conductor, $I_{SC}$ is zero and hence a charge is building up in the specimen at rate

$$\Delta Q/\text{second} = I_B(1 - (\delta + \eta)). \tag{4.11}$$

The charging of a sample depending on the incident beam energy is shown in figure 4.9. At lowest beam energies, the incident electrons have not enough energy to sufficiently produce secondary electrons. The total yield $(\delta + \eta)$ is lower than unity and the specimen is charged negatively. With increasing energy, between a few hundred and a few thousand electronvolt, the secondary yield becomes larger than unity and $(\delta + \eta)$ therefore, too. More charge is leaving the specimen than injected by the beam and the specimen is charged positively. For high beam energies, the penetration depth of the beam is so large, that most of the secondary electrons can't escape from the sample. $(\delta + \eta)$ becomes less than unity again and the specimen is charged negatively.

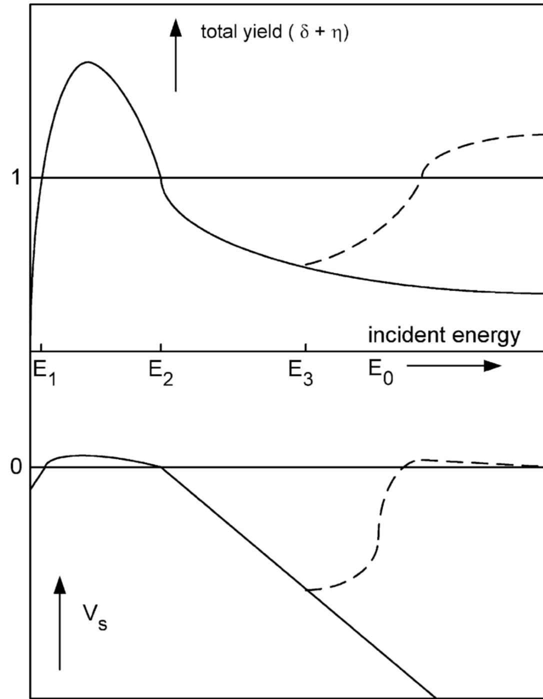


Figure 4.9: Total electron yield $(\delta + \eta)$ and surface potential $V_S$ in a poorly conducting bulk specimen or thin film (dashed curve), as a function of incident-beam energy $E_0$. Egerton et al. [2004]

There are two points, where $(\delta + \eta) = 1$, and therefore even for an insulator no charging is observed. The lower value, $E_1$ is typically between 50 eV and 150 eV and $E_2$ between 0.5 keV and 3 keV (Joy and Joy [1996]). For thin samples there is a third point, where the charging becomes positive again. It is when the range of the electrons becomes higher than the sample thickness and no charge is injected into the sample from the incident beam. Some values for $E_2$ are shown in table 4.1.

| Sample | $E_2$ in keV |
|---|---|
| PMMA | 1.2 |
| $SiO_2$ | 1.7 |
| $Al_2O_3$ | 2.1 |
| Natural diamond | 1.2 |
| Silica glass | 1.7 |

Table 4.1: $E_2$ values for different materials (Rau et al. [2008]).

Cazaux [2005] has introduced a new model of secondary electron emission yield, for application to polymers, where the results imply a zero charging point for most polymers in the range of 0.6 keV to 1.5 keV.

The last point I want to mention here is hydrocarbon contamination, since low voltage SEM is especially sensitive to it. It occurs when hydrocarbon molecules are polymerized by the electron beam and deposit on the sample. The molecules originate from pump oils, vacuum grease, etc. in the sample chamber and lead to contamination of the sample. Also the sample itself can be a source of hydrocarbons leading to contamination. Since low voltage microscopy is very sensitive to the surface, even a few atomic layers can strongly disturb the imaging.

# 5 Scanning Electron Microscopy

In this chapter I will briefly introduce the working principle of a SEM and give an overview on recent SEM developments especially in the direction of low-voltage SEM (LVSEM). Afterwords I will introduce the special design of the DELTA SEM, which not only allows to achieve high resolution at lowest electron energies, but also allows to perform spectroscopy on backscattered electrons.

## 5.1 Overview on the Current State of SEM Applications

In a scanning electron microscope, an electron beam is focused to a point on the sample. In the optimal case, the focus point has a Gaussian distribution with a FWHM (full width half maximum) of about 1 nm or even smaller. Figure 5.1 shows the typical setup of a SEM. By scanning the sample point by point with the focused electron beam (probe), a two dimensional image is generated. The lateral resolution of a SEM is therefore mainly dependent on the probe size, i.e. it is the better, the smaller the focus point of the electrons is. The second key factor limiting the resolution is the brightness of the electron source - when the electron flux becomes too small in the probe, poor signal to noise ratio (SNR) limits the resolution (Bogner et al. [2007]). The third limiting factor ist the interaction volume of the beam in the specimen, which is discussed in chapter 4.
The improvement in resolution as well as the use of lower beam energies was in the first place driven by the development and implementation of brighter electron sources like cold and thermal field emitters (El-Gomati and Walker [2014]). In a field emission gun (FEG), a tungsten wire with a sharp point and a layer of zirconium oxide, supported by a hairpin, emits electrons by quantum mechanical tunneling process when it is brought into close proximity with a positively biased extraction electrode (Bogner et al. [2007]). The FEG has a high brightness of the order of $10^8\,\mathrm{A\,cm^{-2}\,sr^{-1}}$ to $10^9\,\mathrm{A\,cm^{-2}\,sr^{-1}}$ at 20 keV, a small virtual source size (diameter of the electron beam generated by the source) in the range from 5 nm to 25 nm and a low chromatic energy spread $\Delta E$ varying from 0.15 eV to 0.5 eV for different types of FEGs. The last point is especially important for low beam energies where chromatic aberration of the probe forming electron optics becomes a major factor (Joy [1991]).
After leaving the gun, the electron beam will diverge. The condenser lenses converge and collimate the electrons leading to a relatively parallel, demagnified beam. The spray aperture excludes non-homogeneous and scattered electrons. The objective

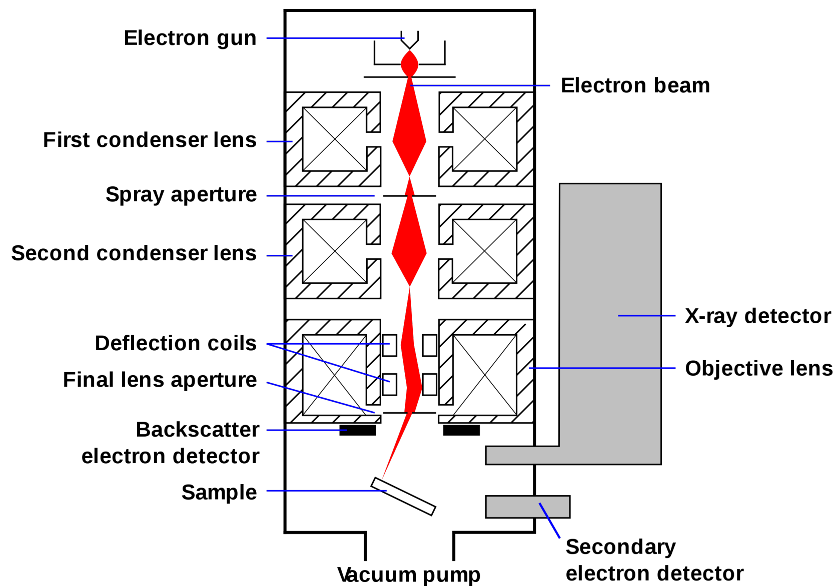


Figure 5.1: Schematic setup of a conventional SEM. (Wikipedia contributors [2019])

lens (also called probe forming lens) focuses the beam on the sample. The deflection coils allow to scan the probe over the sample to generate an image. The final lens aperture affects the beam shape and edge sharpness, also minimizing detrimental effects of aberration on the probe size (Zhou et al. [2006]).
The resolution of standard SEM machines is in the order of few nanometers. Modern electron microscopes contain complex electro-optical devices and lens systems, to correct for aberrations without reducing the electron flux, enabling resolutions better than the nm range. This way even atomic resolution can be achieved in an SEM setup using secondary electrons, however with very high electron energy at 200 keV (Zhu et al. [2009]). At low beam energies, resolutions below 1 nm can be achieved with corrected SEM systems (Kazumori et al. [2004]). Michael [2011] has shown 1.1 nm resolution with a monochromated SEM with no dedicated aberration correction at 500 eV beam energy, which shows that chromatic aberration is a main limiting factor for the resolution of a low voltage SEM.

Operating a SEM at low beam energies has many advantages. For organic and biological samples the reduced beam damage by using low-energy electrons is important to preserve the structural integrity of the imaged specimen (Pawley [2008]). Moreover, LVSEM can positively influence the imaging quality as the interaction volume decreases which improves the resolution (signal localization) by confining the generated signal to a smaller area. Low-Z (e.g. organic) materials have an increasing backscattering coefficient at decreasing energy, which improves the contrast for those materials. Charging of insulating materials can be reduced by decreasing the electron energy, which can reduce charging artifacts for those materials. These points are discussed in more detail in chapter 4.

As already mentioned, chromatic aberrations need to be considered in order to maintain high resolution with low electron energies. The influence of chromatic aberration contribution on the probe diameter is given by

$$d_{Chr} = C_C \alpha \frac{\Delta E}{E}, \tag{5.1}$$

where $C_C$ is the chromatic aberration coefficient, $\alpha$ the convergence angle for any ray traveling through the lens, $\Delta E$ the energy spread of the source and $E$ the beam energy (Michael [2011]). So the effect of chromatic aberration becomes larger with lower beam energy, since the relative error of the energy spread increases.
One approach to reduce the electron energy even down to 1 eV without aberration correction was introduced by Müllerová and Frank [1993] implementing a cathode lens to the specimen chamber in a routine SEM. Although the results show interesting contrast mechanisms for material science when imaging at ULV (Frank et al. [2007]), the resolution seems to be limited to at least tens of nanometers.
Another possibility to correct for spherical and chromatic aberrations is an electron mirror. Dohi and Kruit [2018] gives a good overview on the implementation of mirror correctors to LVSEMs and introduces a modified approach using miniature mirrors to reduce aberrations of a bending magnet. The problem of a bending magnet, which bends the beam path at a large angle in order to mirror it, is that it generates its own large energy dispersions. To counterpart this effect, the beam separator has to be specially designed on the theory of curved-axis optics (Müller et al. [1999]). Such a system was designed and built for the SMART project (Fink et al. [1997]). A beam separator designed on the basis of the same concept is implemented in the prototype instrument used in this work – the so called DELTA SEM.

## 5.2 DELTA SEM

The work in this study is performed with a prototype microscope developed by ZEISS named "Delta" based on the shape of the central beam splitter (Schroeder et al. [2018]). Figure 7.1 shows the microscope located at the Institute of Molecular System Engineering and Advanced Materials in the University of Heidelberg and a schematic of the beam path through the microscope. The design with curved-axis optics in the central beam splitter and mirror corrector, which results in the namegiving delta-shaped beam path, allows – as mentioned in the previous section – to correct spherical and chromatic aberrations and enables a resolution around 1 nm at lowest energies down to 10 eV.
Moreover, this geometrical design allows to collect the BSE and SE signal separately from the primary beam by guiding it again through the beam splitter. Only this way it becomes possible to implement a spectrometric detector system outside the beam column, whereas there is no possibility to implement a spectrometer for backscattered electrons in a standard, top-down SEM design as illustrated in figure

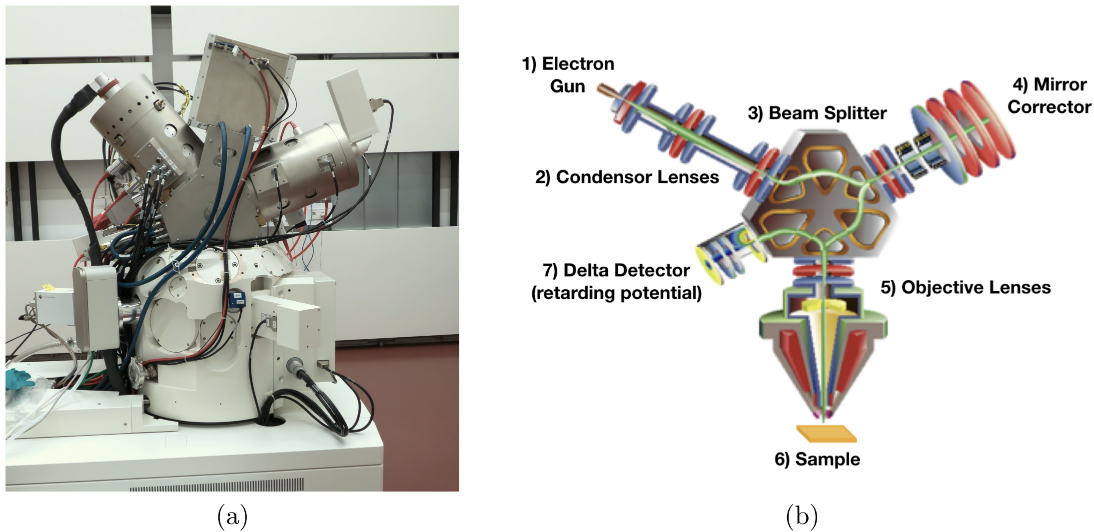


(a) (b)

Figure 5.2: (a) Picture of the DELTA Microscope, (b) schematic of the beam path through the components. Source: Carl Zeiss Microscopy (Oberkochen, Germany) (description edited).

5.1.

Figure 7.1 (b) shows a schematic overview of the microscope setup. From the electron source (thermal FEG with DENKA tip) the electron beam goes through the condenser lenses into the beam splitter located in the center of the device. There the beam is guided through magnetic fields into the mirror corrector, reflected back into the beam splitter and then focused and decelerated to the required landing energy by the objective lenses onto the sample. The electrons reflected and generated by the sample are then either detected by the In-Lens detector in front of the objective lenses, or guided back through the beam splitter to the DELTA Detector (DD). The signal distribution was studied in this work and is discussed in chapter 7.
The DD consists of a scintillator and a photomultiplier tube for the detection of the electrons. In front of the scintillator is a wire grid which can be set on an electric potential, thus only electrons with an energy above a certain energy threshold can pass the retarding potential and will then be detected. The working principle is shown in Figure 5.3. An aperture can be placed in front of the DD and the aperture size can be varied in order to improve the energy resolution. Of course, with smaller DD-aperture the intensity of the measured signal goes down.
The specimen is brought onto the navigation stage in the sample chamber through an air lock chamber with its own vacuum pump, so the sample chamber does not need to be opened. The sample chamber vacuum is in the order of $10^{-7}$ bar. To further reduce contamination, a plasma cleaner is integrated in the sample chamber. Three ion getter pumps reduce the beam-path vacuum in the column from $10^{-7}$ bar at the opening to the sample chamber to about $10^{-9}$ bar at the FEG.

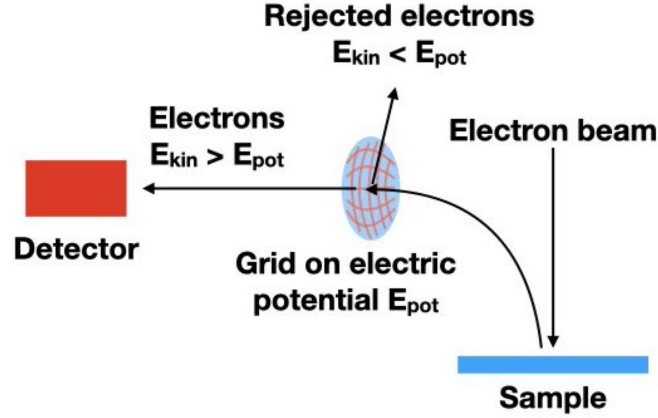


Figure 5.3: Schematic of the working principle of the Delta Detector. Only electrons with a kinetic energy above the grid potential can be detected.

The design of the DELTA SEM allows to record spectral image series with primary energies down to 10 eV and at high spatial resolution.

## 5.3 Data Acquisition

The scintillator-photomultiplier system of the DD creates an electric signal whose intensity is proportional to the number of detected electrons for every scanning point. The signal is then converted into a two-dimensional gray-value image, where the gray value represents the measured intensity.
An electron energy spectrum can simply be measured with the DD by varying the detector-grid voltage (DD-Grid) in the range of interest and taking a SEM image for every DD-Grid voltage step, as shown in Figure 5.4. This gives a cumulative intensity (gray value) spectrum for each image pixel proportional to the number of electrons able to pass the DD-Grid. Since the navigation stage will drift slightly with time (after it was moved), the image shifts for each point in the spectrum. To study the spectrum of structures in the image, the stage drift has to be corrected so that the corresponding structures are aligned in all images. Especially for large magnifications the stage drift may be so large, that the structure of interest completely drifts out of the field of view during the measurement, then – of course – no alignment is possible anyway.
By differentiating the cumulative spectrum, i.e. subtracting the intensity values of neighboring voltage steps from each other, a typical energy dependent spectrum is obtained, which is proportional to the number of electrons with an energy between the potential energy of the two subtracted DD-Grid voltages:

$$\text{for } m = 1...M, \quad N_e(E_{V_m} < E < E_{V_{m+1}}) \propto I(V_{m+1}) - I(V_m), \tag{5.2}$$

where $m$ is the voltage step, $N_e(E)$ is the number of electrons with energy $E$, $I(V_m)$ is the measured intensity for the DD-Grid voltage at step $m$ and $E_{V_m}$ is the potential

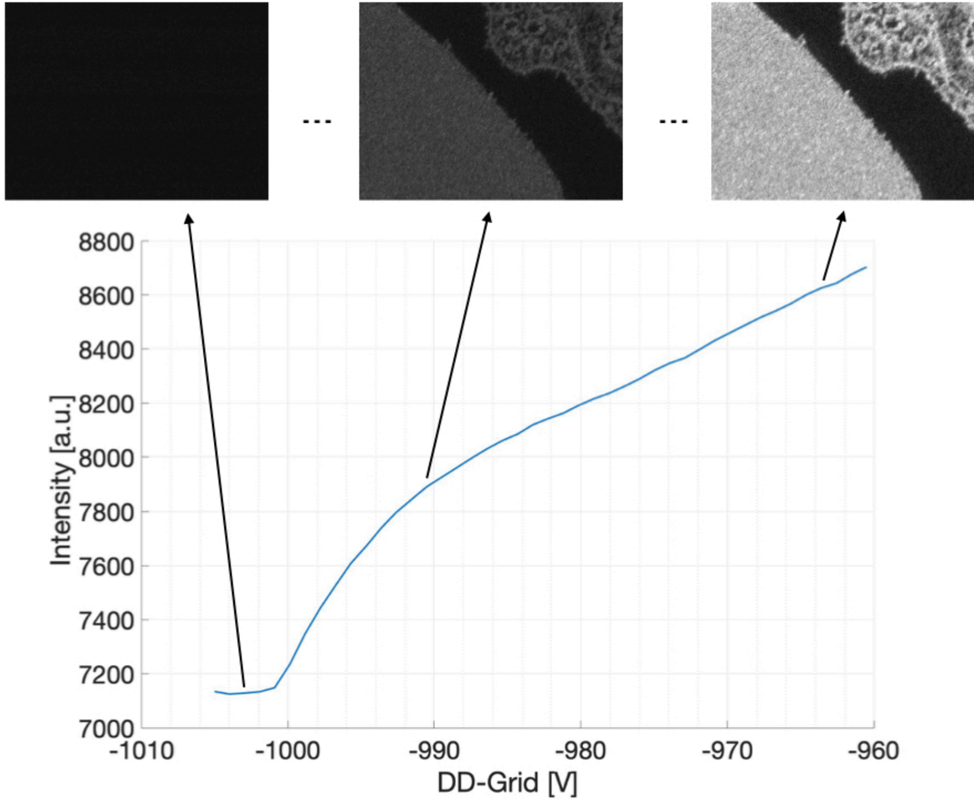


Figure 5.4: Example graph for spectral data acquisition (image of a serial section slice of mouse muscle) with the DD at 1 keV primary energy. For DD-Grid voltage below −1000 eV (threshold higher than the primary energy) no electrons can pass the grid, therefore only noise is measured. The Graph shows the intensity (gray value [a.u.]) averaged over all image pixels for each DD-Grid voltage step with a step size of 1 V.

energy of the DD-Grid at step $n$. For the plot of the differentiated spectrum, the mean value of the voltage steps $V_{diff} = (V_m + V_{m+1})/2$ is taken as the corresponding voltage value for the intensity difference. Figure 5.5 (b) shows the differentiated example plot.
The spectrum of a single pixel has usually a very noisy SNR, as shown in figure 5.6. SNR can be improved by averaging over more scans per energy step (SpS), or by decreasing the scan speed and thus increasing the probe's dwell time on a pixel. Both approaches increase the number of detected electrons and improve the stochastic noise. However, they may have different effects on charging and contamination depending on the conductivity and composition of the specimen. The more serious problem of increasing the SpS or dwell time is that it increases the dose and the measurement time for a spectrum, which potentially leads to larger beam damage and larger stage drift, respectively.

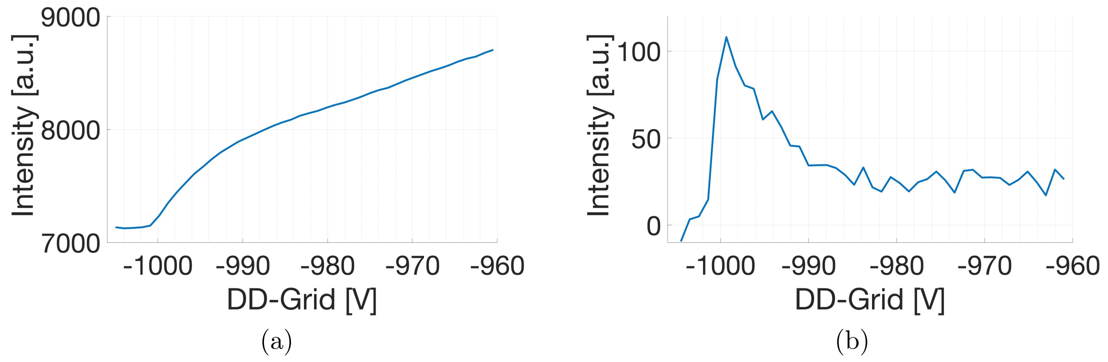


Figure 5.5: (a) Cumulative example BSE spectrum and (b) differentiated spectrum averaged over the whole image of a serial section slice of mouse muscle.

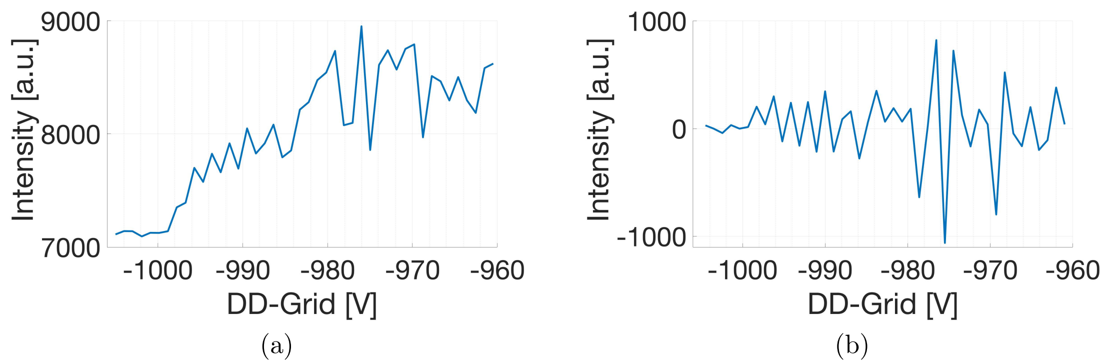


Figure 5.6: (a) Cumulative and (b) differentiated single pixel spectrum of the example graph in figure 5.5. Intensity of each spectral point is averaged over five image scans (5 SpS), dwell time 3.2 µs per pixel. Note the extreme noise of such experimental data.

To generally identify spectral characteristics in the BSE signal of different materials as a first step, stochastic noise can be simply reduced by averaging over a large number of pixels in a region of interest.

# 6 Samples and Evaluation Methods

## 6.1 Samples and Sample Preparations

### 6.1.1 Polycrystalline Gold

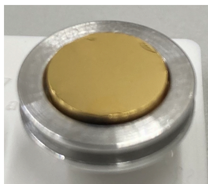

The gold sample was provided by the group of Prof. Petra Tegeder (PCI, Heidelberg University). They use this kind of gold block as substrate for their HREELS measurements (Maass et al. [2019]). After annealing under UHV conditions inside the experimental HREELS setup, the surface becomes mono-crystalline Au(111). Since we had to transport the sample through ambient conditions into our high vacuum microscope chamber, we had to clean the surface by using the built in plasma cleaner (GVV10x EC15 'downstream asher' by ibss Group, Inc.) inside the sample chamber. The block was put into a specially designed SEM stub. The surface contamination was removed after 4 h plasma cleaning with 50 W in our instrumentation. Unfortunately, the surface turned out to be polycrystalline after this procedure.

### 6.1.2 Flat DNA Origami Platelets

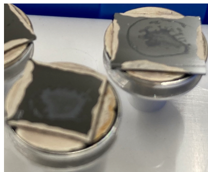

DNA origami platelets (Hernandez-Ainsa et al. [2013]) were provided by Mai Tran (AG Prof. Kerstin Göpfrich, ZMBH, Heidelberg University) in a buffer containing 5 mmol Tris (Tris(hydroxymethyl)aminomethan), 5 mmol EDTA (Ethylenediaminetetraacetic acid), 12.5 mmol $MgCl_2$ and 5 mmol $KCl$. Each platelet has 12 binding sites for the Cy3 fluorophores. The concentration of DNA origami inside the buffer for both batches is given in table 6.1.

The solution was carefully drop-casted on a cleaned silicon wafer (p-doped, Boron 100$ppm$). The wafer was exposed to air plasma in a Zepto Plasmacleaner (Diener electronic GmbH und Co. KG) for about 30 seconds to make the surface hydrophilic so that the solution spreads well on the wafer. For a good concentration and distribution of the origami on the wafer, a 1 µl droplet of the buffer was placed on the wafer first, afterwords a second 1 µl droplet of the solution containing the origami was placed onto the first, spread droplet. This gave a more decent distribution than diluting the origami before drop-casting. Dr. Irene Wacker has provided significant help with her expertise to improve the preparation.

To reduce the amount of residual contaminants from the solution, the wafer was care-

Table 6.1: Concentrations of the origami solutions.

| | Concentration origami (no fluorophore) | Concentration origami + Cy3 |
|---|---|---|
| First Batch | 297.0 ng µl$^{-1}$ | 276.4 ng µl$^{-1}$ |
| Second Batch | 182.4 ng µl$^{-1}$ | 155.8 ng µl$^{-1}$ |

fully cleaned with pure water 60 seconds after the drop-cast (so that the origami can settle and adhere onto the wafer). Afterwords, the wafer were put on SEM stubs and fixed with conducting silver paste (Acheson Silver DAG 1415).

### 6.1.3 Exfoliated Graphene

Daniel Ehjeij (AG Prof. Uwe Bunz, OCI, Heidelberg University) provided the graphene flakes produced via electrochemical exfoliation. They were suspended in N,N-dimethylformamide (DMF), which has been found to yield stable graphene suspensions (Johnson et al. [2015]). The electrochemically exfoliated graphene suspension was further diluted with DMF in order to achieve a good distribution of flakes on the substrate. The solution containing the graphene flakes was drop-casted onto a cleaned silicon wafer (p-doped, Boron 100$ppm$), which were placed on a hot plate at 60 °C to 70 °C to evaporate the solvent.
To reduce the contamination by the residuals of the solvent, the samples were treated with argon plasma in the Gatan Solarus Model 950 Advanced Plasma System, using Ar gas of 99.998 % purity. The wafers were treated for 15 seconds, with radio frequency (RF) power of 5 W and gas flow of 33.3 sccm, at a pressure of 9.33 Pa (Wrege [2022]).
The exfoliated graphene flakes were drop-casted on 'UltraAuFoil' gold TEM grids (S343-8-UAUF by Plano GmbH) without further plasma treatment.

### 6.1.4 Printed Structure Containing Quantum Dots

The 3d-printed structure was developed by Frederick Mayer (AG Prof. Martin Wegener, IAP, Karlsruhe Institute of Technology). The printing process and used materials are described in detail in Mayer et al. [2019]. The main monomer used as basis of the photoresist is PETA (Pentaerythrittetraacrylat), to which in the formulation process 10 % (w/w) nonpolar (oleic acid) functionalized CdSeS/ZnS alloyed quantum dots ($\lambda_{em}$ = 450 nm for the blue-emitting quantum dots) in toluene solution (1 mg ml$^{-1}$) was added.
The printed structures were stained pre embedding: Pre-weighed $OsO_4$ crystals were dissolved in dry acetone to 1 % (wt/vol) and transferred to a weighing glass with tight lid. Porous polymer pillars were submerged in the liquid and incubated for 2 h. For the embedding Epon (42.4 g glycid ether 100, 29.6 g dodecenylsuccinic acid anhydride, 18.4 g methyl-5-norbornene-2,3-dicarboxylic anhydride and 2.4 g benzyldimethylamine as initiator) was used, the embedded sample was cured 24 h at

60 °C. 70 nm thick sections were cut with an ultramicrotome which were placed on a silicon wafer. The embedding end sectioning was performed by Ronald Curticean.

### 6.1.5 Graphitized Cellulose Paper

The carbon structure was obtained from pyrolyzing an origami-folded cellulose paper and featuring a randomly distributed carbon microfiber network (detailed fabrication can be found in Islam et al. [2018]). Spurr's low viscosity resin, firm (mix 4.10 g ERL 4221 (3,4-epoxycyclohexanemethyl 3,4-epoxycyclohexanecarboxylate), 1.43 g DER 736 (diglycidyl ether of polypropylene glycol), 5.90 g NSA (nonenyl succinic anhydride), then add 0.1 g DMAE (Dimethylaminoethanol) and mix thoroughly) was used for direct embedding of small pieces of pyrolized paper origami. The embedded structure was cut using an ultamicrotome into 200 nm sections placed on a silicon wafer. More details on the preparation process can be found in Wacker et al. [2023]. Embedding and sectioning was performed by Li-Yu Huang (AG Prof Ulrich Gengenbach, AIA, Karlsruhe Institute of Technology).

### 6.1.6 Tetra-Phenyl Cumulenes

The samples of Tetra-Phenyl Cumulenes (Wendinger and Tykwinski [2017]) were provided by Prof. Rik R. Tykwinski (Department of Chemistry, University of Alberta) in dry chemical state. Both $C_{30}H_{20}$ (PH5) and $C_{28}H_{20}$ (PH3) were dissolved in Tedrahydrofran (THF, CAS: 109- 99-9) in concentrations of 5 mg ml$^{-1}$. 5 µl of the solution were drop-casted on a cleaned silicon wafer (p-doped, Boron 100$ppm$), which was used for the SEM experiments (King [2024]).

### 6.1.7 Polymere Microspheres

The sample preparation of the microspheres for SEM and TEM were performed by Jochen Kammerer. The synthesis was performed by Florian Feist (AG Prof. Christopher Barner-Kowollik, Centre for Material Science, Queensland University of Technology) (Kammerer et al. [2023]). The embedding process is described in the supporting information of Kammerer et al. [2023]: 'The microspheres were mixed with EPON (42.4 g glycid ether 100, 29.6 g dodecenylsuccinic acid anhydride, 18.4 g methyl-5-norbornene-2,3-dicarboxylic anhydride and 2.4 g benzyldimethylamine as initiator) in 0.2 ml microcentrifuge tubes. The dispersion was sonicated for 1 h in a water bath and subsequently centrifuged (5-10 min in a Sigma 3-16KL centrifuge at max speed of 15300rpm / 21 900 g). The samples where then cured in an oven for 24 h at 60 °C.'
Ultramicrotomy was employed on the embedded microspheres to cut ultra-thin (60 nm to 80 nm) sections which were placed on a silicon wafer for the SEM study.

### 6.1.8 Printed PETA Structures with Fluorophores

The structures for the electron radiation studies were prepared by Enrico Lemma (AG Prof. Martin Bastmeyer, Zoological Institute, Karlsruhe Institute of Technology) using a protocol for DNA hybridization of printed scaffolds (Lemma et al. [2023]): A photo-reactive molecule (photoenol) was mixed (10 % w/w) to the photoresist PETA (pentaerythritol triacrylate) commonly used for two-photon lithography. The photoresist was printed on ITO glass (Optics Balzers, P/N 204776) and then selectively functionalized with single stranded DNA, to which the target DNA with attached Cy3 fluorophore was bound. The detailed preparation process is described in Lemma et al. [2023].

## 6.2 Data Evaluation and Scripts

### 6.2.1 Fluorescence Survival Rate Evaluation

The evaluation of the fluorescence survival rate of Cy3 molecules after electron irradiation was performed on FM images taken with an upright light microscope (AxioImager 2, Carl Zeiss Microscopy, Oberkochen, Germany) with long distance objectives. The RFP-channel was used for excitation (photodiode mean wavelength = 555 nm). The recorded RGB-image was converted to 8-bit gray-scale for further evaluation.
The intensity (gray-value) was averaged for three regions: Not irradiated structure with fluorophores (A), irradiated structure with fluorophores (B) and not irradiated ITO glass support as background reference signal (C). The fluorescence survival rate was calculated with

$$\text{Survival Rate} = 1 + \frac{I_B - I_A}{I_A - I_C}. \tag{6.1}$$

Figure 6.1 shows an irradiated sample with indicated regions over which the signal intensity was averaged for the evaluation. The error of the survival rate was calculated by the error propagation from the standard deviation of the averaged gray values:

$$\sigma_{\text{Survival Rate}} = \sqrt{\left(\frac{1}{I_A - I_C}\sigma_B\right)^2 + \left(\frac{I_C - I_B}{(I_A - I_C)^2}\sigma_A\right)^2 + \left(\frac{I_B - I_A}{(I_A - I_C)^2}\sigma_C\right)^2}. \tag{6.2}$$

For each primary energy and for each irradiation dose 2 to 4 structures were irradiated and averaged in the evaluation. The resulting error of the averaged survival rates is then calculated with

$$\sigma_{\text{Survival Rate, avg}} = \sqrt{\sum_{i=1}^{N} \left(\frac{\sigma_{\text{Survival Rate},i}}{N}\right)^2}, \tag{6.3}$$

with $N$ being the number of averaged evaluated areas.

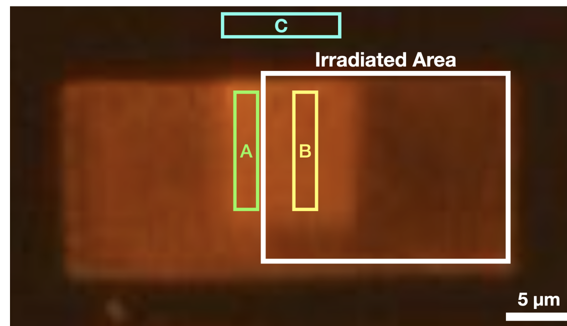


Figure 6.1: FM image of the functionalized PETA stucture with fluorescent markers after electron irradiation. Regions for the evaluation of the survival rate are exemplarily indicated (see text).

### 6.2.2 Protocol to Obtain bsEELS Spectra out of Image Raw Data

The microscope software developed by Zeiss exports the recorded spectral images as an image stack in a MatLab file. The images are exported as '.tif'-files for further processing using the MatLab script 'hd_exportSpectralImageStackToTiff.m' written by Jörg Eisele (C.1).
The image stacks are aligned in order to correct for the stage drift using the FIJI plugin 'Linear Stack Alignment with SIFT' based on Lowe [2004]. The aligned image stack is converted back into a MatLab file for the next step using the MatLab script 'hd_replaceSpectralImagesByImageStack.m' (C.2).
On the basis of the aligned images, black and white (8-bit grayscale value 0 and 255) masks of the 'regions of interest' (ROI) are created manually with FIJI and saved to a separate folder. An example of masks for an spectral image stack is shown in figure 6.2.
These masks are used to define the regions from which the spectra are extracted from the spectral image stacks. This is done with the MatLab script 'hd_exportAveragedSpectrumOfMappedRegionsFromFolder.m' (C.3). The script takes the spectral images and averages the gray values of the pixels in the selected regions according to the created masks. The output are two .csv files per mask each with two columns. One file contains the voltage values of the DD-grid and the averaged gray value – in other words the cumulative spectra from the selected image regions in each mask. One file contains the differentiated gray values with the corresponding DD-grid values as described in section 5.3 – in other words the energy-loss spectra.
These .csv-files are used for plotting of the spectra with the MatLab plot function.

Figure 6.2: Example of manually created masks for further spectrum evaluation from DNA-origami and silicon wafer. Note that the distribution and size of the selected silicon wafer regions is on purpose distributed over the whole image to approximately match the size and distribution of the origamis in order to exclude systematic differences from spectral artifacts ('anisochromaticity', see chapter 7).

### 6.2.3 Convolution Fit Procedure

For the convolution fits shown in the part IV ('Results'), the reference spectra are modeled with a sum of simple Gauss function in the form of

$$y = a \exp - \frac{(x-\mu)^2}{2\sigma^2} + b. \tag{6.4}$$

Thereby the peak position or mean value $\mu$ and the width or standard deviation $\sigma$ are extracted from reference measurements and are kept as fixed parameters. The amplitude $a$ and offset $b$ of each excitation are the free parameters fitted to the bsEELS spectra. Only for the $SiO_2$ an empirical step-function was used to model the onset of the band gap excitation (see appendix section C.4).
If the width of the measured ESF had to be reduced (see section 12.1), this was done by interpolating the ESF over 100 datapoints per 1 eV energy step and removing every $n$'th data point.
The model was then convoluted with the ESF using the 'conv'-function in MatLab. The resulting convolution was plotted together with the measured bsEEL spectra and the free parameter were varied by hand to achieve the best fit. The Script for the convolution with MatLab can be found in the appendix in section C.4.

# Part III

# Approaching Spectral Imaging with Ultra-Low Voltage SEM

Spectral imaging with a SEM at primary beam energies down to 10 eV is a completely new approach, challenging and expanding conventions and experimental possibilities in the field of electron microscopy. In this part I want to lay out which potential developments and new applications are connected with this novel experimental approach, how it complements established methods in the field of microscopy and spectroscopy, but also which limiting factors our prototype setup has at this stage needed to be addressed in the further development of this method.

# 7 Signal Collection of the Microscope Detectors

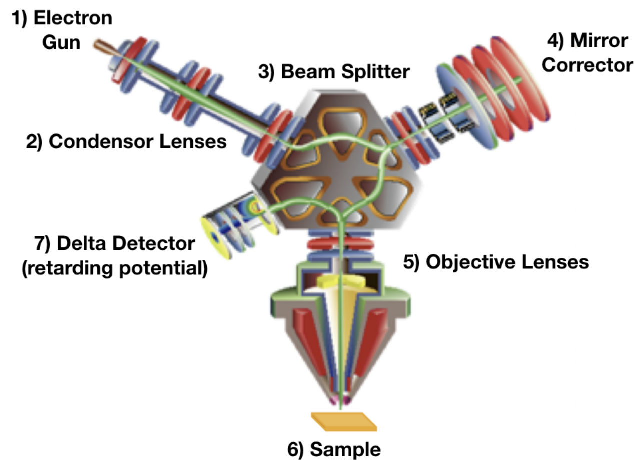


Figure 7.1: Schematic of the beam path through the components. Source: Carl Zeiss Microscopy (Oberkochen, Germany) (description edited).

Figure 7.1 shows the schematic of the beam path through the microscope. The Microscope is currently operating with two detectors: An inlens detector sitting in the beam column behind the pole piece and the so called 'Delta Detector' equipped with a retarding potential spectrometer, which is located at the side of the beam splitter. Both are single pixel scintillator detectors.
The pole piece is designed to decelerate the electrons to the desired landing energy onto the sample and to collect the electrons scattered and emitted from the sample back towards the detectors. Figure 7.2 illustrates the electron trajectories towards the detectors. The potential between pole piece and sample surface accelerates all scattered and emitted electrons back along the incoming beam path. Electrons scattered at large angles with respect to the primary beam and with high energy are collected with a large distance from the primary beam path and hit the inlens detector. Electrons scattered with small angles with respect to the primary beam (180° scattering) are close to the primary beam path and do not hit the ring-like inlens detector, but are guided back through the beam splitter to hit the DD.
At ultra-low primary energy also the electrons scattered at high angles with respect to the primary beam (90° scattering) have such a low momentum that they do not gain enough transverse separation to hit the inlens detector. This can be very nicely

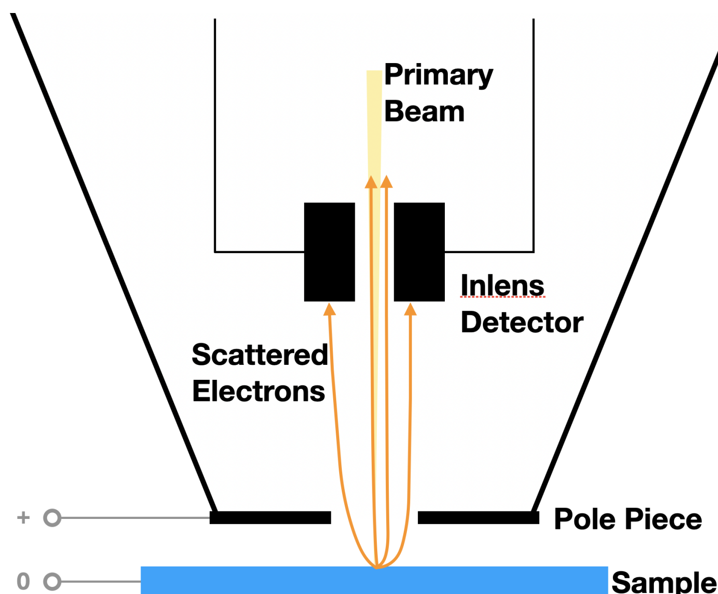


Figure 7.2: Schematic of the trajectories of scattered electrons towards the inlens detector and 'Delta Detector'.

observed at lowest magnification, which means largest primary beam deflections for the image scan. Figure 7.3 shows inlens images at 1000 eV and 80 eV at lowest magnification. The outer parts of the images are bright. Due to the large deflection angle of the primary beam, the electrons are widely separated from the beam column path and therefore most scattered and emitted electrons are collected on a outer trajectory hitting the inlens detector. At the dark inner circle, the deflection angle is smaller, so more electrons are on inner trajectories and do not hit the inlens detector, but are guided to the DD. The interesting part is now the difference between 1000 eV and 80 eV.

For 1000 eV the inner image part is darker, but still electrons do reach the inlens detector and signal ca be measured. There is no clear edge but a smooth gradient towards the image center. In contrast, for 80 eV the inner signal is dark, except of noise no signal is detected in the area, so all electrons are actually collected and accelerated to the 'Delta Detector'. The limit at which low deflection angles give sufficient signal for imaging with the inlens detector is about 300 eV. Below 200 eV no signal from low deflection angles (high magnifications) can be detected with the inlens detectos, so below this energy nearly all scattered and emitted electrons from low deflection angles of the primary beam are collected towards the DD. The edge of the inner circle is sharp, indicating that all electrons from the sample are quickly accelerated onto parallel trajectories back towards the beam column. A second ring can be seen around the dark circle in the image and profile plot for 80 eV. We currently do not have a proven explanation for this, but it might be the result of second order scattering events at the edge of the inlens detector.

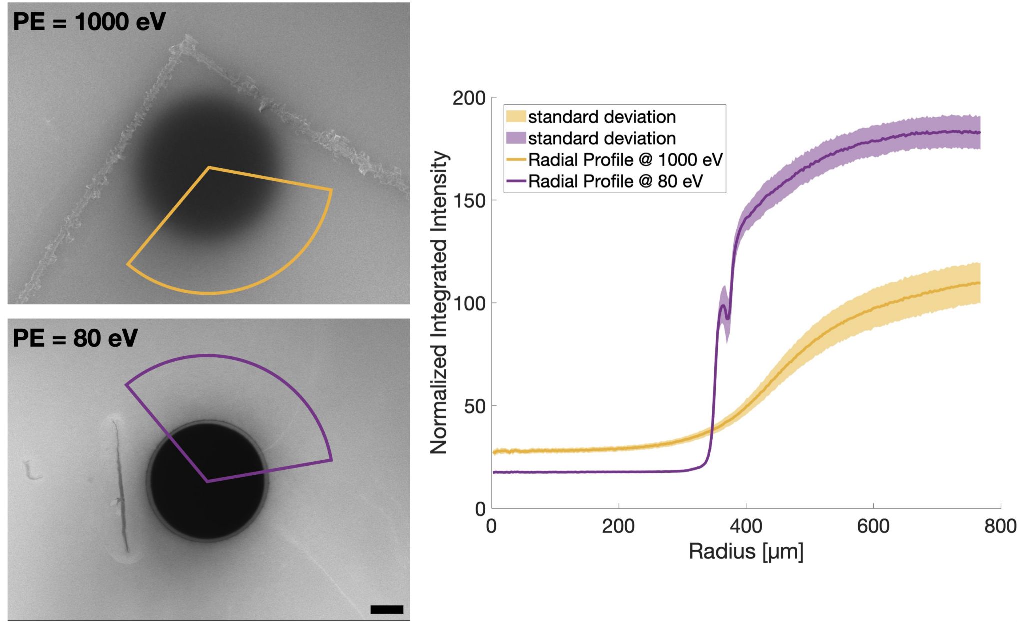


Figure 7.3: Left: Inlens detector Images of a Si-wafer at 1000 eV and 80 eV at lowest magnification (Scale bar equals 200 µm). Note that the dark central circle is diffuse at 1000 eV whereas it has a clear edge at 80 eV. Areas indicate the evaluation area of the radial profile plot using Fiji plugin 'Radial Profile Angle' (Schindelin et al. [2012]). Right: Radial profile plots of the indicated areas. For 80 eV the intensity increases from 5 % to 80 % over a radial distance of 85 µm. For 1000 eV the same increase is over 305 µm.

To summarize the findings of this chapter, we know that for higher magnifications (low primary beam deflection) – i.e. image size smaller than 300 µm – and primary energy below 200 eV all backscattered and emitted electrons are collected and accelerated towards the DELTA Detector. This is very important since we want to have all the information at the detector we are working with.
The working principle of the DD will be described in more detail in chapter 9. I have already studied a number of the properties of the microscope and especially the spectrometer within my master thesis (Ryklin [2019]), which was the starting point of this work. The main findings regarding the further work in this doctoral thesis were:

- The spectral response of the detector is dependent on the deflection of the beam (scan position) and hence image region. We called this effect anisochromaticity. This effect becomes small for large magnifications (and therefore small deflection angles). Below 10 nm pixel size the effect becomes negligible, all of the spectra recorded in this work are therefore well below the threshold.

- The spectral response is also dependent on the working distance and imaging

settings like contrast. Therefore these settings are kept as similar as possible throughout all measurements.

- The device - also due to its location in a dedicated room - is very stable against temperature change, magnetic stray fields and vibrations. However, we have shown that electronic instabilities can introduce systematic errors to spectral measurements, which are not always easy to detect. Therefore averaging over a larger number of measurements gives better results than increasing the scan time of a single measurement.
- The signal to noise ration for the BSE signal increases with decreasing primary energy. Therefore it is wise to choose a rather low landing energy.

Since my master thesis, we were able to gain more and more understanding in the spectral response of the detector setup and how to interpret the data in a meaningful way, what posed a significant challenge in this project. This will be discussed in detail in the following chapters of this part.

# 8 Challenges and Opportunities of Imaging at Ultra-Low Voltage

As described in the motivation to this work a big strength of ULV SEM lies in the extremely small interaction volume of the electrons with the sample. This way the signal is localized to nanometer range which gives high resolution with no signal mixing (see chapter 2). Of course we need to keep in mind that high surface sensitivity leaves us very susceptible to surface contaminations as well. In this chapter I first address to which extend surface contamination can be a limiting factor for our method. Afterwords I show and discuss imaging results on different samples proving the high surface sensitivity and showing advantages when imaging at ultra-low voltage. In the last section I discuss to which extend reducing the primary energy has an influence on the induced beam damage by electrons.

## 8.1 Handling Surface Contamination

Since we are not working under ultra-high vacuum (UHV) conditions – sample chamber vacuum is around $2 \times 10^{-5}$ Pa to $6 \times 10^{-5}$ Pa – we are always dealing with adsorbed hydrocarbon contamination on the sample surface. Before I can discuss any results on backscattered EELS, we need to show that surface contamination can be controlled within the experimental setup under the right conditions.
We need to distinguish two sources of contamination: One from the sample preparation and one from exposure to ambient environment conditions. Most common sample preparation for this work was drop-cast on a silicon-wafer. The more unintended residuals and contaminants are in the solution, the thicker is the contamination which is introduced by the preparation process. It is therefore very important to work with solvents and materials as pure as possible to avoid additional contamination from the preparation process. The other main source of contamination is particles – mostly hydrocarbons – from the environment which adsorb to the sample surface (Postek [1996],Vladar and Postek [2005]). This is unavoidable without sample preparation under vacuum or inert gas conditions and a corresponding transfer to the microscope. It helps to reduce the contamination by keeping the time under ambient conditions short and leave the sample under vacuum inside the microscope chamber for a couple of days to desorb part of the contaminants. But without UHV conditions for sample preparation and measurement a layer of contamination will always remain (Vladar and Postek [2005]).

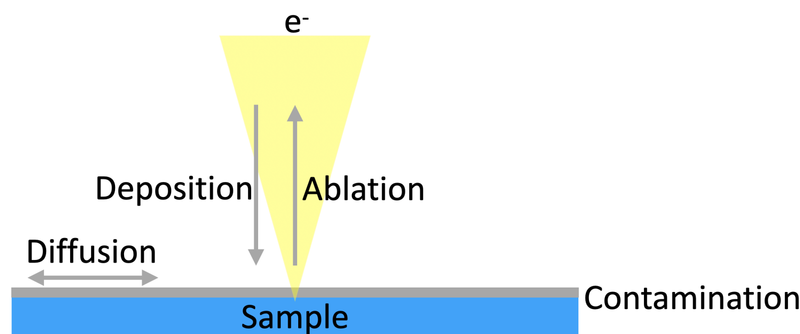


Figure 8.1: Electron beam induced processes affecting surface contamination.

Under irradiation of an electron beam three processes can happen as illustrated in figure 8.1. (i) New contamination can be deposited induced by the electron beam. This mainly occurs under bad vacuum conditions. Residual particles are then ionized by the electron beam and accelerated onto the sample leading to contamination growth (Reimer [1993],Vladar [1998]). (ii) Contamination can diffuse along the sample surface. This process is most prominently observed by the contamination frames build up around the imaging areas (see figure 9.1 (b)). Here the electrons induce a cross-linking of the hydrocarbons changing the viscosity and generating a concentration gradient. The contamination starts to diffuse along the gradient towards the imaging regions irradiated by the electrons. Once the molecules reach the imaging area they get cross-linked by the beam leading to a build-up of contamination around the imaging area. The width and height of the contamination frame is dependent on the initial amount of contamination on the sample and the scan rate (i.e. how fast the electron beam is scanning the image)(Reimer [1993]). (iii) The contamination can as well be removed by electron beam induced desorption and chemical etching (Materna Mikmeková et al. [2020],Toth et al. [2009]).
To interpret whether contamination is deposited or removed just by looking at the gray value change of the SEM images is not straight forward. For better understanding and clear evaluation we decided to use atomic force microscopy (AFM) to study the contamination dynamics induced by electron irradiation in the SEM. The experiments were performed by Franz Schmidt-Kaler as part of his master thesis in our group (Schmidt-Kaler [2021]). He exposed different substrates with time, dose and energy series and analyzed the induced change of the surface contamination with the AFM. One obstacle was to correlate the irradiated areas between SEM and AFM, which he solved by etching a pattern with a focussed ion beam onto the substrate for orientation in both instruments. Figure 9.1 shows the experimental setup and the readout of the AFM measurements.

For a detailed study of the contamination dynamics I refer to the master thesis Schmidt-Kaler [2021]. The most important result for this work is shown in figure 8.3. The AFM data show that for a range of primary energy from 50 eV to 2000 eV the contamination in the central part of the irradiated area is reduced since the effective surface height decreases. Thereby the largest reduction of contamination is

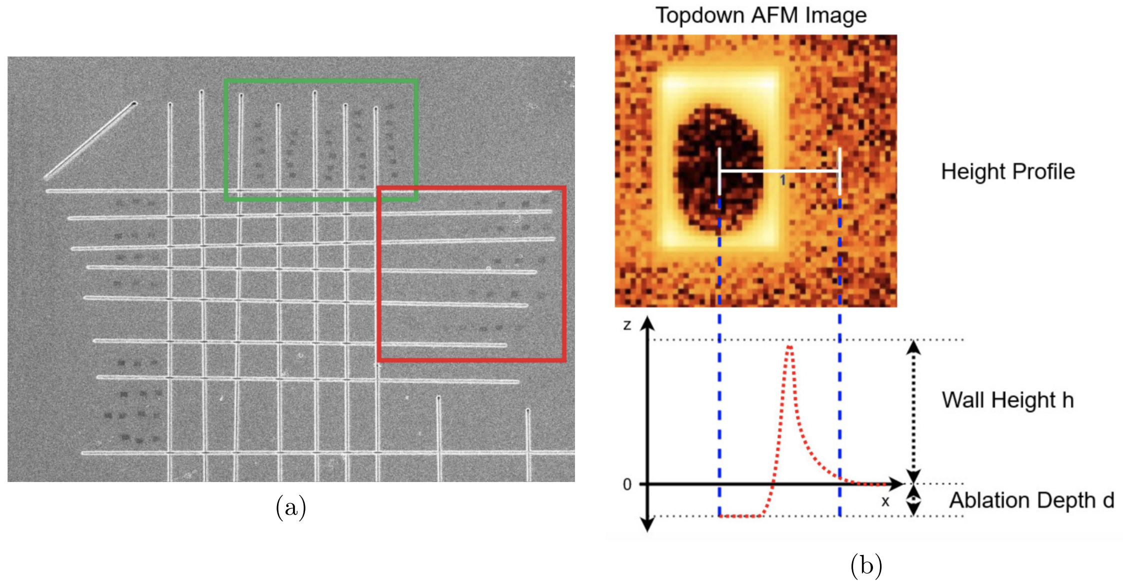


Figure 8.2: (a) Overview of the experimental setup for AFM study of beam induced contamination change in the SEM. A grid pattern was etched onto the Si-wafer to relocate and correlate the irradiated areas from the SEM to the AFM. One can see the frames irradiation series inside the pattern. (b) AFM image of an electron-irradiated region from the SEM – ablation depth and wall hight were extracted and analyzed for different SEM imaging conditions (Schmidt-Kaler [2021]).

seen for energies between 200 eV to 500 eV. The data also shows that if the sample is pre-treated with plasma and/or the vacuum conditions are improved by removing residual hydrocacrbons with a cryo-pump, the reduction of surface contamination is even enhanced. For best conditions at lowest energy of 20 eV the contamination in the central image part gets reduced as well.

It was important for us to measure and understand the dynamic evolution of the contamination under electron beam irradiation to know for which settings and experimental protocols we can expect the removal of contamination. At around 300 eV the ablation rate is the highest, which is in agreement with the experiments of Materna Mikmeková et al. [2020]. Since we use the spectrometer predominantly at 100 eV and lower landing energy, it is an important result that for a clean sample preparation and cryo-pumped vacuum system the contamination is ablated at energies down to 20 eV as well. Figure 8.4 shows this dynamics for beam irradiation at 20 eV primary energy. The first scan is clearly covered with contamination since little contrast can be seen of the underlying structure. With each scan, the central part of the image is cleaned of contamination while, as expected, a frame of cross-linked contaminants is building up around the center of the scanned imaging area. For this case, at scan 6 to 8 the highest contrast of the origami structure is

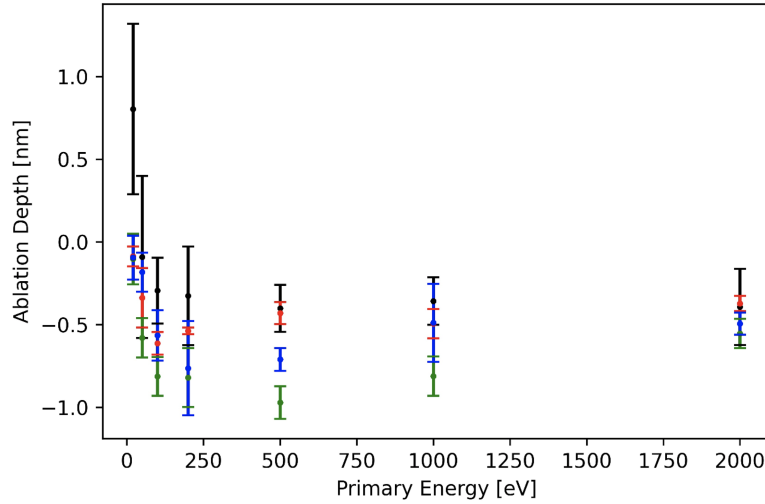


Figure 8.3: Ablation of contamination in the central part of the SEM image versus primary beam energy under different conditions: black – normal chamber conditions, no sample treatment; red – improved vacuum by factor 2 with $LN_2$ cooled cryo-pump; blue – sample treated with plasma inside the microscope before irradiation; green – plasma-treatment before irradiation and improved vacuum with cryo-pump.
Irradiation time was 10 min at 100 pA and 0.62 nm pixel size, corresponding to 1.24 million electrons per nm$^2$.

reached[1], corresponding to an electron dose of about $15 \times 10^3$ electrons per nm$^2$. Afterwards the contrast decreases again indicating that the structure is damaged. The effect of beam damage at ultra-low voltage is discussed in section 8.3. To put it into perspective: To record a spectral image series with sufficient signal to noise ratio an electron dose of $5 \times 10^3$ to $30 \times 10^3$ electrons per nm$^2$ is needed depending on the primary energy and the required energy range.
It is important to note that the contamination dynamic is dependent on the scanning parameters as well, especially the scan speed or frame time – so the time which the electron beam dwells on a pixel and the time until the beam reaches that pixel again after scanning the rest of the image. This effects the diffusion of contaminants as well as the temperature progression influencing the physics (diffusion) and chemistry (damaging / polymerization of molecules) at the image area.

To conclude this section, we have shown that inside our microscope the electron beam can be used to remove contamination from the imaging area with beam energies down to 20 eV, enabling us to record images and spectral image series on a clean surface at lowest energy.

[1]The imaging properties at ultra-low voltage will be discussed in more detail in the next section.

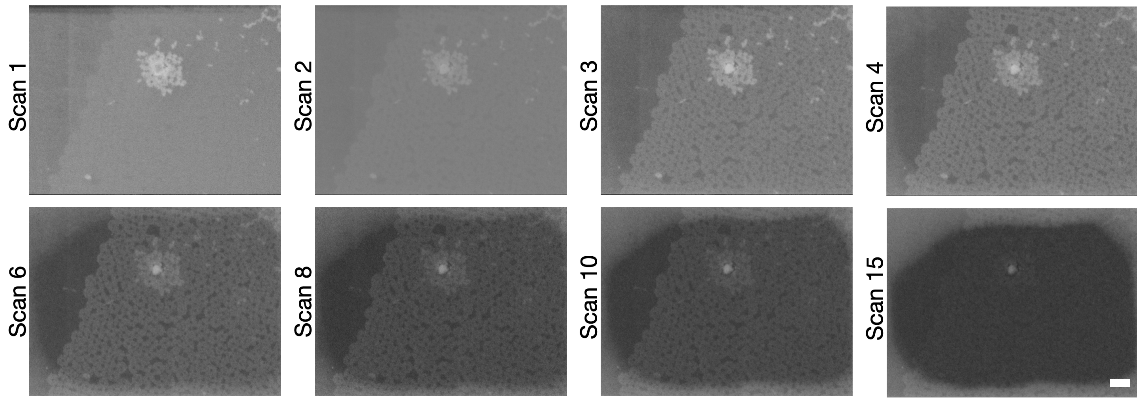


Figure 8.4: Images of DNA-Origami platelets on Si-wafer after different numbers of scans. Each scan equals a dose of 2800 electrons per $nm^2$. At the first scan, the image is clearly blurry due to overlying contamination. With increasing scans, the contrast of the Origami increases – the contamination in the central image region reduces and the contamination frame at the edges builds up as expected. At scan 15 the contrast of the origami vanishes due to beam damage. Scale bar (frame scan 15) represents 100 nm.

## 8.2 Examples of Unexpected Image Contrast and Surface Sensitivity

Working at ultra-low voltage means extremely small interaction volume. In this section I want to illustrate with examples what that means for imaging in the SEM. If not stated otherwise, the images are recorded with the 'Delta Detector'. For 'backscattered electron image' the grid voltage was set to a value to filter out the secondary electrons, typically to −50 V. It is important to note that the grid filter can naturally only filter electrons with a lower energy than the threshold set by the filter, so there is no way to image only secondary electrons without backscattered electron signal in this setup. For convenience – since the secondary electron signal in most cases predominates the backscattered signal, I discuss this in chapter 9.2 – I will call images containing the SE signal 'secondary electron image' although also BSE contribute.
The used samples and their preparation are described in section 6.1.

### 8.2.1 Polycrystalline Gold

Figure 8.5 shows a polycrystalline gold surface imaged with different parameters. All images are acquired with the same electron dose (2000 electrons per $nm^2$). The BSE image at 1000 eV taken with the spectral energy filter detector does show little to no contrast. The main reason for that is that there is no material contrast – everything is gold – and the interaction volume of the backscattered electrons is larger than

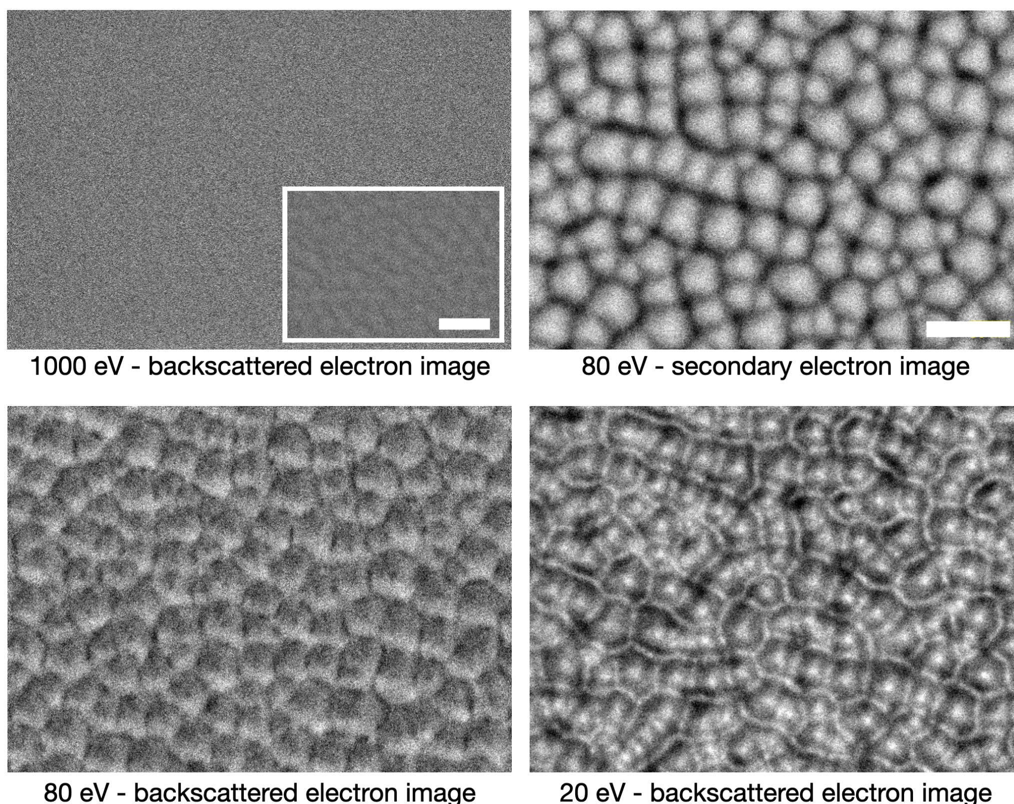


Figure 8.5: Images of a polycrystalline gold surface under different imaging parameters. Backscattered electron image at 1000 eV (conventional SEM energy) shows no contrast in the spectral energy filter detector. Inset image at 1000 eV is recorded with the inlens detector in parallel and shows the gold domains and that the image is in focus. Note that all images are acquired with the same electron dose – contrast changes drastically under different imaging parameters at ULV with the spectral energy filter detector. Scale bars represent 100 nm.

the structural features of the sample. The inset inlens image does however show some weak contrast. This can be explained by the arrangement of the detectors described in chapter 7. The inlens detector detects primarily the electrons scattered at a higher angle with respect to the primary beam. Therefore high topography on surfaces give more contrast in the inlens detector due to shadowing of the 'high scattering angle' electrons from lower areas (topography effect).
The lower left panel of figure 8.5 shows an image recorded at 80 eV filtered for backscattered electrons. Obviously the image shows a lot more contrast and details compared to the 1000 eV image, which makes a lot of sense considering the small interaction volume of the electrons. The domains of the polycrystalline surface are nicely resolved. Interestingly all grains are brighter on the lower face than the upper face. This is a systematic error or feature of the detector and I will explain it in more detail in chapter 9. At this point it is important to know that for samples with

rough topography, more or less electrons are detected depending on the orientation of the topographic face. As in this example, more electrons are detected if the face shows to the bottom of the image compared to if it shows to the top. This is an effect of the asymmetry in the detection beam path. We have to take this into consideration since it introduces a systematic error for the spectroscopy as well, which is the reason we have so far primarily done experiments on flat samples with little to no topography.
When the secondary electrons are not filtered out but included in the signal, we get the image on the upper right panel of figure 8.5 at 80 eV landing energy. With secondary electrons the grains of the polycrystalline surface look very homogeneous and clearly separated by the grain boundaries, where little signal is generated. It is a notable observation that although only about 60 eV are separating the BSE and SE signal at this energy, the contrast generated is that different. Besides the apparent difference in signal acceptance of the detector between SE and BSE at this energy, the difference in signal depth between BSE and SE can as well be seen in particular comparing the width of the dark grain boundaries.
At 20 eV (lower right panel in figure 8.5) backscattered and secondary electrons are not distinguishable (see chapter 9.2) but we assume that primary backscattered electrons contribute more than SE. The contrast change is impressive and was very unexpected. Whereas at 80 eV for BSE as well as for SE the grains are bright throughout the surface and the boundaries give little signal, at 20 eV now just the tip of the grains is bright and in contrast to what was observed before the grain boundaries are bright as well and the area in between is darker. At this point we do not have a proven explanation for this contrast mechanism. It could be that the effect also has to do with systematic acceptance deviations of the 'Delta Detector'. However, this explanation seems unlikely since the energy of all detected electrons is close together at 20 eV PE. It is a very interesting observation which definitely needs more experiments on different crystalline surfaces, unfortunately this would have gone in a different direction at this point and for this thesis I wanted to focus on backscattered EELS.

### 8.2.2 Flat DNA Origami Platelets

I have discussed in the motivation of this work that one intriguing aspect of ULV imaging is the backscattering coefficient for light atoms, which increases with decreasing electron energy (section 4.2.1). It makes our approach especially interesting for carbon, organic and biological materials. In order to study the imaging properties on organic samples as well as the surface sensitivity of ULV imaging, we selected for this flat DNA origami platelets and prepared them on a Si-Wafer substrate (for sample preparation details see section 6.1).

Figure 8.6 shows the imaging results for different PE. At 1000 eV it is hard to see any contrast although the 20 nm gold fiducial on the upper left side shows that the image is in focus. There actually is a carpet of origami as is visible in the 500 eV and 200 eV images. However, for higher PE the signal is dominated by the silicon

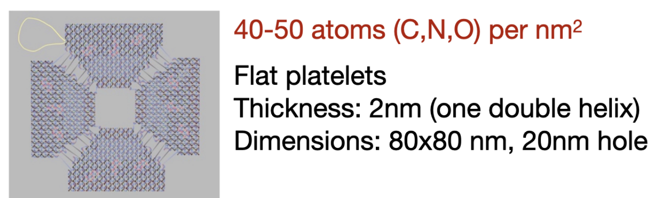


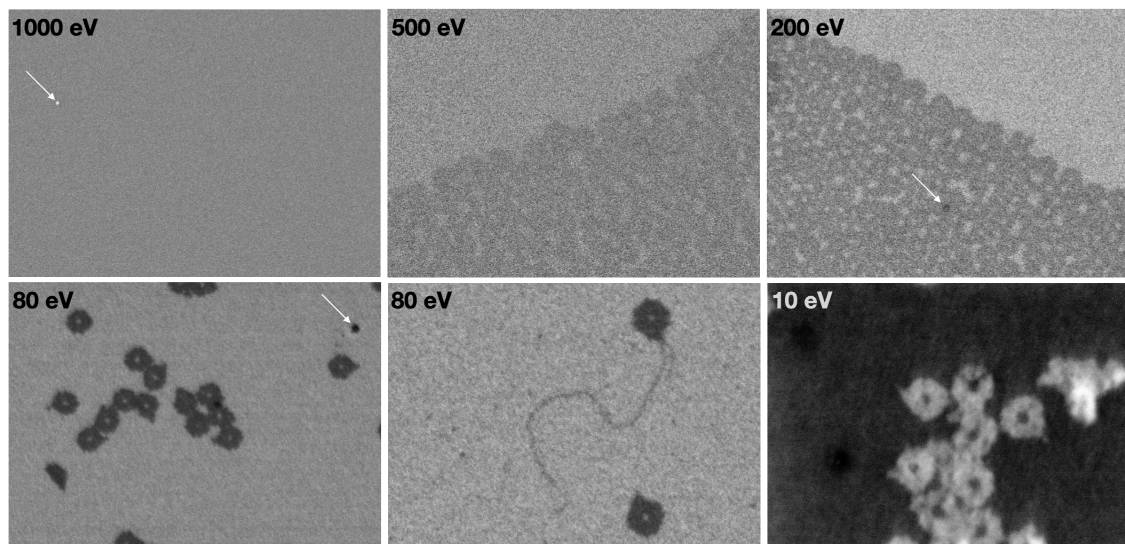


Figure 8.6: Top: Schematic and dimensions of the used DNA origami in this study (kindly provided by May Tran from AG Prof. Kerstin Göpfrich). The yellow string in the schematic represents surplus unfolded DNA material, which can also be observed in the images. Below are images of the origami on Si-wafer substrate recorded with different primary electron energies and filtered for backscattered electrons. The image at 1000 eV (conventional SEM energy) shows almost no contrast although it is in focus. White arrows point to gold fiducials. (The size of the origamis are 80x80 nm providing an intrinsic scale bar).

substrate due to the large interaction volume at this energy. The images show how the contrast increases with decreasing energy. At 500 eV the origami are still very blurry and the signal is dominated by the silicon support. At 200 eV the contrast is quite good already so that the edges and the hole of the origamis can be resolved. At 80 eV we get the strongest contrast, which is also the reason we performed most of our spectroscopic studies at this energy. The contour of the origamis is clearly resolved, in some cases – especially in the left image at 80 eV – even the cross-like spacing in between the four triangles of the single origami is resolved. This is quite astonishing since there still is DNA material but with a lower density. The origamis have surplus unfolded DNA which accumulates at one corner of the structure, these are nicely resolved in the 80 eV images as well. In the image shown in the middle of the lower row of images in figure 8.6 the DNA double helix appears to be pulled out over the substrate, which is resolved as well. All this shows the power of imaging at

ULV. The Origami are just 2 nm thick and the contrast and resolution at 80 eV can to our knowledge not be reached with any other electron microscope.
The image shown at 10 eV shows a contrast flip (figure 8.6, lower right panel). At this energy it is not possible for us to distinguish between BSE and SE signal. The image still shows amazing contrast against the substrate and most features are still resolved, although more artifacts from charging are present as well. As already mentioned in the discussion of the gold surface, it would be very interesting to further study the interaction and contrast mechanisms below 30 eV PE achievable with this special microscope, but it is not part of this work.
I want to point out that the bright signal of silicon compared to the dark organic origami (mostly carbon) is in agreement with the backscattering coefficients for these materials, although silicon has a higher atomic number than carbon (see section 4.2.1). In the images some gold fiducials can be found which are bright at 1000 eV, have similar brightness at 200 eV and are darker than the origami at 80 eV. This is in agreement with the trend of the backscattering coefficient for gold compared to silicon and carbon as well.

### 8.2.3 Graphene

For the last example we move from 2 nm thick origami platelets to single atomic layer graphene, with a thickness of about 0.3 nm. Graphene actually was one of the first specimen I started to study within this work. It is of interest because as a flat, single atomic layer carbon material it was perfect to test the surface sensitivity and signal depth. Additionally it has been studied extensively in TEM EELS measurements, so it is a good starting point for spectroscopic studies as well (Kapetanakis et al. [2015], Wachsmuth et al. [2014], Eberlein et al. [2008]). Figure 8.7 shows free standing monolayer graphene flakes on carbon quantifoil. Several observations can be made looking at the images. The graphene in the 1000 eV SE image appears dark not only where free standing above the holes, but on the support as well. This indicates that a significant fraction of the primary electrons do not interact with the graphene to produce SE. The SE generated in the quantifoil layer underneath can not escape through the graphene layer which is why the image is darker in this areas as well.
At 200 eV more electrons interact directly with the graphene layer, the SE image shows little contrast between the flake and the support, indicating that more SE are generated directly in the graphene layer. The holes are still darker, so a part of the electrons do not interact with the graphene layer. Interestingly, the BSE image at 200 eV does show almost no difference in contrast from above the hole to above the support, so the majority of Electrons is backscattered from the graphene layer the same way as from the thicker support layer. In contrast, at 600 eV the graphene sheet shows less backscattering compared to the support substrate.
At 30 eV there is not a lot of difference in between the image filtered for BSE and the image including SE. The BSE image actually seems to map the topography and surface roughness more than the SE image, which is opposing to conventional SEM

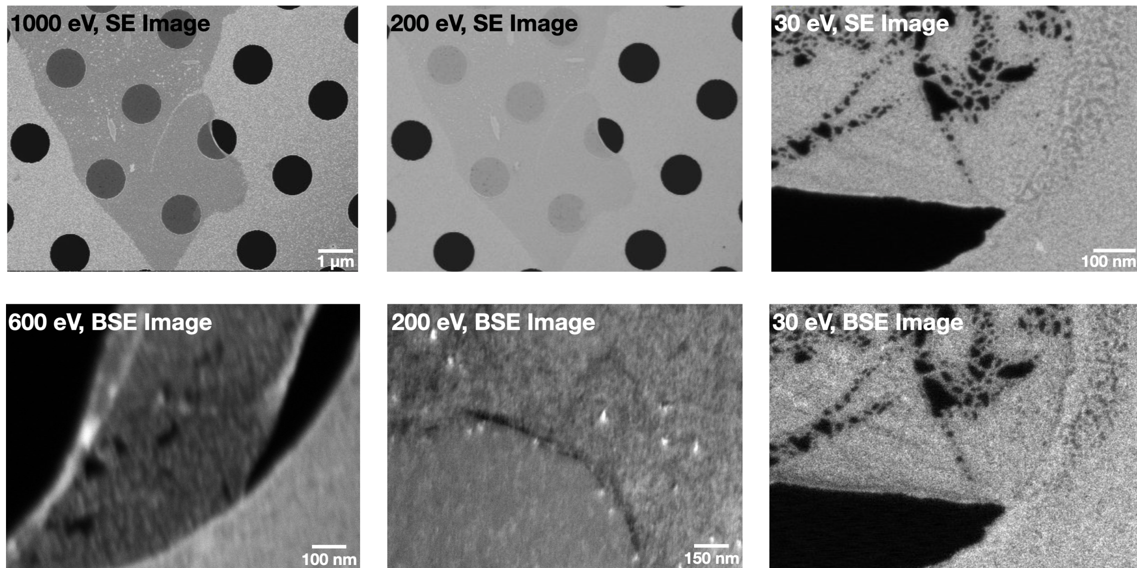


Figure 8.7: Graphene on carbon quantifoil imaged with different parameters.

energy above 1 keV where the SE carry the topographic information. The surface roughness hints at contamination present on the surface, which actually was a serious problem with these samples. I will discuss this in more detail when I come to the spectroscopic results in section 11.1.

We did also try different substrates for the graphene flakes, which is shown in figure

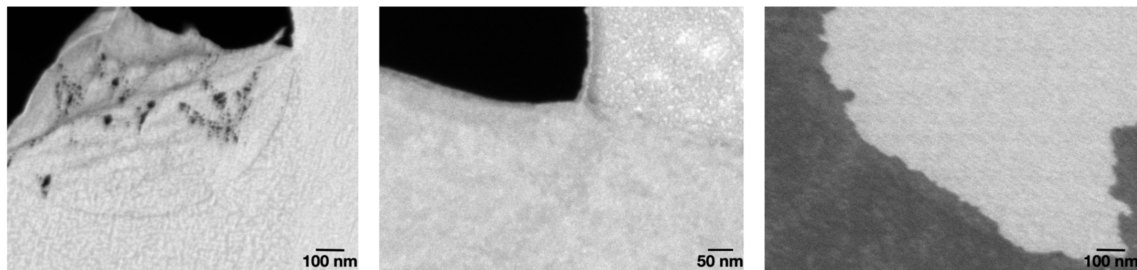


Figure 8.8: Graphene flakes on different substrates images at 80 eV PE and filtered for BSE. Left image is on carbon quantifoil substrate, middle image on gold quantifoil, right image on silicon wafer.

8.8. Graphene on carbon quantifoil is carbon on carbon. It will be interesting to see how spectra of these materials differ, but the BSE images do not show any intensity contrast despite of surface roughness which enables us to tell where the graphene flake is in the image. For graphene on gold quantifoil there is more intensity contrast, however, there is also a lot of contamination apparent so it is difficult to tell how much of it is 'real' carbon vs. gold and how much is contamination. For the silicon wafer surface it looks completely different. We saw already for the Origami images in part 8.2.2 that silicon has a much higher backscattering coefficient than the organic origamis. The same can be seen here for graphene which appears dark in contrast

to the silicon support. To emphasize, we are looking at a few atomic layer of carbon (if we assume some contamination is present) and clearly the majority of electrons are backscattered from these few atomic layers giving the high contrast in the image.

### 8.2.4 Summary of the ULV Imaging Observations

With this prototype microscope a whole new energy range down to 10 eV is accessible for high resolution imaging. With the three examples above I wanted to point out and show how ULV imaging affects the signal and contrast compared to standard SEM energy. Here I want to summarize the observations:

- While the secondary electron signal always originates from the first few atomic layers due to their low energy, below 200 eV primary energy the penetration depth of backscattered electrons gets similar to the range of SE. Below 100 eV there is no indication for a difference in signals depth between BSE and SE in the examples shown.

- With our detector setup, backscattered electrons actually give more topographic contrast than secondary electrons. This results from the inhomogeneity of the grid potential at the Delta Detector and will be further explained in chapter 9.

- Due to the small penetration depth and interaction volume we get unprecedented contrast for thin films and materials.

- The backscattering coefficient for light atoms generally increases with decreasing primary electron energy which leads to better signal to noise ratio for the imaging of organic materials. Also, the large range of accessible primary energies allows to pick different energy points at which the contrast between different materials gets maximal.

- The small interaction volume increases the resolution since the generated signal is confined to the small volume.

- at lowest PE ($<$30 eV) the BSE and SE signal gets mixed (overlapping energy ranges). At this energy we observe interesting contrast changes and scattering mechanisms like the strong signal from crystalline grain boundaries, which will be interesting to further study in the future.

## 8.3 Beam damage

Beam damage is – and always was – a limiting factor in electron microscopy studies. However, it actually is not easy to measure the extend of beam damage. To quantify beam damage usually a 'critical dose' is specified at which a defined resolution or amount of detail is lost. The critical dose of course is dependent on the primary electron energy: How much energy can be transferred from the incoming electron? But it is also dependent on the specimen: How beam sensitive are the atomic and molecular bonds in the specimen, at which transferred interaction energy do they break? Then, secondary damage effects play a large role as well: How much heat is generated in the sample by the beam? Are radicals formed which further damage the sample? Is the sample charging and thereby electrical and mechanical stress introduced? In addition, depending on the vacuum condition, gas-mediated electron beam induced etching can be a cause for indirect beam damage.
Some of the damage effects can be reduced by cryogenic sample cooling or sputter coating for better conductivity for example (Knapek and Dubochet [1980], Egerton et al. [2004]). Another trend over the last decades in TEM imaging and spectroscopy – enabled with improved electron sources and electron optics – is the reduction of primary energy from hundreds to tens of keV to increase the critical dose and reduce beam damage (Linck et al. [2016]).
With the Delta SEM we reduce the primary beam energy – compared to TEM – another three orders of magnitude to tens of eV. The question now is: Can we measure and quantify how reducing the primary energy under 1 keV affects the beam damage? In the SEM we can not follow the beam damage of a structure on molecular or atomic resolution like in the TEM, therefore we need another readout we can follow and decided to use organic fluorophores as this marker. Since a big strength of the DELTA is the application to organic and biological materials, it made sense to test the beam damage on a organic material. In addition, fluorescence imaging is quite easily accessible and we can correlate the surviving fluorescence after electron beam irradiation with the induced beam damage.

The first approach was carried out by our master student Lukas Bange. (Bange [2020]). He used 'Rhodamine B' as a fluorophore and mixed the fluorescent marker into epoxide resin in order to cut sections with a distinct thickness. Figure 8.9 shows the measured survival rate of the fluorescence after electron irradiation in the SEM in dependence of the electron dose for different primary energies. An obvious trend can be seen - with decreasing primary energy more fluorescence survives the electron irradiation. However, for all energies beam damage was still introduced with the smallest irradiated dose and it increased with increasing dose – as we would expect. By using thin sectioned slices the fluorescence was confined to a thickness of only 60 nm. However, at lowest primary energy this is still significantly thicker than the penetration depth of the electrons, as is shown by the Monte Carlo simulations of the electron scattering performed with 'Casino' in figure 8.10. This leaves an open question, whether the survival rate increases because of lower primary and secondary

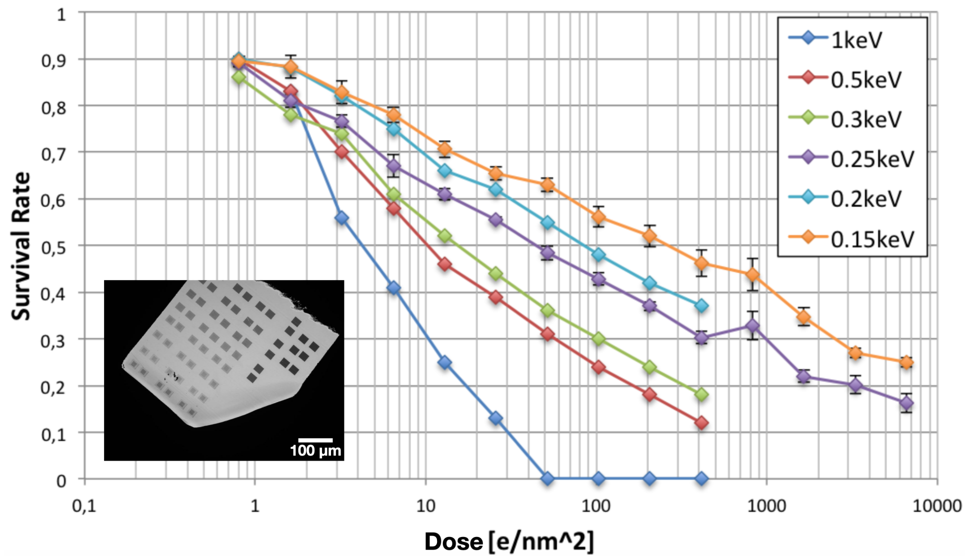


Figure 8.9: Electron dose plotted agains the survival rate of Rhodamine B fluorescence after electron irradiation in the SEM for different primary energies. Rhodamine B was embedded in Epoxide resin and cut in 60 nm sections. Inset image shows a section with irradiated areas. Bange [2020]

beam damage, or if just less volume is damaged by the electron beam and therefore the fluorescence of the not penetrated volume increases the measured survival rate with decreasing penetration depth.
To test this I studied another fluorescent sample where the fluorophores were attached as a monolayer at the sample surface. The sample and the results on the survival rate study are shown in figure 8.11. The results show the same trend as the survival rate measurements for Rhodamine B ultra-thin sections. For the monolayer we see that for 80 eV and 40 eV the survival rate further increases, so beam damage is further reduced, compared to 150 eV. So despite smaller penetration depth – more electrons interact with the surface layer – the beam damage on the surface fluorophores is reduced at lower beam energy.
This experimental setup is not perfect either, because the PETA is fluorescent at the excitation energy of Cy5 as well. Nevertheless we were able to detect the fluorescence change of the Cy5 fluorophores to measure the survival rate on the surface layer. More details on the measurement and data analysis can be found in sections 6.1.8 and 6.2.1.

We need to keep in mind that direct electron interaction is not the single cause of beam damage and a significant source of beam damage is electron induced chemical etching, since we are not working under UHV conditions. Nevertheless our data clearly shows that the total damage decreases with decreasing energy even on beam sensitive organic materials, hence ULV SEM benefits studies of beam sensitive materials.

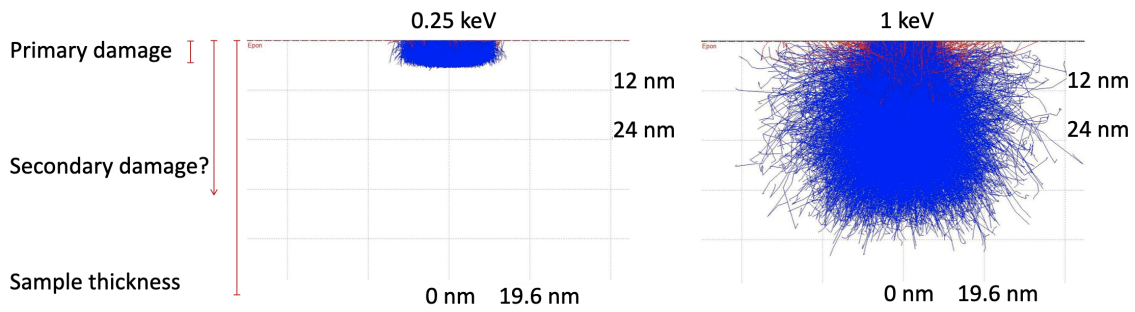


Figure 8.10: Monte Carlo simulation of the penetration depth of electrons in epoxide resin. While the electrons penetrate almost the entire 60 nm section at 1 keV, only about 10 nm are reached at 250 eV.

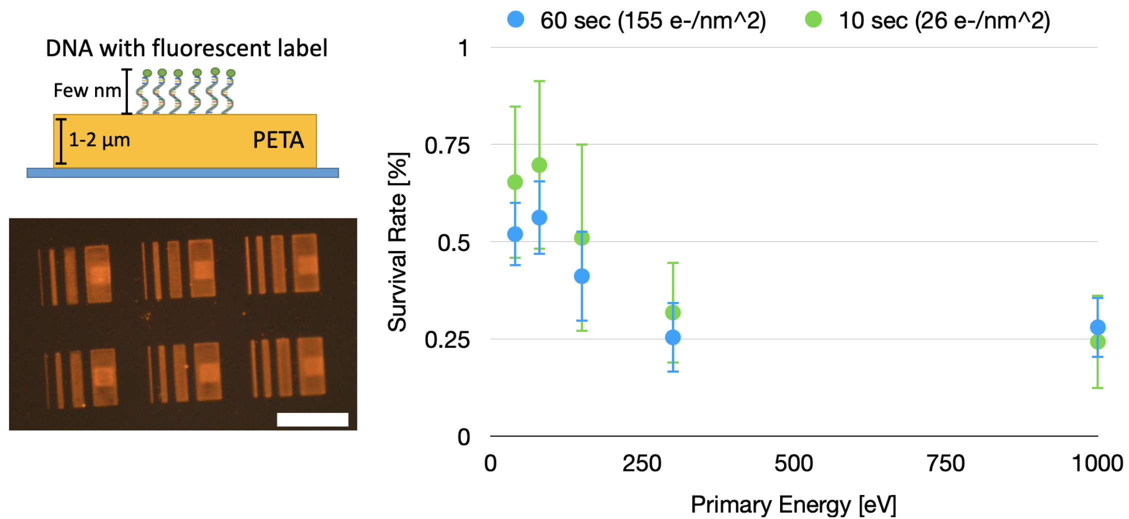


Figure 8.11: Left: Schematic of the sample and a fluorescence image of the structures. Cy5 is used as fluorophore. Right: Survival rate of the fluorescence plotted as a function of the primary electron energy for two irradiation times. Scalebar represents 20 µm.

# 9 Spectroscopy with the Delta Detector

In section 8.2 I have described the opportunities of imaging at ULV and also, how electron energy filtering for BSE by excluding SE enables to image samples with different contrast mechanisms. Our goal is to use the Delta Detector to obtain electron energy loss spectra with backscattered electrons equivalent to established methods like HREELS and TEM EELS. The current setup of the detector unfortunately has some problems complicating the measurement and interpretation of the recorded electron spectra. In this chapter I want to introduce and explain the problems and the properties of the Delta spectrometer and discuss, how we nevertheless can approach bsEELS and interpret the measured data in a meaningful way.

## 9.1 Energy Resolution and Energy Spread Function

The spectrometer of the Delta microscope consists of an energy filtering grid-system in front of a single pixel scintillator detector (long scintillator plate without spatial resolution of the detected electrons). A retarding potential is applied to the grid-system filtering the incoming electrons by their kinetic energy. By adjusting the retarding potential stepwise a cumulative electron energy spectrum can be recorded. Differentiation of the cumulative spectrum gives the energy loss spectrum of the detected electrons.

Figure 9.1 illustrates the working principle. An image stack is recorded with decreasing detector grid voltage, so for each grid voltage step more electrons reach the detector since lower energy electrons are accepted with each grid step. Typically the start voltage is set higher than the primary electron energy, so the onset of the elastic backscattered electron peak can be recorded. If the grid voltage is run up to zero, lowest energy electron can reach the scintillator so also the secondary electron peak is recorded.

The major problems with this setup are: (i) the beam path towards the grid is not corrected, hence electrons are spread out along the beam path dependent on their energy and distance from the electron optical axis. (ii) The retarding grid potential is not homogeneous, so dependent on the position the electrons arrive at the grid they experience different potentials which spreads out the energy acceptance at the detector and therefore the energy resolution in the recorded spectral image stack decreases.

Figure 9.2 illustrates the problem. The primary electrons are focused on the sample and the probe ist scanned over the sample to take the image. Now the backscattered electrons do not leave the sample straight on the beam axis, but get scattered in all directions. They are collected by a electric potential towards the pole piece back in

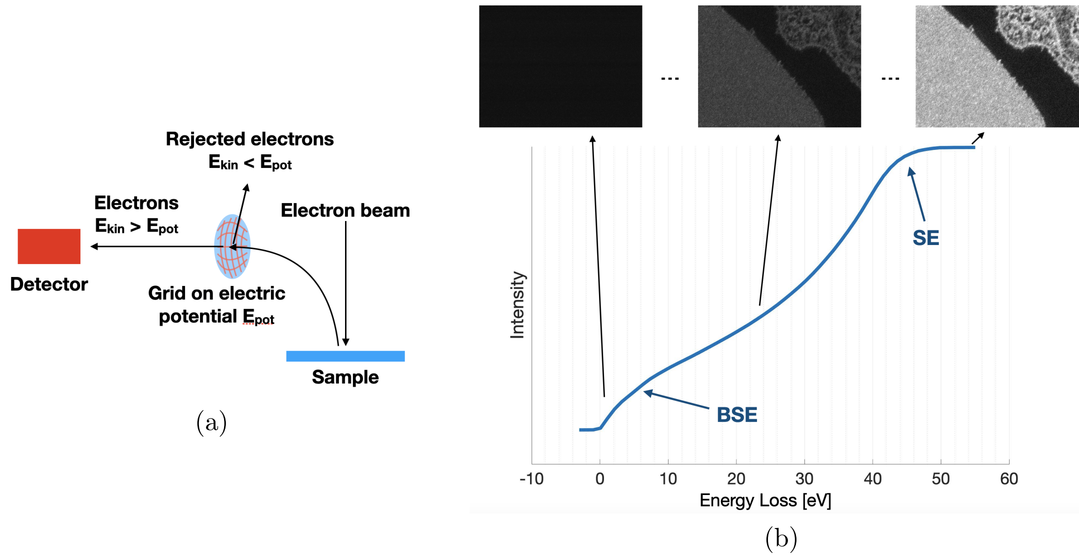


Figure 9.1: (a) Scheme of the working principle of the retarding grid spectrometer. The grid system is set to a voltage giving an energy potential which only electrons with sufficient kinetic energy are able to pass. By running the grid potential stepwise from the energy of the primary electrons to a target end step, an image stack with the information of a cumulative energy spectrum is recorded, which is illustrated with an example measurement (b). Two onsets can be seen, one is the elastic and inelastic BSE signal at zero/low energy loss, one the SE signal at highest energy loss.

the beam splitter. However, as the figure illustrates, they will have an off-axis distribution due to all possible scattering angles. This off-axis distribution will be larger at higher primary energies, since the backscattered electrons have more energy to spread out before they are bent onto the beam path. Additionally, the interaction volume is larger at higher energies, hence electrons leave the sample from a larger area. This not only increases the beam spread back to the detector, but also degrades the resolution since the interaction volume is larger than the probe size. This explains the effect that our energy resolution is worse at higher primary energy and better at lowest energy.
Backscattered electrons also have different energies due to their elastic and inelastic interaction with the sample. The beam path towards the detector is not corrected which leads to an additional spread of the backscattered electron beam towards the detector, however only in one direction.
The backscattered electrons arrive at the delta detector with a homogeneous spread due to scanning and scattering angle and a directional spread along one axis due to energy spreading of the bent beam path and see a non-homogeneous retarding potential of the energy filter. This leads to significant errors in the energy detection of the incoming electrons and a limited energy resolution.

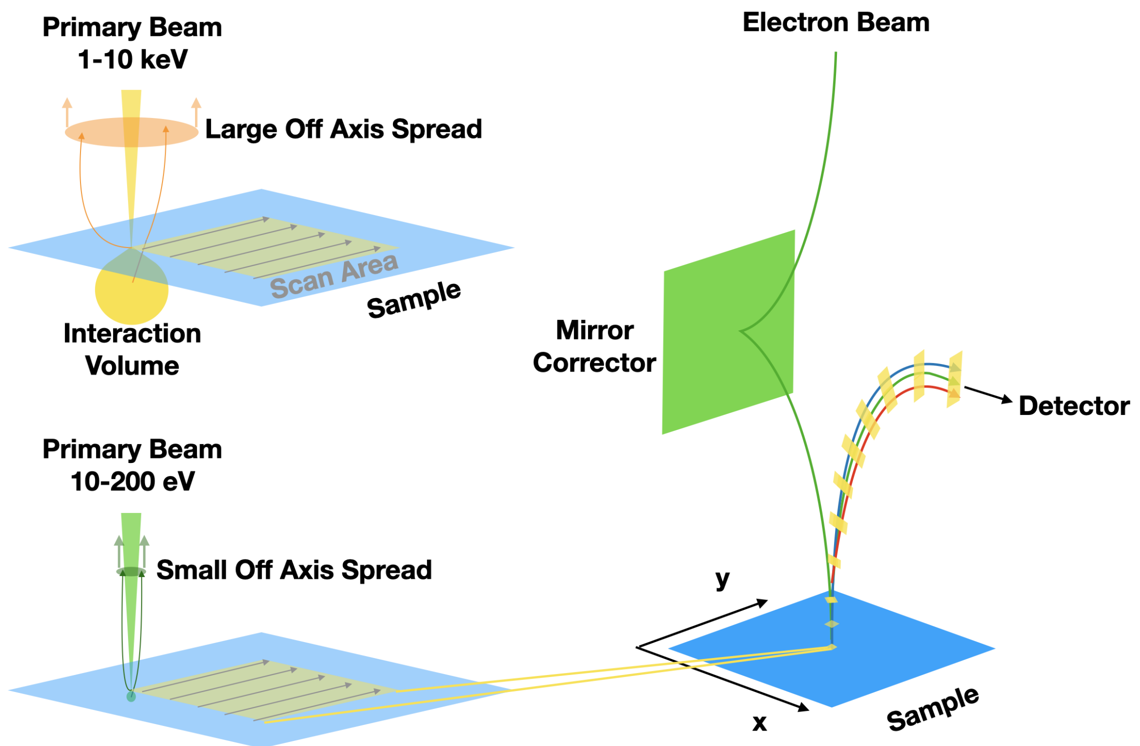


Figure 9.2: Schematic of the beam path towards the Delta Detector. Left side demonstrates the electron backscattering from the sample – the interaction volume and off-axis spread is much larger for conventional primary energy (top) compared to ultra-low voltage (bottom). Right side demonstrates the energy dependent spread due to Lorentz force on the beam path towards the detector.

More by chance, I was able to probe the spectral response of the detector system. While studying graphene spectra on a quantifoil grid, I came over a larger defect in the quantifoil which showed strong charging behavior at 20 eV landing energy and appeared to display the grid structure of the Delta Detector. Figure 9.3 shows the charged area. Negative charge seems to accumulate at the larger defect hole leading to a potential at which the primary beam is mirrored. This way each image point in the charged area is reflected to a single trajectory on the beam path. The whole charged, reflecting area depicts the retarding grid system through which all the trajectories go at different positions. For an uncharged sample, the scattered electrons from each image point can take different trajectories in which case the backscattered electrons from one image point path the grid as many different trajectories and not only one an in the mirrored case. This is schematically illustrated in figure 9.4.

If we analyze the spectrum recorded from the mirrored area of the defect, as shown in 9.3, we see that the spectral response of each trajectory through the grid system is very different. Optimally, we would like to have a delta-peak shaped response with an energy spread of the bandwidth of the Schottky FEG, since the beam is

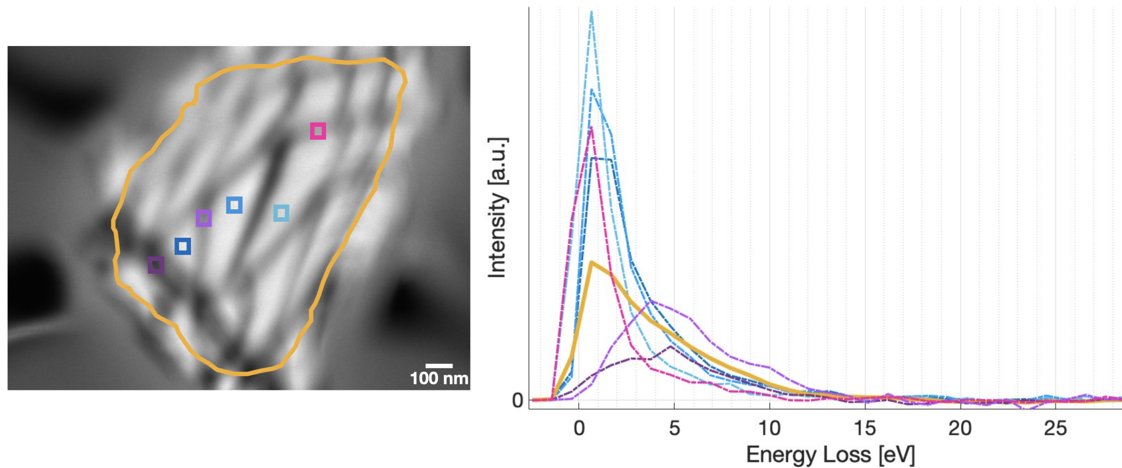


Figure 9.3: A defect in a quantifoil hole gets charged and acts as a mirroring potential and thereby mapping the beam path through the grid system. Left image shows the charged area at the end voltage of the corresponding spectra at the right taken at 20 eV landing energy. Right spectra show the signal produced by different regions on the grid path and a averaged spectrum over the whole grid.

just reflected at the surface. The grid systems, however, introduces an energy and amplitude shift depending on the trajectory through it, which makes the interpretation of the spectra recorded with this setup difficult and they always need to be interpreted carefully under these restrictions. Nonetheless we can assume that for scattering from an uncharged sample, the signal response of the system in the first approximation will be an average over all possible trajectories represented by the 'full' spectrum as seen in figure 9.3 and we will see, that this assumption allows us to interpret our data in a meaningful way. This 'full' response spectrum of the detector system will be taken and referred to as the 'energy spread function' (ESF, named in the style of the point spread function for imaging) of our detector system. In chapter 9.3 I will describe how the ESF is used to interpret recorded spectra of different materials. Before that I want to share some measurements and findings regarding the distinction of secondary and backscattered electrons in chapter 9.2

I want to point out at this point that this considerations on the beam trajectories and detector response discussed in this section will be important in the discussion on possible improvements of the detector setup in the outlook (section 14.2).

Figure 9.4: Schematic representing the difference of a mirrored beam to scattered. The left side shows the charged defect at which the mirrored beam only takes one trajectory, so all electrons of an image point arrive at one point on the detector system. In contrast, for a scattered beam (right image) all trajectories are possible dependent on scattering angle and energy, so in general electrons from each image point can arrive on the whole detector surface.

## 9.2 Ratio and Distinction of Backscattered and Secondary Electrons

So far most of the literature regarding SEM distinguishes BSE and SE by means of their energy - most commonly defining all signal electrons below 50 eV as secondary electrons (Seiler [1983]). This distinction naturally runs into problems if the primary electrons themself have an energy of 50 eV and below.

With our approach we are for the first time able to show how the signal of BSE and SE separates at primary energies below 100 eV and also how the signal intensity of both electron signals depends on the primary energy and observed specimen.

Figure 9.5 and 9.6 show electron energy spectra of $SiO_2$ and $Au$, respectively, for energies between 16 eV and 50 eV. The data shows that below 50 eV the main signal of BSE (left peak at zero energy loss) and SE (rightest distinct peak) can clearly be distinguished down to a certain, material dependent point. To which extend 'low energy' BSE contribute to the SE signal and vice versa 'high energetic' SE to the BSE signal is more difficult to tell and at a certain energy the signals get clearly mixed.

Interesting is the development of the ratio between BSE and SE peak which inverts between 30 eV and 26 eV for $SiO_2$ and between 40 eV and 35 eV for $Au$. Comparison of SE and BSE images is already a useful approach in conventional SEM studies (Zhang et al. [2016]), however, the images are taken with separate detectors and highly different signal ratios and therefore signal to noise ratios as well. Our approach allows to record BSE and SE signal with the same detector at similar signal intensities which makes comparing the signals and further image processing easier. Moreover, the ratio development of BSE and SE might serve as additional input for material mapping and characterization.

Figure 9.7 shows the ratio of signal intensity between SE and BSE for $SiO_2$ and $Au$ plotted against the primary energy. It needs to be noted, that the SE intensity is

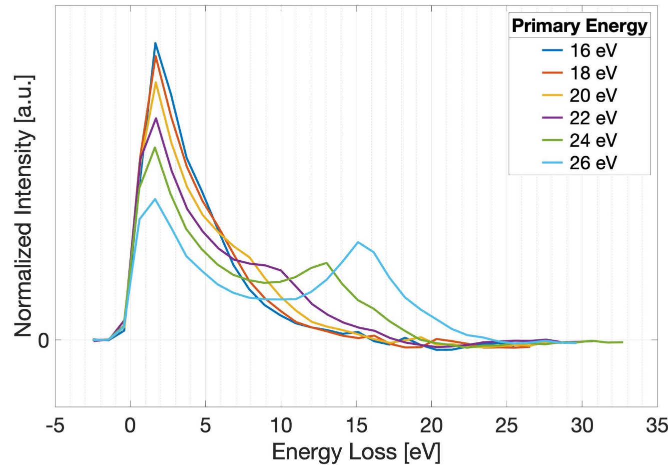


(a)

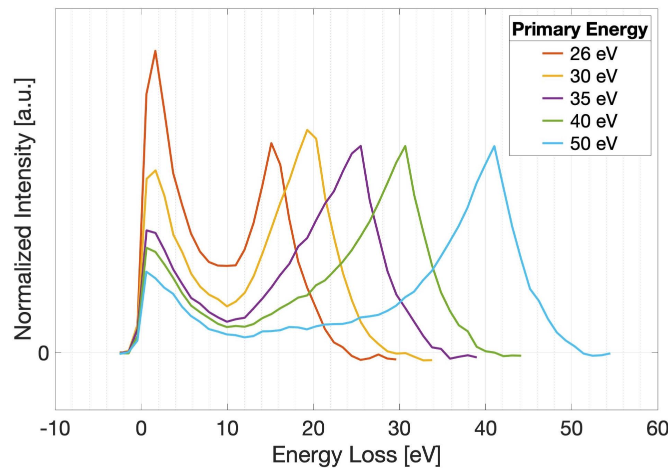


(b)

Figure 9.5: BSE and SE spectra of **Si-wafer** ($SiO_2$) from 16 eV to 50 eV. Spectra are normalized to their integral so the total signal is equal for all spectra.

not only material dependent, but also depends on surface topography (edge effect) and therefore these ratio comparisons need to be interpreted with caution. In my work, I will mostly focus on the BSE energy loss signal and not on the SE signal, however.

What is of more importance for this work is that with decreasing primary energy, the detected BSE signal increases, especially for low Z materials (see section 4.2.1). This enables measurements with sufficient signal intensity at relatively low electron dose (e.g. typical image dose for DNA origami on silicon-wafer is about 1000 electrons per nm$^2$). Figure 9.8 shows full measured spectra from SE to BSE peak for $SiO_2$ and $Au$ at 80 eV PE. Again it can be noted that the relative intensity of the BSE compared to SE is higher for $SiO_2$ with lower atom number Z. Importantly, the BSE and SE are clearly separated by a plateau of underground signal therefore we expect little signal mixing of SE and BSE.

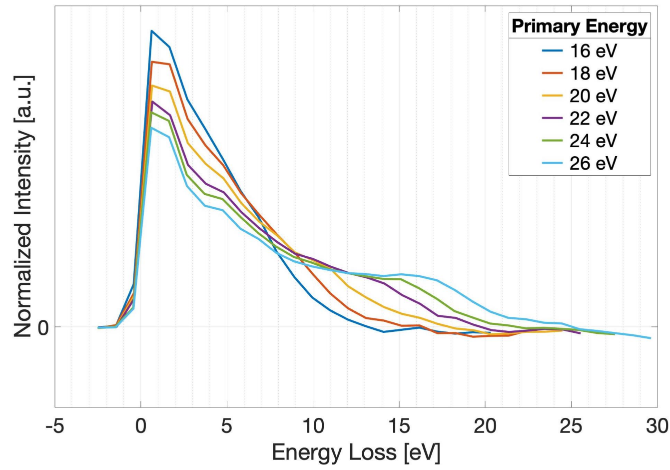


(a)

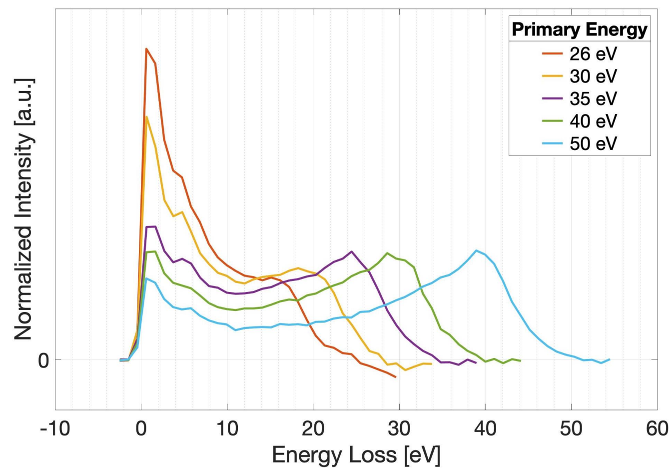


(b)

Figure 9.6: BSE and SE spectra of polycrystalline **gold** from 16 eV to 50 eV. Spectra are normalized to their integral so the total signal is equal for all spectra.

To summarize this short detour on secondary and backscattered signal mixing, it is apparent that the definition of secondary electrons as 'electrons with energy below 50 eV is inadequate when the primary energy itself is below 100 eV. The main signal of SE and BSE can be distinguished down below 30 eV PE, which also leads to different image contrasts when filtering for BSE or including SE as seen in section 8.2. Although portions of the signals are certainly mixed at primary energy below 50 eV. For this reason most spectra in this work are taken at 80 eV PE, since it gives sufficiently high signal to noise ratio for BSE and low beam damage (see section 8.3) with little to no contribution of the SE signal.

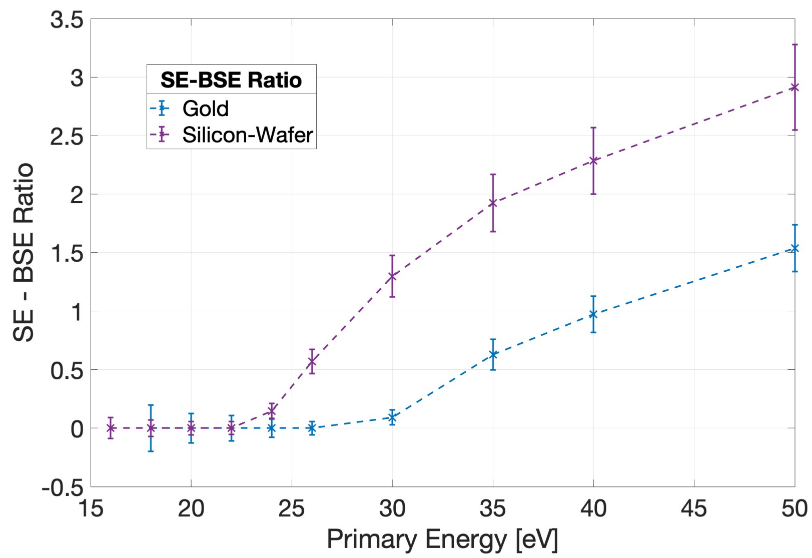


Figure 9.7: SE-BSE ratio plot for $SiO_2$ and $Au$.

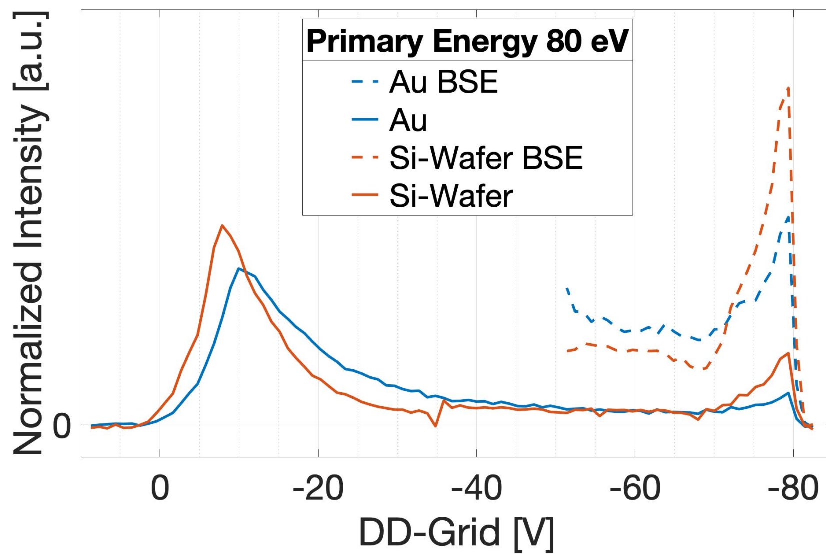


Figure 9.8: Example spectra of $SiO_2$ and $Au$. SE peak on the left, BSE on the right.

## 9.3 Backscattered EELS Spectra and the Energy Spread Function

Now that we understand more about the detection pathway towards the Delta Detector and have seen first data of secondary and backscattered spectra recorded with the Delta Detector, I want to explain in this section how we approach the evaluation of the measured backscattered electron energy loss spectra with the knowledge of the Energy Spread Function. Figure 9.9 is a graphical reminder of the origin of the ESF described in detail in section 9.1 (cf figure 9.3).

Every interaction signal – elastic or inelastic – is superimposed by the signature

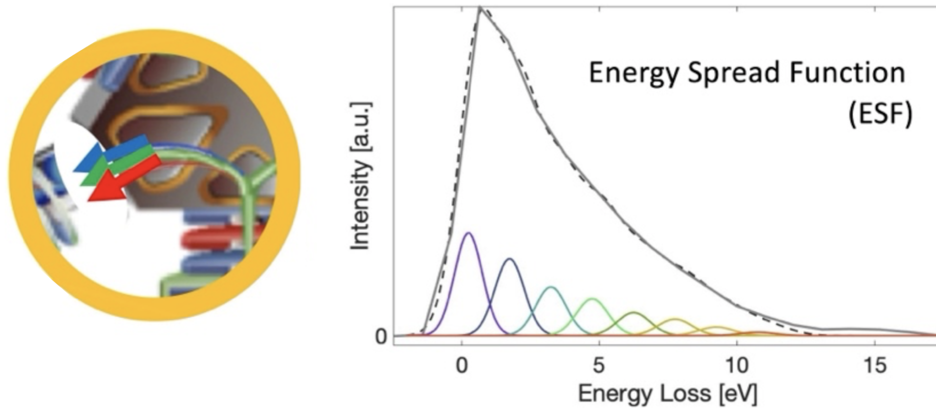


Figure 9.9: Measured Energy Spread Function (full black line) which is caused by the beam spread on the path towards the Delta Detector described in detail in section 9.1. Dashed line is the result of a convolution of the colored gauss functions in the plot; it is just meant to illustrate and remind that the ESF results from the superposition of many different spectral signatures from different beam paths through the delta detector.

of the ESF. Mathematically speaking, it is a convolution of the 'real' electron energy loss signal after the backscattering interaction with the sample surface with the ESF. To get the true signal out of our spectra a deconvolution is needed, which, however, is not straight forward since in every convolution information is lost. We are working in our group on approaches to the deconvolution problem with neural networks and bayesian inference frameworks, latter is however still in development. In my work I decided to try a forward modeling approach as a starting point, in order to study the relations between known or expected material signals and the measured bsEEL spectra with our device. This way we are able to evaluate how the measured signal is in agreement with the expected model and test the concept. For the forward model I use known data from other spectroscopic measurements of the same specimen – usually (S)TEM-EELS data. I model the known spectral features or peaks from the reference measurement and convolute the modeled data with the ESF. I illustrate the procedure with an example here.

Figure 9.10 shows measured bsEEL spectrum of a silicon wafer and a TEM EEL spectrum of $SiO_2$ used as reference spectrum to model the expected spectral signature. Since we expect to see the same spectral features (i.e. excitations) of the studied material in bsEELS as in TEM EELS, we use the energy of the spectral features as a set parameter and fit the intensity of the spectral features to our measured data.

The result of the convolution is shown in figure 9.11. The fit shows some systematic

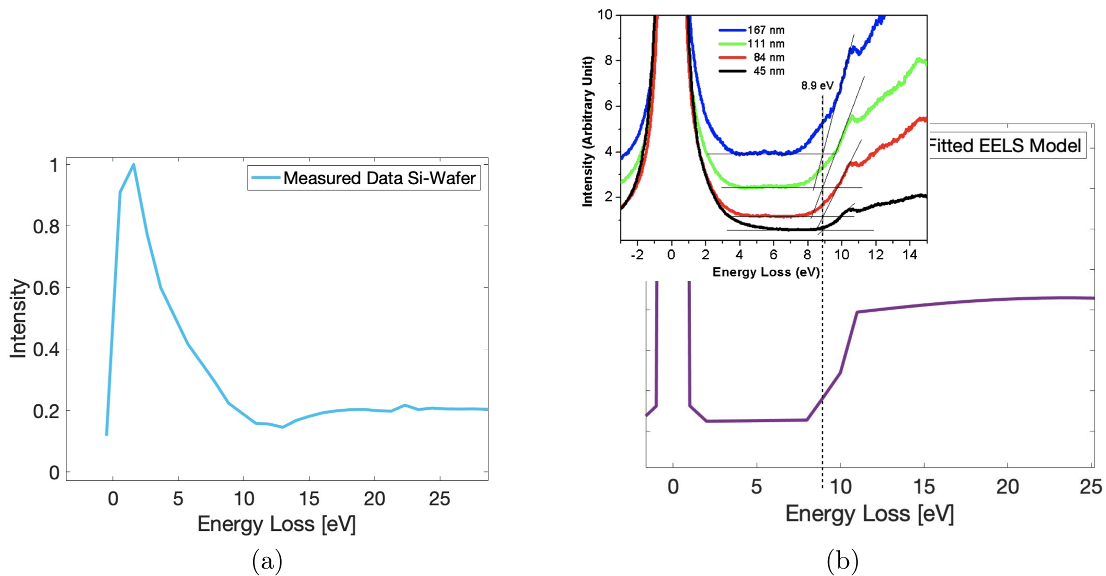


Figure 9.10: (a) Normalized Delta spectrum of a silicon wafer ($SiO_2$) at 80 eV PE. (b) Reference TEM EELS data used to model the spectral features (Park et al. [2009]). Onset energy of the bandgap signal (8.9 eV) is a fixed parameter, intensity of the plateau is a free parameter.

deviations from the measured data at the zero-loss peak and at the 10 eV energy loss dip, however, overall the fit represents the measured data very well using only the signal intensity of the step function as a free parameter (details for the convolution fit procedure are explained in 6.2.3). This is not a prove that the modeled data represent the 'true' energy loss spectrum of the backscattered electron interaction. Still the model fits the data well and as we will see with more samples in the part 'Experimental Results' we are able to model many different systems well with this approach, so we are confident that the convolution model fit is very reasonable as a first approach.

The silicon wafer is a useful substrate for bsEELS measurements since $SiO_2$ has a wide band gap and the EEL spectrum does not have any excitations before the band gap at about 9 eV. We see this in the measured data as the zero-loss peak has the same shape as the ESF up to the characteristic dip in the measured spectrum at about 11 eV to 12 eV energy loss. So when we put a material of interest on the Si

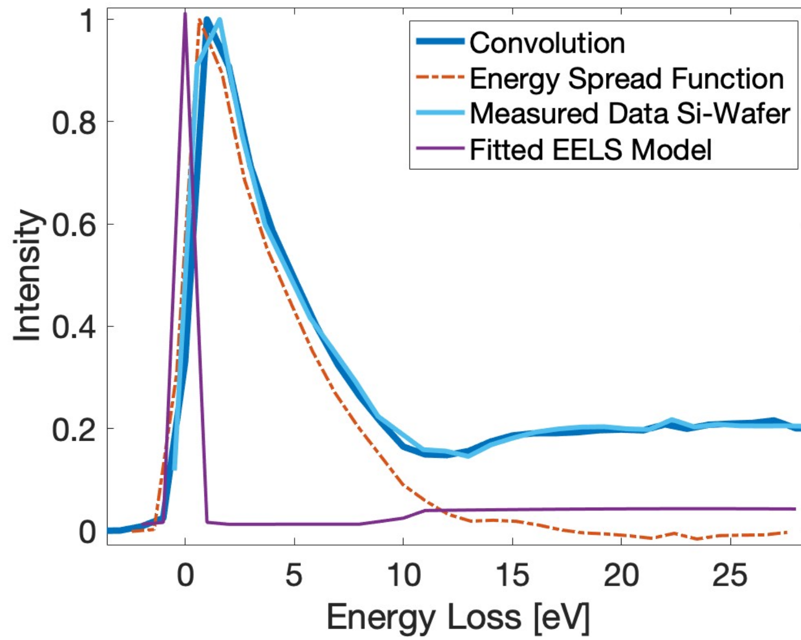


Figure 9.11: Measured Delta spectrum of a Si wafer and convolution fit of the modeled TEM EELS reference with the ESF.

wafer substrate, we can compare the measured spectra and immediately see if the material of interest has additional excitations in the 1 eV to 10 eV energy loss range. In addition, having the $SiO_2$ spectrum as a reference spectrum of the substrate enables us to check for sample contamination, since any additional hydrocarbon will give a signal in the band gap range. This is shown in figure 9.12. The bsEEL spectrum of a contaminated silicon wafer surface is wider than the ESF pointing to an additional signal before the band gap excitation. Unordered carbon has a relatively wide peak (compared to ordered structure of graphene for instance) at 5 eV (S. D. Berger and Martin [1988]) and including the expected peak in the convolution fit resembles the measured data well again.

To conclude, the forward modeling gives us a possibility to compare our measured data with expected signal known from other sources like (S)TEM EELS and enables us to understand our measured spectra and compare the fitted model intensities with the reference measurements. Using silicon wafer as a substrate gives us additionally the possibility to compare measured spectra with a internal reference and check for sample contamination.

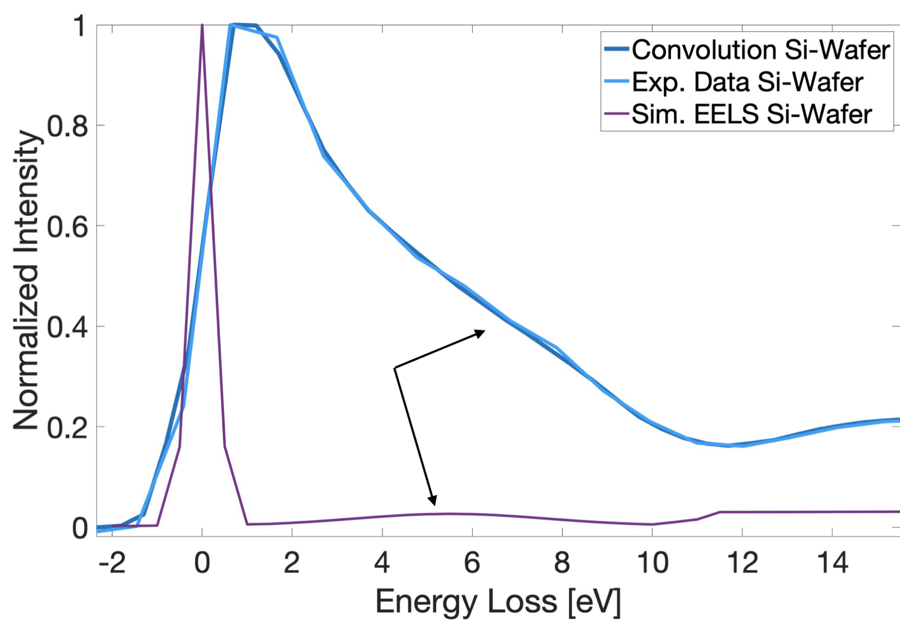


Figure 9.12: Measured Delta spectrum of a contaminated Si wafer surface and convolution fit of the modeled TEM EELS reference with the ESF. The hydrocarbon contamination gives an additional wide signal at 5 eV (black arrows).

# Part IV

# Experimental Results

In the following I will show the results of bsEELS experiments on a variety of materials and material systems. Since the data of this new characterization approach has a complicated signature dominated by an inconstant Energy Spread Function described in the previous part, it was inevitable to study a variety of materials in order to compare different signals with different expected outcomes. That way we gain understanding in how to interpret the bsEEL spectra at this stage and learn how to distinct real signal from signal artifacts. I divided the results in three chapters: Inorganic materials, which are stable under electron irradiation so we have not been limited by beam damage. Carbon materials, which have well understood properties and references we could compare our results with. And organic materials, where we expect bsEELS to have great potential, where, however, surface charging and beam damage plays a larger role as well.

# 10 Inorganic Samples

I want to start with experimental results of bsEELS on inorganic materials and samples, since we can largely exclude effects of sample degradation and beam damage on these systems. We have used clean silicon wafer and gold surface to screen the spectral response for BSE as well as SE, from which I have shown the most results already in chapter 9, most notably the bsEEL spectrum and interpretation of the silicon wafer.
Here in this chapter I want to show further bsEELS results on inorganic materials starting with the mentioned gold surface studies and on ZnS quantum dots embedded in a printed polymer structure, which will show the potentials in characterization and 3D reconstruction using bsEELS in a SEM.

## 10.1 Polycrystalline Gold

The gold surface was one of the first samples I measured in the Delta at the beginning of my doctoral studies. It actually was intended to be a mono-crystal surface which was provided by the group of Prof. Tegeder (PCI, Heidelberg University). Th gold surface is commonly used as a substrate for their HREELS studies. However, it was an older crystal and since we needed to transport the sample through ambient conditions and clean the surface, we were left with a polycrystalline surface. More details on sample and preparation can be found in section 6.1.1.
Since we did not understand the spectral response of the detector at that time, I used the gold sample primarily for screening of the spectral forms at different energies, which lead to the SE-BSE segmentation results discussed in section 9.2. With ongoing experiments, we understood better how to interpret the bsEEL spectra, which is why towards the end of my work I wanted to see if we can understand and interpret the older gold spectra as well. I recorded the bsEELS spectra as a single measurement at that time, so I could not average and the spectrum shows some characteristic noise.
As described in section 9.3 we use reference data from other experiments to perform a convolution fit with the ESF. The experimental bsEELS spectrum and the reference spectrum as well as the convolution fit are shown in figure 10.1. The fitted model represents the measured data well. The used parameter for the fit are listed in table 10.1. We use the peak energies and peak width (standard deviation of the gauss model) as fixed parameters taken from the reference experiment data. The only free parameters of the Gauss model used for the convolution fit are the peak intensities (amplitudes). The fitted values show some notable differences to the reference TEM EELS data: The third peak at 10 eV energy loss has a noticeably higher intensity in

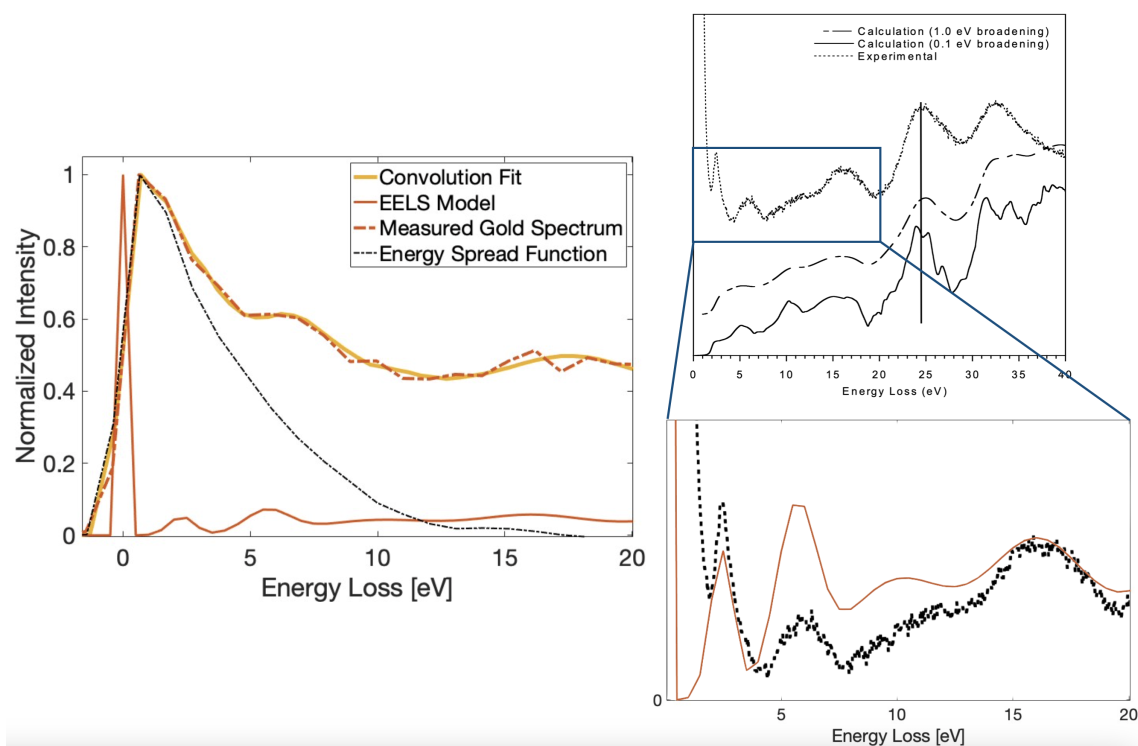


Figure 10.1: Measured bsEELS spectrum at 80 eV primary energy and reference TEM EELS experiment (Keast and Bosman [2006]) on the upper right. Bottom right: Zoom in of fit model and TEM EELS reference; peak positions are set from the reference data, peak intensities are fitted to the bsEELS measurement.

the bsEELS spectrum than in the TEM EELS experiment, which however fits the calculated low-loss EELS in the reference better. Moreover, the peak intensities in the TEM EELS reference generally increase with increasing energy loss, whereas for the bsEELS measurement, the first to peaks show the highest excitation intensity. The high intensity of the first surface plasmon peak in the TEM reference is due to broadening of the zero-loss peak, it has lower intensity in the calculated spectrum.

As I have shown in section 8.2 we could nicely resolve the single grains of the polycrystalline surface. To check whether the different image areas – i.e. grain surfaces and boundaries or 'gaps' between the grains – also have a different spectroscopic response, we segmented the brighter grain surfaces and darker interspaces between the grains by thresholding for higher and lower image gray values as is shown in figure 10.2, together with the resulting spectra from the selected regions of interest and the convolution fits with the corresponding fit models.

Again, the only free parameters changed for the new model fits were the amplitudes of the excitations. The resulting values are shown in table 10.2. All amplitudes of the inelastic scattered electrons increase relativ to the elastic peak for the darker interspace regions of the grains. However, it is notable that the first surface plas-

Table 10.1: Parameters for convolution fit in figure 10.1.

| | Mean | Sigma | Amplitude | Offset |
|---|---|---|---|---|
| **Gauss 1** | 2.45 | 0.5 | 0.053 | 0 |
| **Gauss 2** | 5.65 | 0.88 | 0.062 | 0 |
| Gauss 3 | 10.0 | 2.5 | 0.042 | 0 |
| Gauss 4 | 16.0 | 2.2 | 0.052 | 0 |

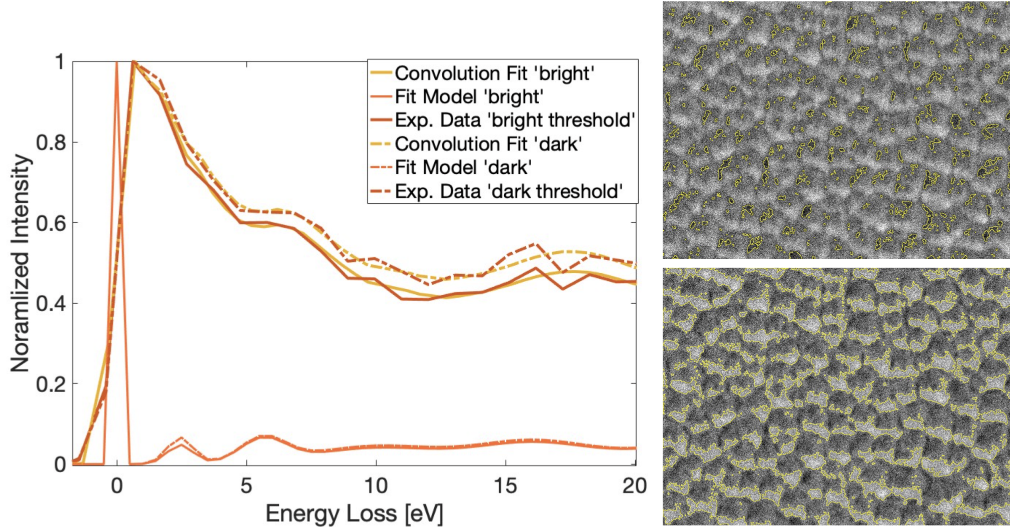


Figure 10.2: bsEELS spectra at 80 eV primary energy from bright (grain surface) and dark (grain gaps) image parts of polycrystalline gold surface. Right images show the evaluated image regions (top: dark; bottom: bright). Evaluation regions were selected by thresholding the 20 % lowest and highest gray values respectively.

mon peak at 2.45 eV energy loss is experiencing the highest amplitude change. The reason for this could be that the surface plasmon excitation is more likely between the grains at the boundaries. Still these results need to be interpreted with caution, since we know that the present topography also can influence the spectral response, changing the shape of the ESF and for this gold surface, we are not able to compare the spectra with an internal reference in the same image, which could help to interpret the spectral changes with more certainty.

This experiment shows that we are able to use the convolution approach to fit and interpret more complex energy loss spectra with several excitations in the low loss regime. Although the ESF has a FWHM of about 5 eV[1], also the excitation at 2.45 eV has an influence on the spectral form and is needed to fit the data correctly.

[1]See the shape and width of the ESF in figure 10.1, left panel

Table 10.2: Comparison of peak amplitudes of the convolution fits between the 'bright' grain surfaces and 'dark' interspaces from figure 10.2.

| | Amlitude 'dark' | Amplitude 'bright' | Ratio 'dark'/'bright' |
|---|---|---|---|
| **Gauss 1** | 0.066 | 0.048 | **1.38** |
| **Gauss 2** | 0.062 | 0.059 | 1.05 |
| Gauss 3 | 0.045 | 0.040 | 1.13 |
| Gauss 4 | 0.055 | 0.050 | 1.1 |

## 10.2 Qunatum Dot Fluorophores

Printing quantum dot fluorophores (Mayer et al. [2019]) was a research topic of Frederick Mayer (AG Martin Wegener, IAP, Karlsruhe Institute of Technology) with whom we were working on another project determining the porosity of printed materials at that time (Mayer et al. [2020]). We decided that having a look at the fluorescent 3d-printed samples might be interesting since we should be able to see the fluorescent excitation with bsEELS. One bigger obstacle, however, was to prepare the printed sample in a way we could study in the SEM. 3D-printed polymer structures have the problem that they are not conducting and charge a lot under electron irradiation. Metal coating is not an option if we want to do bsEELS experiments at ULV, since the signal of interest is then covered with the metal. Additionally of course, we want to study the inner structure of the sample as well and not only the surface of the 3d structure.
Irene Wacker and Ronald Curticean in our group are working with array tomography for many years (Wacker and Schröder [2013], Wacker et al. [2023]) and have adapted and improved the method towards 3d-printed samples in recent years. In a nutshell, we embed the structures in epoxide resin and cut the embedded structure into about 80 nm thick slices and place them onto a silicon wafer. The thin slices charge significantly less in the electron microscope and the slicing allows to look into the sample. More details on the sample preparation can be found in section 6.1.4.
The problem with this sample still was that it was a layered structure printed in several steps and the embedding and sectioning process lead to shearing and breaks of the structure layers. This made it first of all difficult to produce good sections and secondly difficult to find the regions of interest on the sections and correlate them to the 3d structure. Figure 10.3 shows the used section (top right). We can see that the structure is damaged by the sectioning process, since parts like the letter "E" are pulled apart. Nevertheless it allows a correlation to the corresponding structure layer and identification of the elements containing the blue CdSe/ZnS core–shell quantum dots (indicated by the blue circle in the figure).

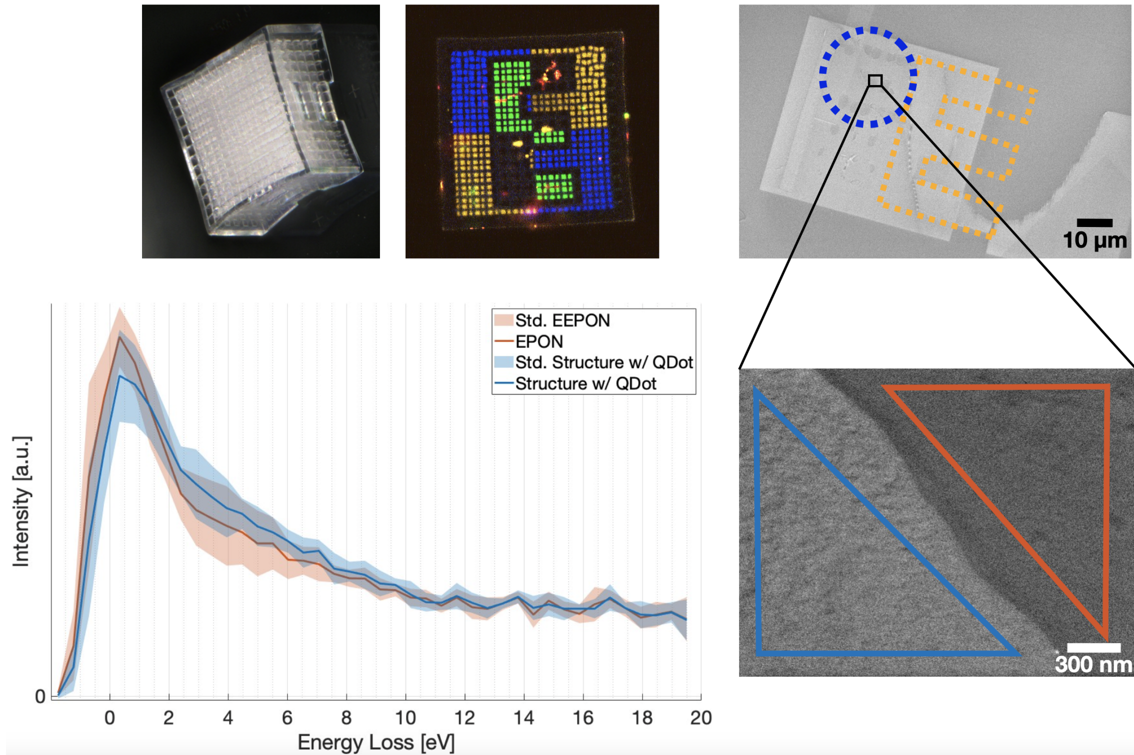


Figure 10.3: Overview on the bsEELS experiment on 3d-printed structure quantum dot fluorophores. On the top the 3d-printed structure is shown (left) containing different fluorescent image layers (see Ref Mayer), a confocal LM image of the correlated layer (middle) and an EM image of the section containing the structure. The letter "E" can be seen on the section which was used to correlate to the corresponding layer and identify the structures containing the blue quantum dots. On the bottom: Averaged bsEEL spectra from four different measurements of the structure containing the QDots and the surrounding epoxide resin (EPON) with the standard deviation of the measurements. One exemplary image of an evaluated region is shown next to the graph. The spectra were taken at 100 eV primary energy with a total spectrum dose of 57 000 electrons per $nm^2$.

The spectra of the printed structure and surrounding EPON clearly have a different form, where the QDot containing structure shows a higher energy loss from about 2 eV to 8 eV. However the standard deviation of the average of the four measurements is a lot higher than the spectral difference. If we look at the single measurements in figure 10.4 we see that the spectral form strongly differs from measurement to measurement. This is due to charging of the sample and more importantly inhomogeneous charging. Since the material distribution and ratio in the images is not the same and the two materials clearly charge differently, the surface potential distribution is different for every measurement leading to a differ-

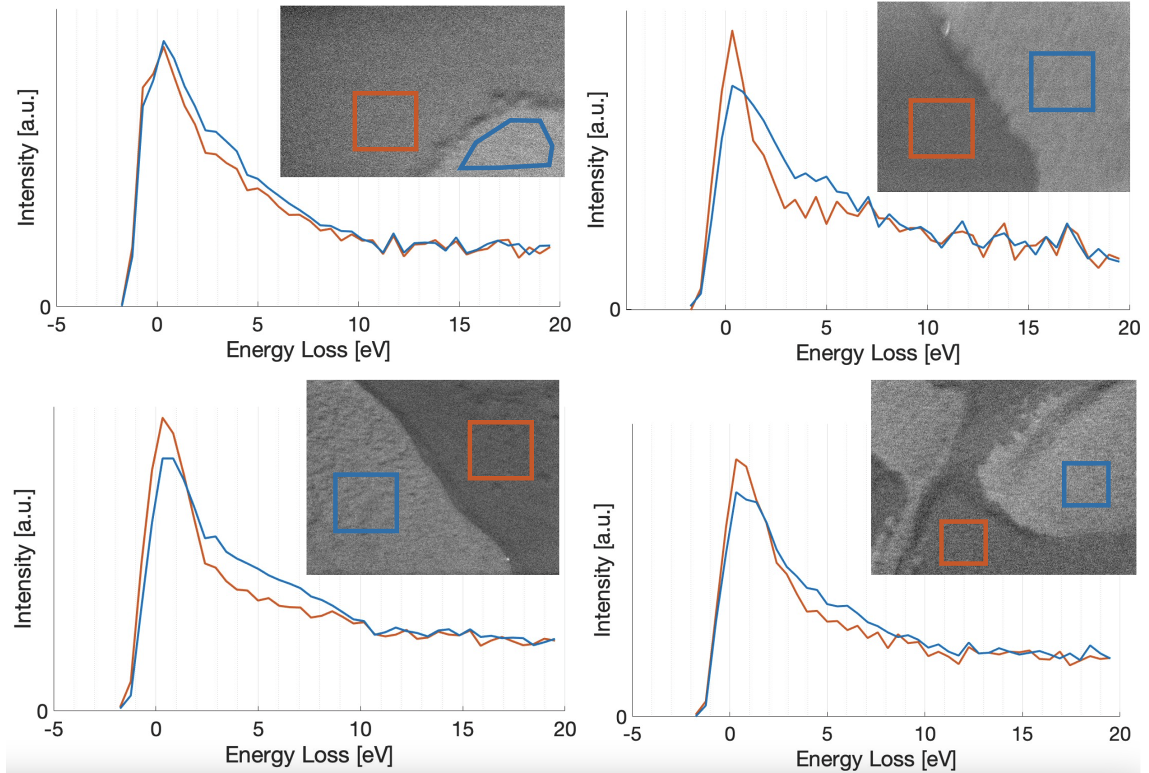


Figure 10.4: Single measurements with corresponding image evaluation regions used to calculate the averaged spectrum in figure 10.3.

ent response affected by a changing effective ESF. Despite of the different spectral response of the measurements, the difference in the signature between the epoxide resin and the Q-Dot containing structure is consistent in all measurements, implying that there must be a difference in the excitations of the two materials in the underlying bsEEL spectra.

If we integrate the signal intensity from 2 eV to 8 eV energy loss for both materials and calculate the average signal difference in that range, we get an intensity difference of 400(101) a.u. which corresponds to 16(4) % higher signal intensity for the structure containing quantum dots. This shows that the signal difference in that energy loss range is significant.

Although the ESF is not constant due to sample charging, I have tried to simulate the data on the assumption of the excitation of quantum dot absorption process. Figure 10.5 shows the result of the convolution fit. We can see that the spectrum of the epoxide resin is strongly influenced by the charging and has a completely different form compared to the ESF, which hinders the simulation with the convolution approach. The spectrum of the printed structure, however, has a spectral form corresponding to the general form of the ESF. This is in line with the fact, that the printed structure did charge less compared to the epoxide resin.

To my knowledge there are no low loss EELS studies for the CdSe/ZnS core–shell

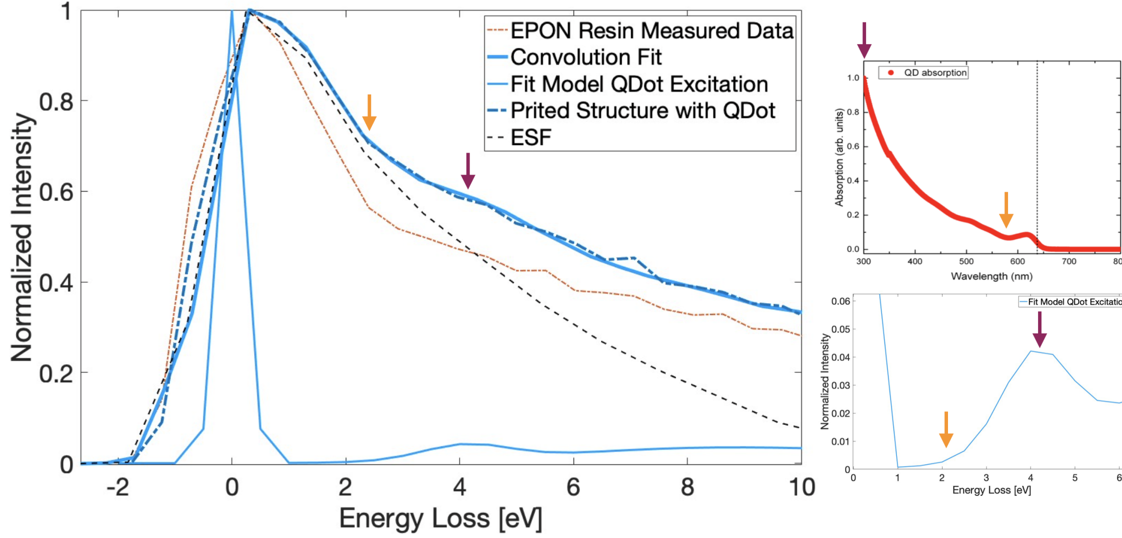


Figure 10.5: Convolution fit to the measured averaged spectrum in figure 10.3 assuming the excitation of the quantum dot absorption process. UV-Vis absorption spectrum used as fit reference is shown on the upper right (Elkabbash et al. [2019]), lower right shows the zoom in of the used gauss model.

quantum dots, so we used the light absorption spectra as a first approach and modeled the slope of the absorption curve with a gaussian peak with the mean at 300 nm. We have no reference at higher energy so a second gauss was added with doubled values for mean and sigma as the second order absorption to fit the data. For the evaluation I will focus on the first peak. Here we see that the onset of the peak and peak maximum resembles the onset of the kink in the measured spectrum and further course well, indicated by the arrows in the figure. It has to be noted that the zero-loss peak of the measurement is broader than expected from the typical ESF without charging, which I fitted by using a small width Gauss instead of a Delta peak for the zero-loss. The used parameters can be found in table 10.3.

Table 10.3: Parameters for convolution fit in figure 10.1.

| | Mean | Sigma | Amplitude | Offset |
|---|---|---|---|---|
| Gauss Zero-Loss | 0 | 0.22 | 1 | 0 |
| **Gauss 1** | 4.1 | 0.76 | 0.034 | 0 |
| Gauss 2 | 8.2 | 2.6 | 0.029 | 0 |

Although this experiment has shown some flaws due to charging artifacts, we are still able to measure a clear additional bsEEL signal from the structures containing the quantum dots which fit the absorption energy of the QDots well.

# 11 Carbon Materials

Carbon materials such as graphite, graphene, fullerenes and carbon nano tubes gained a lot of interest over the last years for a variety of applications, like biofilm engineering, catalysis support, conductive additives for electrode fabrications, electrochemical capacitors and many more (Titirici et al. [2015],Zhai et al. [2022],Chakrabarti et al. [2014]). Thus, the characterization of carbon materials after fabrication as well as in device structure is of great interest. Naturally a surface sensitive spectroscopic method with the possibility of high throughput and high resolution – as we want to establish with bsEELS – would complement and benefit the current research.
At this stage of method development, graphene was a very suitable material to test the bsEELS application towards carbon based and organic samples, since it is flat and conductive, thus should not introduce much errors to the energy spread function, and is well studied in the TEM EELS field, so reference spectra are easily accessible.
The results of bsEELS on graphene will be the main focus in this chapter. In the second section I want to show first results on different carbon structures from a pyrolysis experiment in a collaboration work within the cluster of excellence "3dmm2o".

## 11.1 Graphene

I started the first bsEELS experiments on graphene on TEM Grids mounted on a STEM sample carrier. It turned out that it was not possible to get reliable, reproducible results for several reasons: Firstly, the sample preparation under ambient condition from an exfoliated graphene suspension (see section 6.1.3) introduced a large amount of contamination. Secondly, under ULV electron irradiation the grids appeared to accumulate charge, also not homogeneously over the sample. Thirdly, the orientation of the grid surface was not constant in the STEM carrier. The last two points have large influence on the energy response of the detector system.
To exclude these errors we decided to move to a silicon wafer as a substrate for the graphene suspension. This did remove the charging problem and gave a constant surface topography, which allowed to compare measurements in a meaningful way. Additionally, this allowed us to clean the sample surface with low dosed argon plasma to remove surface contamination without damaging the graphene surface. Deborah Wrege performed the experiments on graphene on silicon wafer substrate as part of her master studies under my supervision in our group (Wrege [2022]).

Figure 11.1 shows bsEELS spectra of graphene and the silicon wafer support recorded at 100 eV primary energy. The spectra are clearly different and the characteristic dip of the $SiO_2$ spectrum at about 10 eV energy loss indicates that the

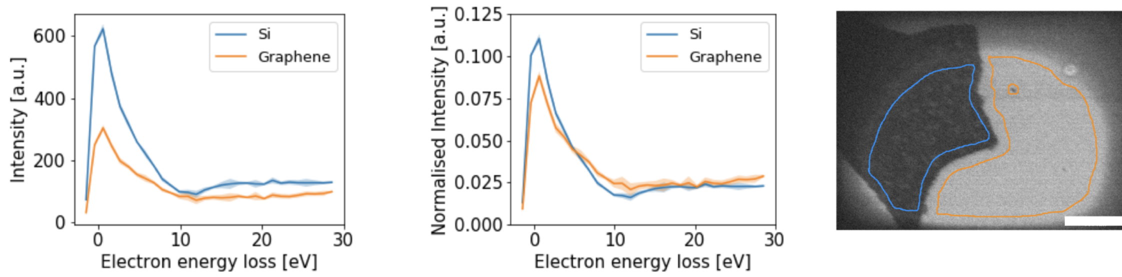


Figure 11.1: bsEELS spectra recorded with 100 eV primary energy from graphene and the silicon wafer support. The indicated errors are the standard deviation of five consecutive measurements on the same area. Left: raw data. Middle: Data normalized to the integrated signal. Right: Reference image with the evaluated regions of interest. (From Wrege [2022])

surface in the central image region does not contain much contamination (see 9.3). As shown in the chapter before, we are now able to use reference data from TEM EELS measurements of graphene to perform a convolution fit and see how well the reference model represents the measurement. The result is shown in figure 11.2.

The convolution fit represents the data very well. The zero-loss peak fits the form

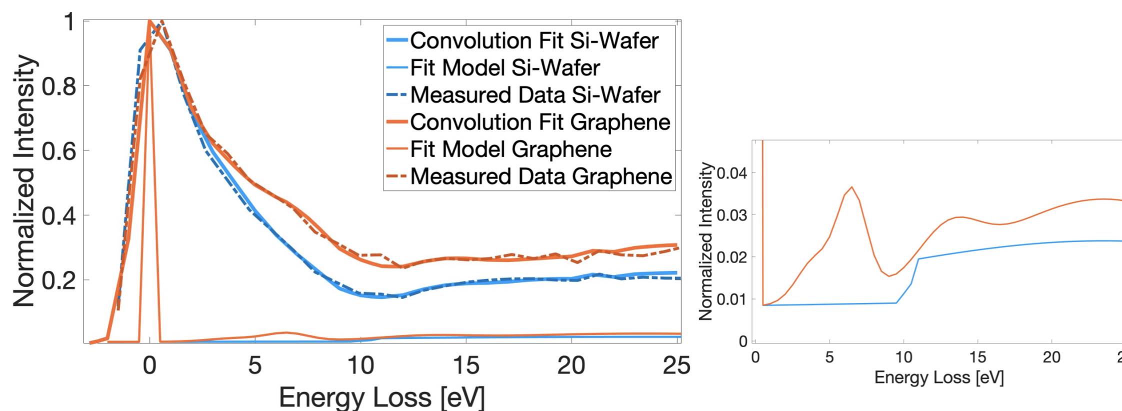


Figure 11.2: Model derived from TEM EELS (Wachsmuth et al. [2014]) and convolution fit to the bsEELS measurement in figure 11.1. The used parameters for the fit model of graphene are listed in table 11.1. Right panel shows a zoom in of the fit model.

of the ESF which indicates that the ESF resembles the imaging conditions for this measurements. Therefore a delta-peak is used for the fit and a small offset was added to fit the intensity offset of the silicon wafer spectrum. I needed to add a small contribution at 4.0 eV energy loss to fit the slope towards the 6.5 eV surface plasmon excitation of graphene seen in the TEM reference. As seen in the previous chapter, higher energy excitations have a lower cross-section for bsEELS at UVL,

Table 11.1: Parameters for convolution fit in figure 10.1.

| | Mean | Sigma | Amplitude | Offset |
|---|---|---|---|---|
| Gauss Zero Loss | 0 | 0 | 1 | 0.008 |
| Gauss 1 | 4.0 | 1.2 | 0.01 | 0 |
| **Gauss 2** | 6.5 | 1 | 0.025 | 0 |
| Gauss 3 | 13 | 2 | 0.01 | 0 |
| Gauss 4 | 23.5 | 8 | 0.026 | 0 |

so the volume plasmon peak at 23.5 eV has a relatively low amplitude compared to the TEM EELS results. The excitation at 13 eV does not correspond to the TEM EELS reference, it corresponds to second order excitation of the surface plasmon. This excitation needs to be considered with caution since there are no reference data to compare with. It is obvious that there is no second order scattering events on atomic layer graphene with 20 eV to 80 eV electrons in the TEM. However, for backscattering at 100 eV it makes sense that a second inelastic scattering event with the graphene layer might occur after backscattering at the support.

Another example of bsEEL spectra from graphene and silicon wafer support is shown in figure 11.3, this time with 80 eV primary energy. I want to include this example to illustrate the problems of the current setup. At first view the date look

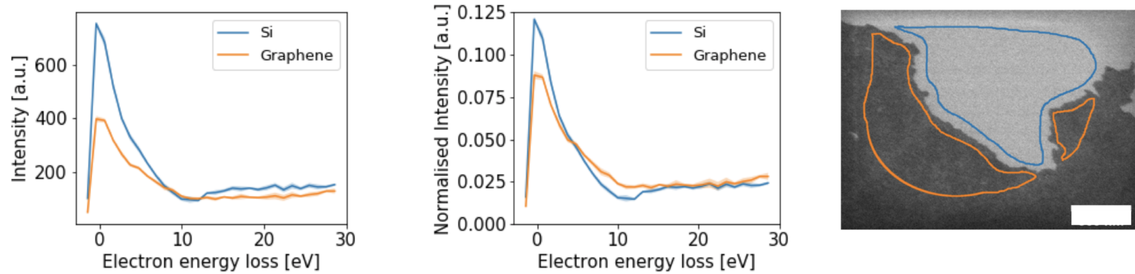


Figure 11.3: bsEELS spectra recorded with 80 eV primary energy from graphene and the silicon wafer support. The indicated errors are the standard deviation of five consecutive measurements on the same area. Left: raw data. Middle: Data normalized to the integrated signal. Right: Reference image with the evaluated regions of interest. (From Wrege [2022])

consistent with the previous example. But when comparing the data to the ESF for the convolution fit, differences between the measurements are apparent. This can be seen in figure 11.4. The expected EELS model for the silicon wafer does not fit the measured data, to fit the data an additional excitation is needed at 7.4 eV energy loss. This can have two explanations: Either, there is some residual contamination on the surface leading to the additional signal, as already discussed in section 9.3. Or, the ESF has a slightly different response at this measurement which leads to

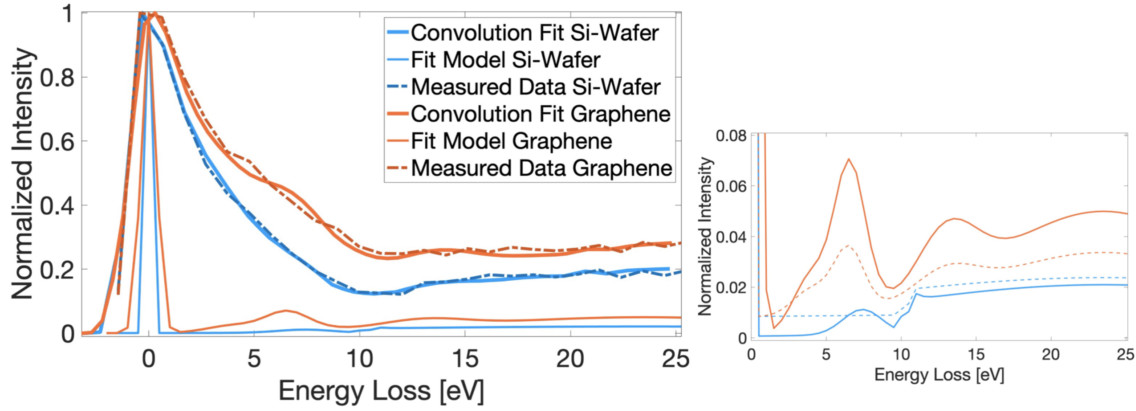


Figure 11.4: Model derived from TEM EELS (Wachsmuth et al. [2014]) and convolution fit to the bsEELS measurement in figure 11.3. The used parameters for the fit model of graphene are listed in table 11.2. Right image shows a zoom in of the fit model with the fit model of the 100 eV measurement (dashed) as reference.

a different from and the additional 'excitation' in the fit actually corresponds to a different ESF form. Either way, the same effect should influence the spectrum of graphene as well so the same additional excitation should contribute in the fit model for graphene. The fit parameter for graphene are listed in table 11.2. The first thing

Table 11.2: Parameters for convolution fit in figure 10.1.

| | Mean | Sigma | Amplitude | Offset |
|---|---|---|---|---|
| Gauss Zero Loss | 0 | 0.35 | 1 | 0 |
| Gauss 1 | 4.0 | 1.2 | 0.022 | 0 |
| Gauss 2 | 6.5 | 1.0 | 0.055 | 0 |
| **Gauss 'Add'** | 7.4 | 1.3 | 0.001 | 0 |
| Gauss 3 | 13 | 2.0 | 0.025 | 0 |
| Gauss 4 | 23.5 | 8.0 | 0.050 | 0 |

standing out is that the zero loss peak for graphene is significantly broader, which I took into account by increasing the width of the zero-loss peak for the fit. It is at this stage not possible to give a definite explanation. One could be that contamination in this measurement increases the surface roughness on the graphene flake which could lead to a broader zero-loss response of the ESF. This would mean that the contamination has a different dynamic under electron irradiation on the graphene surface than on $SiO_2$, but would then agree with the assumption that the additional peak is a real excitation from contaminants on the surface.
Important to note is that all other excitations expected from the TEM EELS reference of graphene are identical to the upper example at 100 eV. The amplitudes are higher to match the bigger signal contribution of the zero-loss peak, but the relative

amplitudes between peaks has not changed.
These two measurements lead to two important conclusions. First, we are able to measure and interpret bsEELS signal from graphene on silicon wafer substrate, identifying the characteristic 6.5 eV plasmon excitation of graphene, which is a great indicator for the applicability of bsEELS to atomic surfaces on bulk samples. But secondly, at this point the ESF shows a large variability, which, however, can be interpreted by using an internal reference of a well understood spectrum.

As written in the introduction to this chapter, we had more problems studying free standing graphene on TEM grids, mainly more contamination and a even less reproducible ESF, also because we did not have a internal reference with known spectra. Nevertheless we found some interesting and coherent results I want to show here as well.
Figure 11.5 shows images of bsEELS measurements of a graphene flake on gold TEM grids (see 6.1.3). The images in (a) show that a lot of contamination is present which shows itself in the rather blurred contrast. The contamination is clearly reduced with increasing electron irradiation time. It can be seen how the brighter contamination gets more and more reduced until string-like residuals are left in the graphene sheet. on the support the contamination seems to form larger clusters, also with smaller residuals in between. The dose of about 2.7 million electrons per $nm^2$ is very large, which also indicates the strong contamination. In the second and third image the growth of defects can be observed as well.
Since we expect to observe the surface plasmon excitation from graphene, we expect the bsEELS signal to have a higher contribution at 6.5 eV energy loss relative to the zero-loss from the image areas where there is graphene. I used the images of the spectral image stack to locate the signal by extracting the spectral parts we expect the plasmon contribution and subtracting this part from the spectral part of the zero-loss contribution. With our cumulative spectral image stack this means:
(Image@$-76.785$ V - Image@$-79.895$ V) - (Image@$-71.603$ V - Image@$-74.712$ V).[1]
This corresponds to subtracting the integral over the red shadowed area from the integral over the purple shadowed area in the spectrum in figure 11.5. The resulting image has less intensity, where the 'plasmon contribution' is higher and more intensity, where it is lower. For better contrast, I inverted the resulting images, so that now the brighter image areas have higher 'plasmon contribution'. These images are shown in figure 11.5 (b). The holes in the structure are of course white in the inverted image.

[1]The values of the grid voltage are measured precisely after setting the target voltage, which is done with less precision. For that reason the grid values have several 'odd' decimal places.

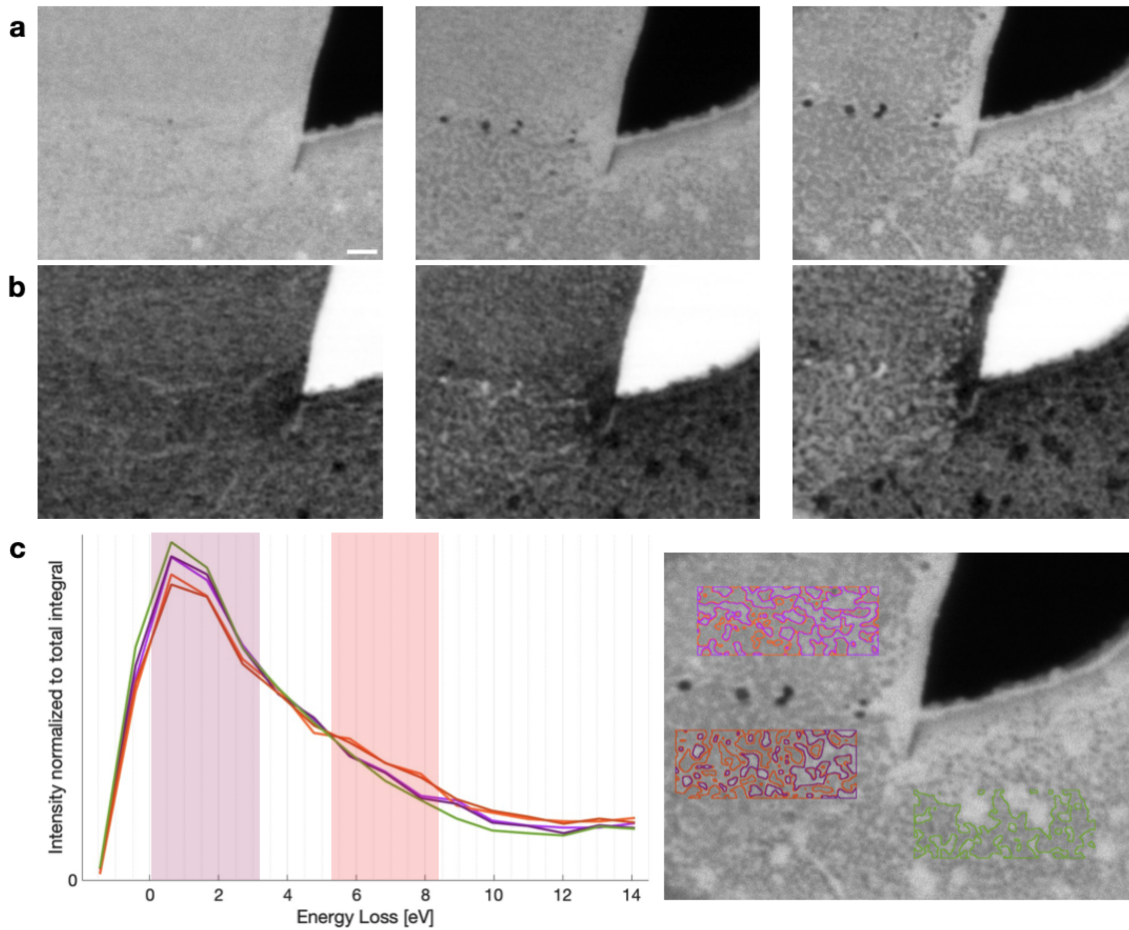


Figure 11.5: bsEELS on graphene on a gold TEM grid at 80 eV primary energy. (a) evolution of the imaged region with increasing electron dose. Between each shown image are are about 220 image scans with a total dose of 2.685 million electrons per $nm^2$. (b) calculated images out of the spectral image stack (see text). The bright image parts have a larger contribution of the red shadowed area (graphene plasmon) and the dark image parts a larger contribution of the purple shadowed area (zero-loss) in the spectrum in c. (c) bsEEL spectra normalized to the integrated signal from the regions of interest showed on the right with the corresponding colors.

In the first image shows no clear localization of higher intensities, which makes sense since the image is dominated by contamination, whereupon the freestanding graphene interestingly seems to have a slightly brighter 'plasmon contribution'. The texture of the free-standing graphene in the (a)-image is different from the graphene part over the support as well. The second and third image now clearly show that the bright 'plasmon signal' comes up where the contamination is removed, but only on the graphene flake. The support signal remains darker although the grey values in the (a)-images of graphene and support are almost identical. Also, the bright

structure in the ‘plasmon images’ matches the darker, clean areas in the raw images, which ist where we expect to have clean graphene signal.
We can use the calculated images to threshold for the brighter and darker signal and create regions of interest for the evaluation of the bsEEL spectra. These regions of interest and the corresponding spectra are shown in 11.5 (c). We see that the red-ish RIO contain the cleaned graphene areas, while the purple-ish RIO contain the contamination-residuals. It is not surprising that the red spectra show a lower signal at zero-loss and a higher signal at the energy loss we expect the plasmon signal, since we filtered the image for those signals. It is, however, consistent and confirmatory that the signal is located at the cleaned graphene areas. It is also very important to note that the green ROI containing the darker, cleaned signal on the support film does not show an additional plasmon signal, although it was selected by thresholding for brighter signal in the calculated image as well.
There is no substantial difference between graphene on support and the free standing graphene. We have to consider that the contamination is not only present on the upper but on the lower surface as well, so there is a thicker layer of contamination under the free standing graphene as well which means we are not measuring a pure monolayer of freestanding atoms here. This can explain that for both cases the spectra are similar.
Figure 11.6 shows the convolution fit for graphene and for the gold grid. To match the width of the zero-loss peak in the measurement a wider zero-loss gauss-peak for the fit model was fitted. The excitations for graphene are the same as on the silicon-wafer and so model fits the measured data well again. Since I had no other reference point, I used the polycrystalline gold model to fit the gold data as well. The model peak at 2.45 eV did not improve the fit, so I did not include it in the fit. The other excitations lead to a decent fit to the measured data.
The important point is that the surface plasmon excitation of graphene fits the measured signal well and that we can use bsEELS signal to locate expected excitations in SEM images.

Table 11.3: Parameters for convolution fit in figure 10.1.

| | Mean | Sigma | Amplitude | Offset |
|---|---|---|---|---|
| Graphene | | | | |
| Gauss Zero Loss | 0 | 0.65 | 1 | 0.01 |
| Gauss 1 | 4.0 | 1.2 | 0.022 | 0 |
| Gauss 2 | 6.5 | 1.0 | 0.055 | 0 |
| Gauss 3 | 13 | 2.0 | 0.26 | 0 |
| Gold TEM grid | | | | |
| Gauss Zero Loss | 0 | 0.65 | 1 | 0 |
| Gauss 1 | 5.65 | 0.88 | 0.01 | 0 |
| Gauss 2 | 10.0 | 2.5 | 0.035 | 0 |
| Gauss 3 | 16.0 | 2.2 | 0.06 | 0 |

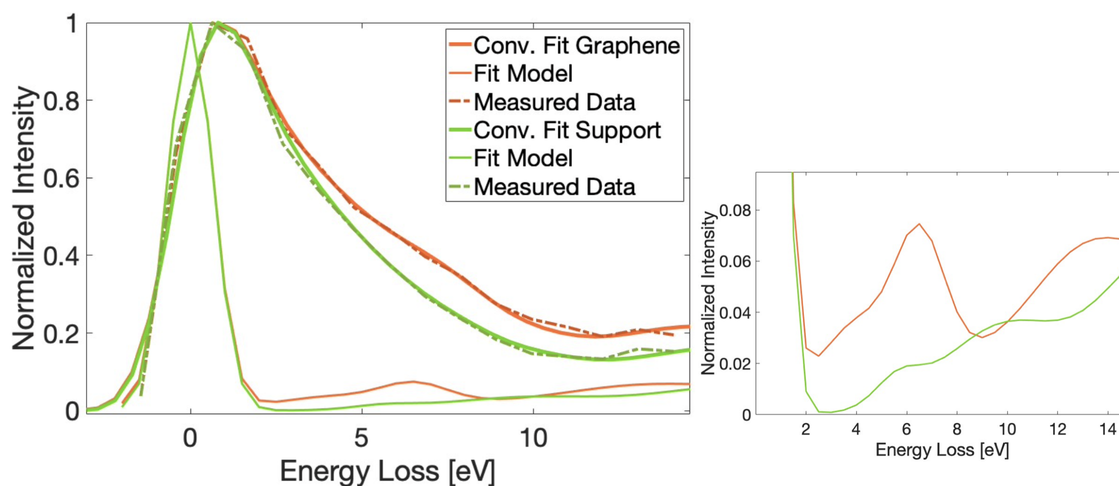


Figure 11.6: Model derived from TEM EELS reference and convolution fit to the bsEELS measurement of graphene and gold grid in figure 11.5. The used parameters for the fit model of graphene and gold are listed in table 11.3. Right image shows a zoom in of the fit model with the fit model.

## 11.2 Graphitized Cellulose Paper

Pyrolysis has a wide range of applications, mainly used in chemical industry to produce different gases and materials. Amongst them are many forms of carbon produced by pyrolysis (Wang et al. [2020b]). In recent years pyrolysis gained more and more interest in the field of 3D-printing as well, allowing to change the volume, density and also properties of 3d-printed structures after the printing process while keeping the printed shape (Arrington et al. [2021], Sun et al. [2023]). To study the pyrolysis process throughout the whole structure volumetric characterization with high resolution is imminent, bsEELS combined with array tomography could be a powerful approach to study this kind of samples in the future.
Results of a first proof of concept experiment are shown here. Graphitized paper structure were embedded in Spurr resin and cut into 80 nm thick sections placed on a silicon wafer. The cutting process damaged the graphitized structure which can be seen in the overview images in figure 11.7. Shear stress has tattered the graphitized structure. This however has made it possible to include the underlying silicon wafer in the measurements giving a reference signal to compare.
The graphitization process was not uniform throughout the structures, resulting in different forms of carbon in different regions of the sample. Figure 11.8 shows the two main products we found of the graphitization process, the right seeming rather amorphous while the left structure showing define edges and faces suggesting a more crystalline composition. Also, the silicon wafer is is apparently cleaner in the right case, whereas in the left case the contamination seems trapped between the carbon structures and is removed less effectively by the beam.

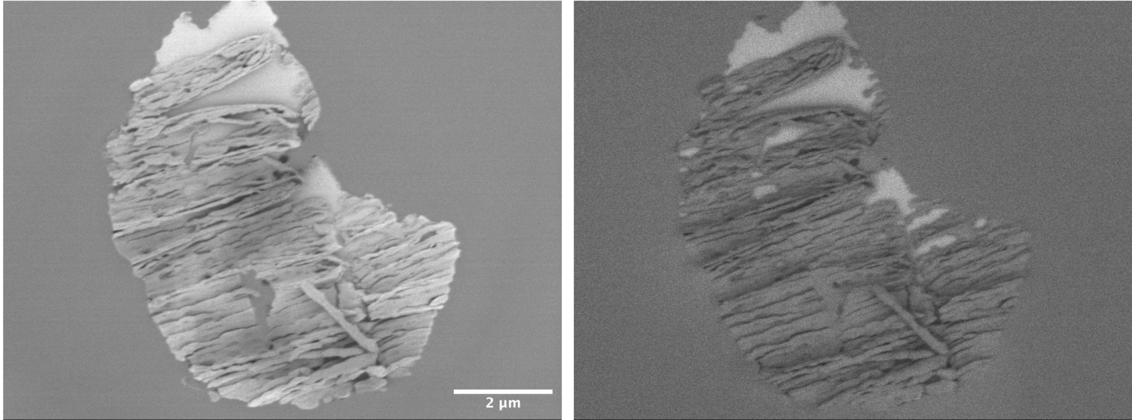


Figure 11.7: Overview images taken at 150 eV primary energy. Left: Including SE signal. The image shows artifacts due to charging. Right: BSE image (DD-grid voltage at −50 V filtering out the SE).

This also reflects in the bsEEL spectra of the silicon wafers of both cases. Both show wider BSE peeks than expected from clean $SiO_2$ as shown in section 9.3, implying that contamination is present. Still both show the characteristic dip at 10 eV indicating that the contamination layer does not superpose the underlying signal. We assume the additional signal on the silicon wafer ist present on the whole image, so on the carbon structure as well, so I include the additional peaks ('Gauss 'Add") of the silicon wafer fit to the fit of the carbon signal.
The carbon signals differ from one another, with the left, crystalline structure showing the excitation shoulder on the BSE peak at higher energy compared to the right, amorphous structure. Since we do not know what to expect without a reference for this experiment, I fitted the peak position of the carbon excitation together with the peak intensity. The fit parameters are shown in table 11.4. The fitted surface plasmon excitations have values of 6.5 eV for the crystalline structure and 5.6 eV for the amorphous structure. S. D. Berger and Martin [1988] have performed TEM EELS analysis on different carbon structures, finding the surface plasmon peak for graphitized carbon at 6.2 eV and for amorphous carbon at 4.8 eV.

It is an important result that we are able to measure a rather small (compared to the ESF width) energy shift from different forms of carbon. Although the values of the TEM reference do not match our bsEELS fit perfectly, the tendency of the amorphous structure having the lower surface plasmon excitation agrees with the TEM measurement. We need to keep in mind that we do not know for this sample, which form or also mix of forms is present at this measurements.

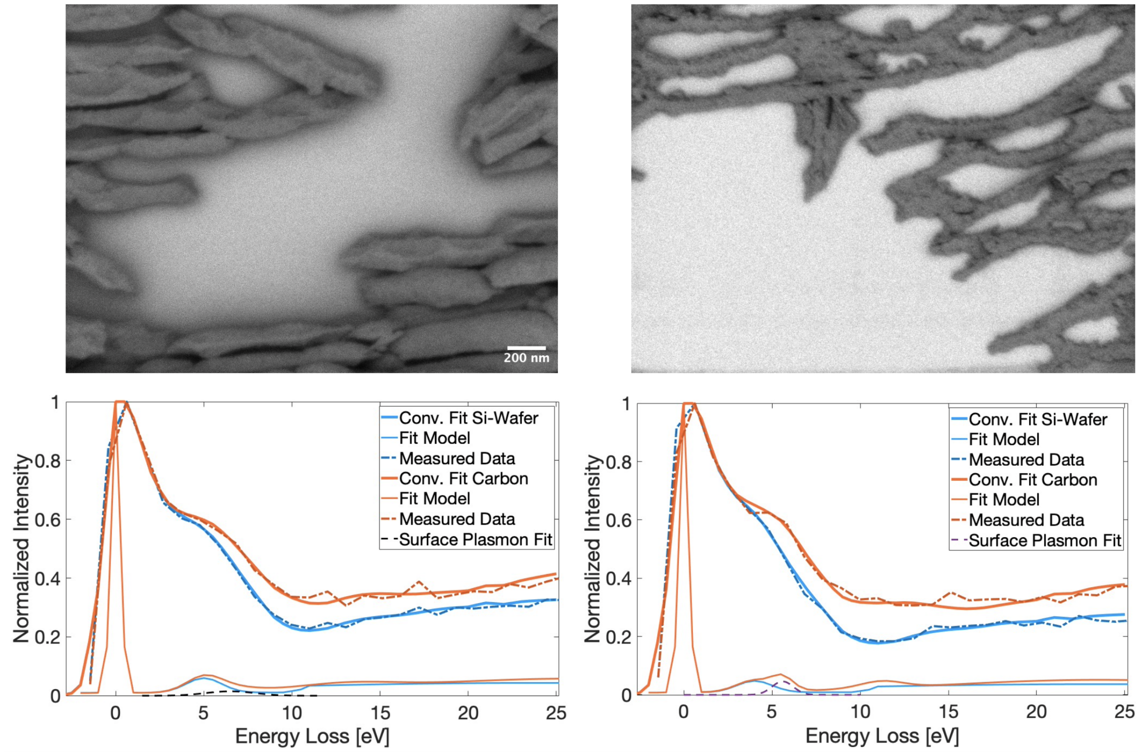


Figure 11.8: Images and bsEEL spectra from different products of the graphitization process with convolution fits to the carbon structure and underlying silicon wafer support. The two forms of carbon show different surface plasmon excitation in the fit.

Table 11.4: Parameters for convolution fit in figure 11.8.

| | Mean | Sigma | Amplitude | Offset |
|---|---|---|---|---|
| Crystalline Structure (left) | | | | |
| Gauss Zero Loss | 0 | 0.26 | 1 | 0.009 |
| Gauss 'Add' | 5.0 | 1.0 | 0.05 | 0 |
| **Gauss 1** | 6.5 | 1.4 | 0.015 | 0 |
| Gauss 2 | 13.0 | 2.8 | 0.02 | 0 |
| Gauss 3 | 26.0 | 9.0 | 0.05 | 0 |
| Amorphous Structure (right) | | | | |
| Gauss Zero Loss | 0 | 0.26 | 1 | 0.007 |
| Gauss 'Add' | 4.0 | 1.0 | 0.04 | 0 |
| **Gauss 1** | 5.6 | 0.6 | 0.046 | 0 |
| Gauss 2 | 11.2 | 1.2 | 0.024 | 0 |
| Gauss 3 | 23.6 | 9.0 | 0.045 | 0 |

# 12 Organic Samples

So far we have talked about bsEELS as a high-resolution spectroscopic method which is highly surface sensitive and allows to study bulk materials and devices without complex sample preparation. One other big advantage of the ultra-low electron energy is the reduced beam damage, which allows to study beam sensitive sample with significantly higher critical dose than TEM measurements for instance.
In this chapter I want to focus on organic samples with experiments that show the sensitivity of bsEELS in terms of signal detection and application on beam-sensitive materials. I will show that we are able to detect the signal of organic fluorophores attached to the Origami structure, which is the first step towards direkt correlation of EM and FM imaging with molecular resolution.

## 12.1 DNA and Fluorophores

DNA origami is a rather new topic of scientific and industrial studies. The ability to create arbitrary two- and three-dimensional shapes at nanoscale with the possibility to functionalize specific parts of the structure make them subject of interest for many biological and bio-engineering application like drug delivery for instance (Jahnke et al. [2023], Dey et al. [2021]). For us at this stage of the work it is a great sample to test bsEELS on a well-defined, nanoscale, organic material (see 6.1.2). Imaging results on the DNA origami are shown in section 8.2.2. Here I will focus on the spectroscopy results.

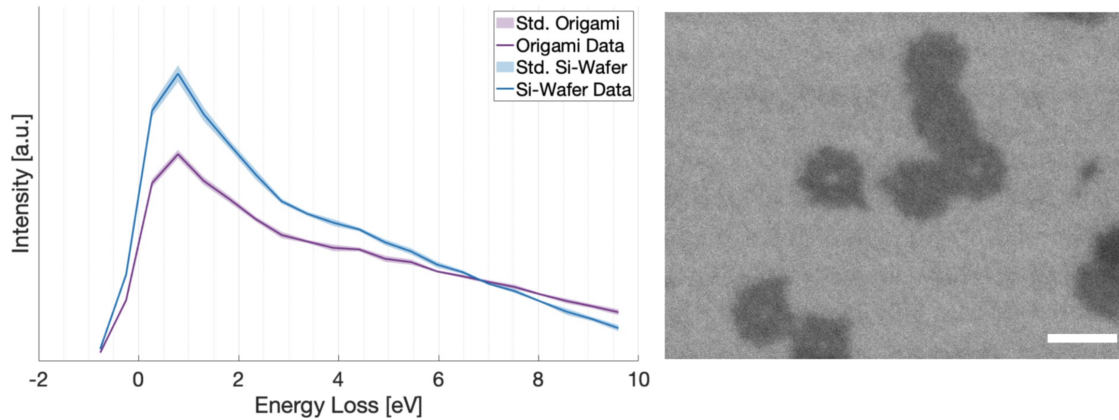


Figure 12.1: bsEEL spectra together with the standard deviation taken at 40 eV of DNA origami on silicon wafer averaged over five different measurements. Right: Exemplary image of one measurement (scale bar 100 nm).

Figure 12.1 shows measured data of origami on silicon wafer at 40 eV averaged over five different measurements together with the standard deviation. In each measurement five origami were selected for the spectral evaluation, so the total signal is the average of 25 origami. The rather small deviation shows that the imaging and sample properties were stable over the course of all five measurements. The silicon wafer spectrum (and also the Origami spectrum) shows a shoulder starting at 3 eV to 4 eV implying either additional signal from residual contaminants of the origami solution or a different energy response of the detector for this measurements or both.
The energy response is in any case different from our previously measured ESF, since the signal width of the measured data is smaller than the measured ESF. This is shown in figure A.1 in the appendix.
In order to fit the data nevertheless, I reduced the width of the measured ESF by interpolating the ESF over 100 datapoints per 1 eV energy step and removing every $n$'th data point to reduce the width. $n$ is then the 'Width Value' where – with decreasing $n$ – the width of the ESF is reduced. The MatLab code can be found in the Appendix (C.4). Figure 12.2 shows the resulting ESF with width value 5, which was used to fit the date in this case.
Figure 12.3 shows the convolution fits to the measured data of origami at 40 eV. Due to the increased number of datapoints the intensities of the excitations in the convolution model are reduced by the same factor, since every datapoint contributes to the resulting intensity in the convolution. I needed to add two excitations to fit the $SiO_2$ which – to point out again – could stem from contaminants out of the origami solution of could actually be coursed by a changed energy response in this experiment. In either case these 'signals' must contribute in the whole image, so in the origami spectrum as well.
DNA has an photon absorption peak at 4.7 eV (Sutherland and Griffin [1981]). How-

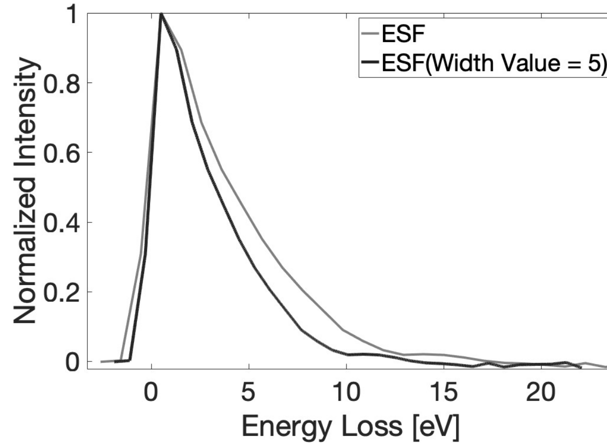


Figure 12.2: Measured ESF and ESF with reduced width to fit the data of origami on silicon wafer.

ever there are also electron interaction references for DNA: To study the influence of secondary electron damage on DNA, low energy electron experiments are published finding resonances energies for DNA damage at 0.8 eV, 2.2 eV, 5 eV and 10 eV, corresponding to single and double strand breakages in DNA. (Gao et al. [2021], Sanche [2008]). These energy transfer channels should be accessible by higher energy electrons as well. I used these energy values as reference data for the convolution fit, since to our knowledge there are no low loss EELS experiments on DNA published in the literature so far, only EELS experiments studying higher shell excitations on DNA (Londono-Calderon et al. [2019]).
The resulting fit parameter can be found in Table 12.1. The convolution model

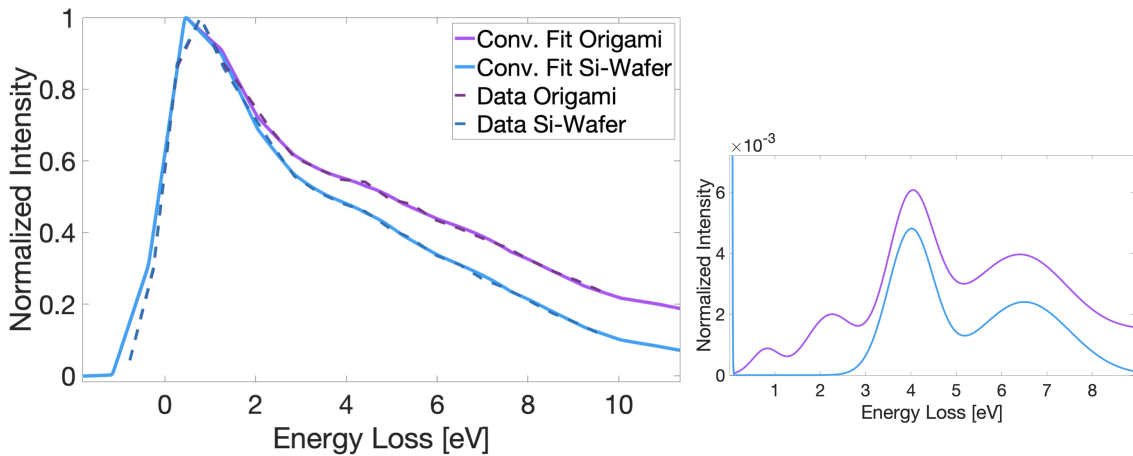


Figure 12.3: bsEEL spectra taken at 40 eV primary energy from origami and the silicon wafer substrate with convolution fits. Convolution models are shown to the right.

Table 12.1: Parameters for convolution fit in figure 12.3. ESF width was reduced with Width Value = 5

| | Mean | Sigma | Amplitude | Offset |
|---|---|---|---|---|
| Silicon Wafer ‘contamination’ | | | | |
| Gauss Zero Loss | 0 | 0.02 | 1 | 0 |
| Gauss ‘Add’ 1 | 4.0 | 0.5 | 0.0045 | 0 |
| Gauss ‘Add’ 2 | 6.5 | 1.0 | 0.0022 | 0 |
| DNA Peaks (additional to ‘contamination’) | | | | |
| Gauss 1 | 0.8 | 0.3 | 0.0018 | 0 |
| Gauss 2 | 2.2 | 0.5 | 0.0015 | 0 |
| Gauss 3 | 5.0 | 1.5 | 0.0015 | 0 |
| Gauss 4 | 10.0 | 3.0 | 0.0015 | 0 |

represents the data well. The deviations, most prominent around the zero-loss peak, are due to the low sampling of the measured data. From the difference of the origami curve to the silicon wafer reference it becomes apparent that all described damaging excitations are needed for the fit.

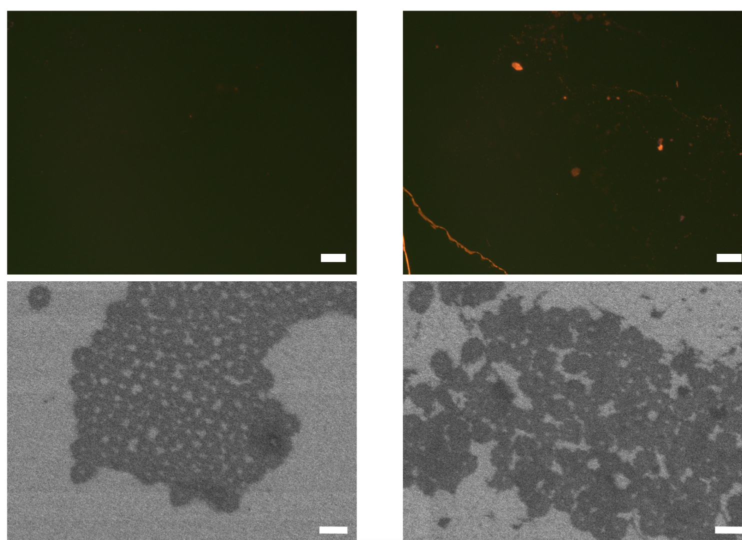

Figure 12.4: FM images (555 nm excitation wavelength, 3 s illumination time, scale bar 100 um) of DNA origami drop-cast on silicon wafer without (left) and with (right) Cy flourophores covalently bound. Below the FM images are exemplary SEM images of areas used for bsEELS analysis at 80 eV primary energy (scale bar 100 nm).

As pointed out in the introduction, DNA origami can be functionalized with different molecules. To test the sensitivity of bsEELS for organic molecules we obtained a batch of DNA origami with twelve Cy3 fluorophores covalently bound per Origami.

Figure 12.4 shows the fluorescence microscopy images of the drop-cast on silicon wafer of origami with attached fluorophore and the reference sample with no fluorophore to cross-check, whether the functionalization was successful. The Origami sample with attached Cy3 shows fluorescence while the reference sample shows no signal. The contrast of the BSE images of both samples is similar, indicating that both sample preparations are comparable in terms of contamination and signal.

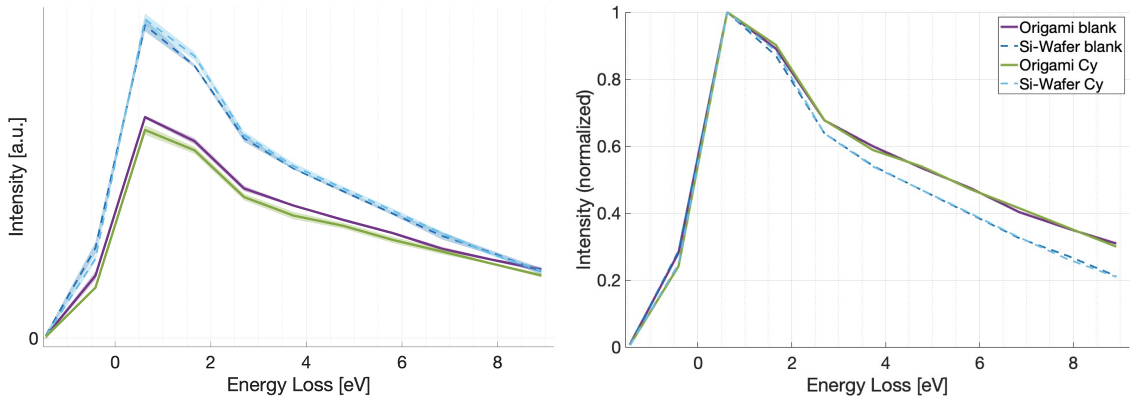


Figure 12.5: bsEELS on DNA origami with and without Cy3 fluorophores at 80 eV each averaged over five different measurements. Left: Raw spectra, right: normalized to the zero-loss peak.

Figure 12.5 shows the bsEEL spectra from the origami with Cy3 and the reference sample without, imaged with identical parameters. Looking at the raw spectra the Cy3 sample has a larger difference in intensity between the origami and the silicon wafer support compared to the unlabelled origamis. This is most probably because of slightly different state of contamination. the standard deviation between the five measurements is small indicating that the imaging conditions were stable. The normalized spectra show almost no difference between the two samples, so the influence of the Cy3 molecules is, if there is any, very small.

The convolution fits for both samples are shown in figure 12.6. Again, we do not expect any excitations for the silicon reference below 10 eV energy loss, so any additional signal we need to add for the fit of the $SiO_2$ are either due to residual contamination from the sample preparation or are deviations from the measured ESF and should in both cases be equally present on the whole sample, so are added as additional signal to the origami-fit as well. Both fits represent the data well, the used parameters are listed in table 12.2.

What stands out comparing the model fit between the two samples is the changed intensity of the excitations at 0.8 eV and 2.2 eV. When the Cy3 molecules are present, the excitation at 0.8 eV is higher and the peak at 2.2 eV is suppressed. With smaller ratio, the same is found for the 5.0 eV excitation which is higher and 10.0 eV excitation which is lower in the Cy3 case. The uncertainty for the fits is – by nature of the 1 eV sampling and convolution with the wide ESF – rather large.

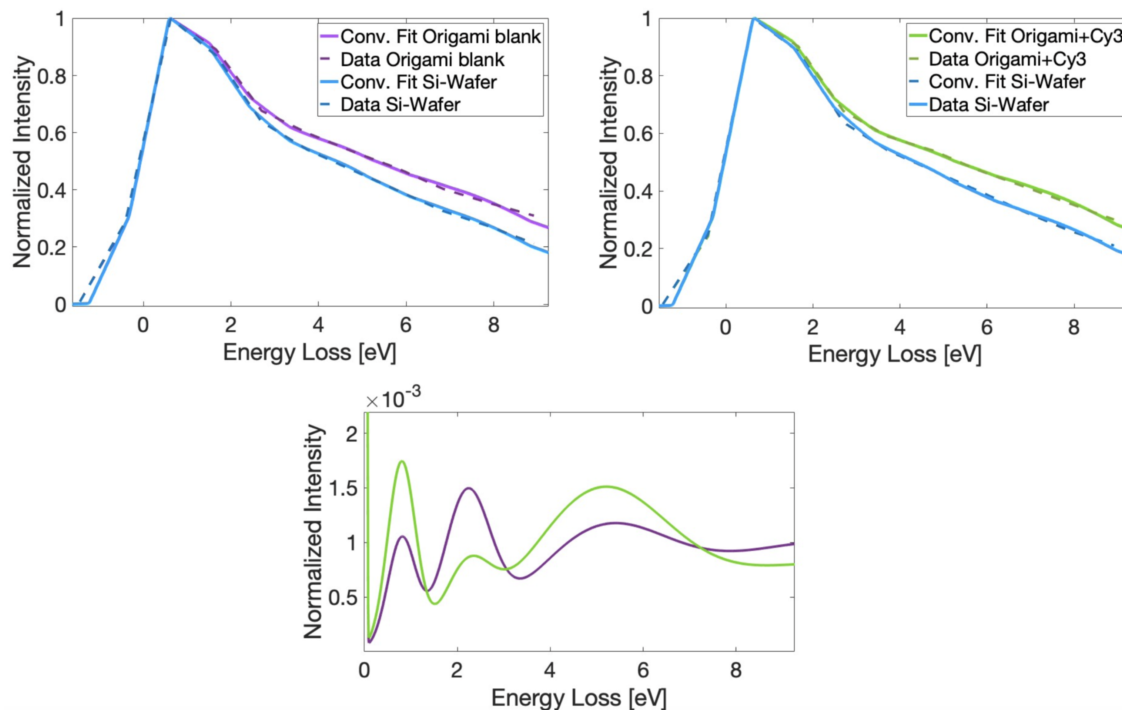


Figure 12.6: Model derived from LEE irradiation reference and convolution fits to the bsEELS measurements in figure 12.5. Left: Blank Origami. Right: Origami with Cy3. The used parameters for the fit model of Origami and silicon reference are listed in table 12.2. Lower image shows a zoom in of the fit model part of the Origami for both samples.

A variation below 50 % of one parameter has little significance on the fit quality. However, the differences between the two fits are between 50 % to 100 % which is a strong indication that these differences indeed stem from the presence/absence of fluorophores. I will discuss the uncertainty of these fits more in the summery chapter 13

The increased excitation at 0.8 eV could be caused by excitation of the trans-cis isomerization of the Cy3 molecules bound to the DNA (Spiriti et al. [2011]), witch is in the energy range of 0.5 eV to 1 eV. The suppressed 2.2 eV excitation could be a sign of Förster Resonance Energy Transfer (FRET) by the coupling of DNA with Cy3, which however so far has not been mentioned in literature to our knowledge.

Figure 12.7 shows the FM images of a second batch of Origami without (left) and with (right) Cy3 label. At this batch the functionalization of the DNA with the fluorophore clearly has worked with a lower conversion rate of the Cy3 binding. The FM images show little difference in the fluorescence signal. Again, the BSE images below the FM images show similar contrast confirming stable and comparable imaging conditions.

Figure 12.8 shows the convolution fits to the measured bsEEL spectra of the second batch at 80 eV. Spectral measurements of ten different regions were averaged in this

Table 12.2: Parameters for convolution fit in figure 12.6.

| | Mean | Sigma | Amplitude | Offset |
|---|---|---|---|---|
| Silicon Wafer ‘blank’ (ESF width reduced by width value 12) | | | | |
| Gauss Zero Loss | 0 | 0.02 | 1 | 0 |
| Gauss ‘Add’ 1 | 4.0 | 0.5 | 0.0030 | 0 |
| Gauss ‘Add’ 2 | 6.5 | 1.2 | 0.0020 | 0 |
| Origami ‘blank’ (additional to $SiO_2$ signal) | | | | |
| **Gauss 1** | 0.8 | 0.3 | 0.0010 | 0 |
| **Gauss 2** | 2.2 | 0.5 | 0.0013 | 0 |
| Gauss 3 | 5.0 | 1.5 | 0.0009 | 0 |
| Gauss 4 | 10.0 | 3.0 | 0.0010 | 0 |
| Silicon Wafer ‘Cy3’ (ESF width reduced by width value 14) | | | | |
| Gauss Zero Loss | 0 | 0.02 | 1 | 0 |
| Gauss ‘Add’ 1 | 4.0 | 0.5 | 0.0024 | 0 |
| Gauss ‘Add’ 2 | 6.5 | 1.2 | 0.0019 | 0 |
| Origami ‘Cy3’ (additional to $SiO_2$ signal) | | | | |
| **Gauss 1** | 0.8 | 0.3 | 0.0017 | 0 |
| **Gauss 2** | 2.2 | 0.5 | 0.0006 | 0 |
| Gauss 3 | 5.0 | 1.5 | 0.0013 | 0 |
| Gauss 4 | 10.0 | 3.0 | 0.0008 | 0 |

experiment with 12 to 13 origami per region included in the evaluation. So overall 125 origamis from 10 measurements were averaged in each spectra – with and without Cy3. In this case, the form of the zero-loss peak differs from the zero-loss form of the measured ESF, which makes the fit accuracy worse around the peak. The deviations are, however, consistent for the origami and the Si-wafer spectrum so the fitted signal should be consistently comparable and not be significantly influenced by the form of the ESF.
Looking at the fitted models, the same characteristics for the first two excitations can be seen as for the first batch. The 0.8 eV peak intensity is increased and 2.2 eV excitation decreased when Cy3 is bound compared to the reference. For this second batch the change of the excitations intensities is much lower which is consistent with the lower number of bound fluorophores as indicated by the FM images. The peaks at 5 eV and 10 eV have no significantly changed intensity between blank reference and with bound Cy3.

Figure 12.9 shows the results of a second experiment from the second batch at at 40 eV. Here, due to higher magnification, only five Origami per spectrum were selected and spectra of five different regions were averaged. The spectral form looks similar to the measurement of the second batch at 80 eV, and the fits show the same characteristics again, as the 0.8 eV excitation is enhanced and the 2.2 eV excitation reduced with bound Cy3, consistent to both measurements before. For this 40 eV

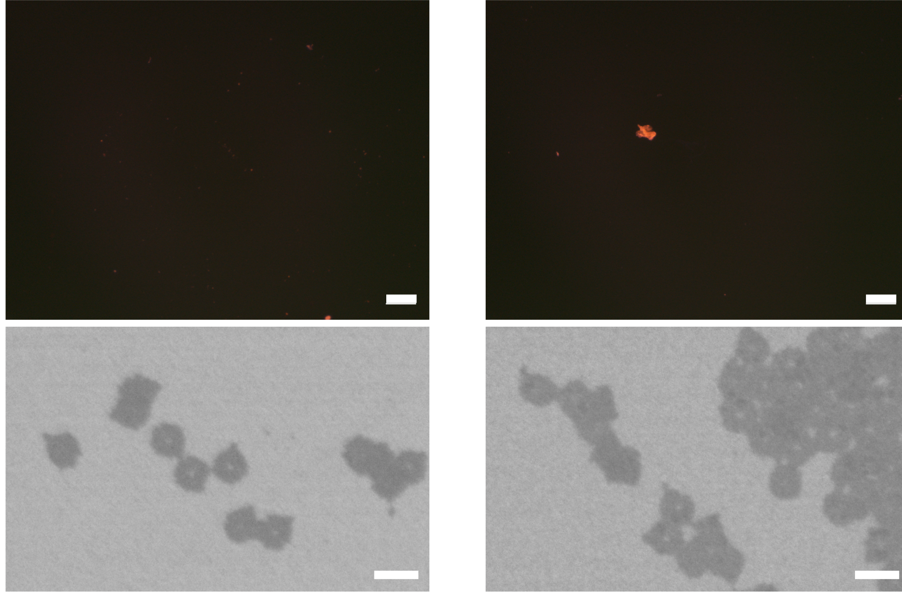

Figure 12.7: FM images (555 nm excitation wavelength, 3 s illumination time, scale bar 100 um) of a second batch of DNA origami drop-cast on silicon wafer without (left) and with (right) Cy flourophores covalently bound. Below the FM images are exemplary SEM images of areas used for bsEELS analysis at 80 eV primary energy (scale bar 100 nm).

measurement the 5.0 eV excitation is higher when Cy3 is present. And consistent with the fluorescence intensity, the overall changes of the excitations is smaller compared to the first batch as well.
The fit parameter of the 80 eV and 40 eV measurements from the second batch are listed in tables B.1 and B.2 respectively in the appendix.
Overall the intensity changes for the second batch are small compared to the rather high fit uncertainty of below 50 %, which again can be explained by the apparently smaller binding rate of the fluorescent label in the second batch. Still all changes point to a consistent influence of the bound Cy3 to the spectral signature. Raw spectra with measurement errors from the spectral evaluation are shown in the appendix in figures A.2 and A.3.

To sum up this section on bsEELS measurements on DNA and fluorophores: The fit model for DNA describes the measured bsEELS data consistently well over measurements on different samples and with different primary energy. It becomes apparent again that we need reference spectra from the silicon wafer support to interpret the data. Although the ESF shape is not constant for all measurements I have shown here, that the $SiO_2$ spectra are fitted well with the same additional excitations throughout all measurements, which is a strong sign that this additional signal is not artificial but originates from residuals from the buffer of the DNA solution.

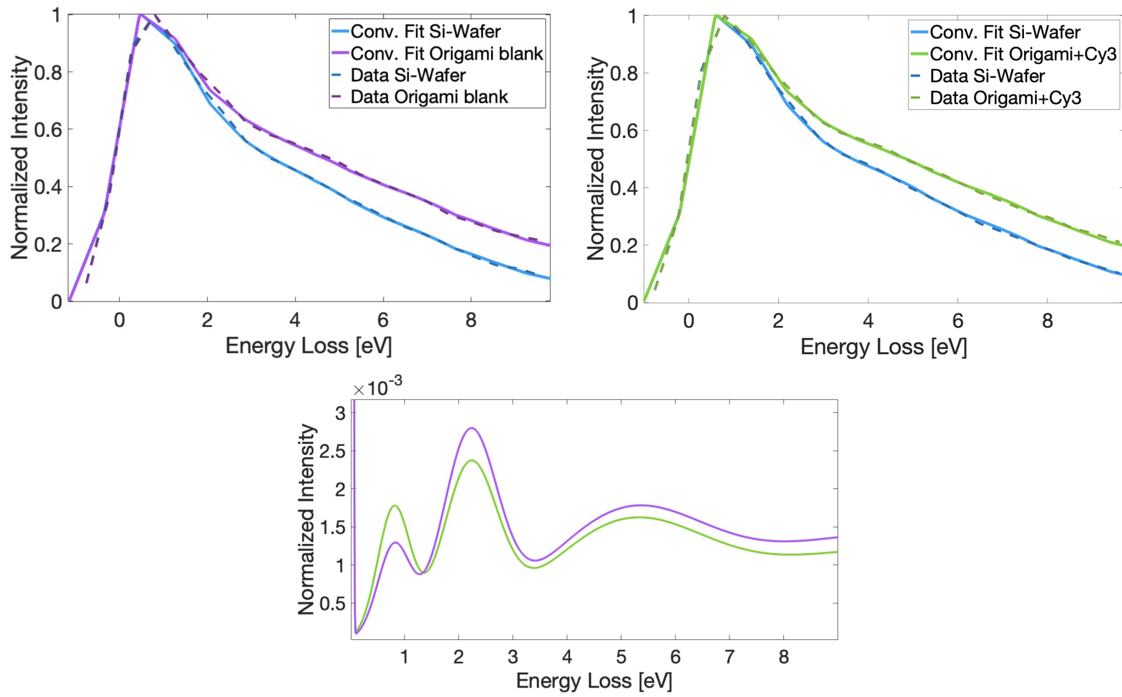


Figure 12.8: Model derived from LEE irradiation reference and convolution fits to the bsEELS measurements of the second batch at 80 eV primary energy. Left: Blank Origami. Right: Origami with Cy3. The used parameters for the fit model of Origami and silicon reference are listed in table B.1. Lower image shows the fit model part of the Origami for both samples.

The signal change of the excitations when the Cy3 fluorophores are bound to the DNA origami is consistent over the measurements as well. The higher 0.8 eV peak could originate from excitation of cis-trans isomerization of Cy3 bound to DNA, which would fit the energy. The reduced signal of the 2.2 eV excitations is rather surprising, since this energy would actually fit the absorption energy of the Cy3 fluorophore. If we want to speculate, the DNA resonance could be damped by a energy transfer process with the fluorophore and we actually measure a smaller absorption contribution of the fluorophores. But this definitely needs more study to understand this process.
Altogether, the data strongly suggests that we are able to detect the signal of at most 12 fluorophores bound per DNA origami with an electron microscope, which is a complete novelty in this field.

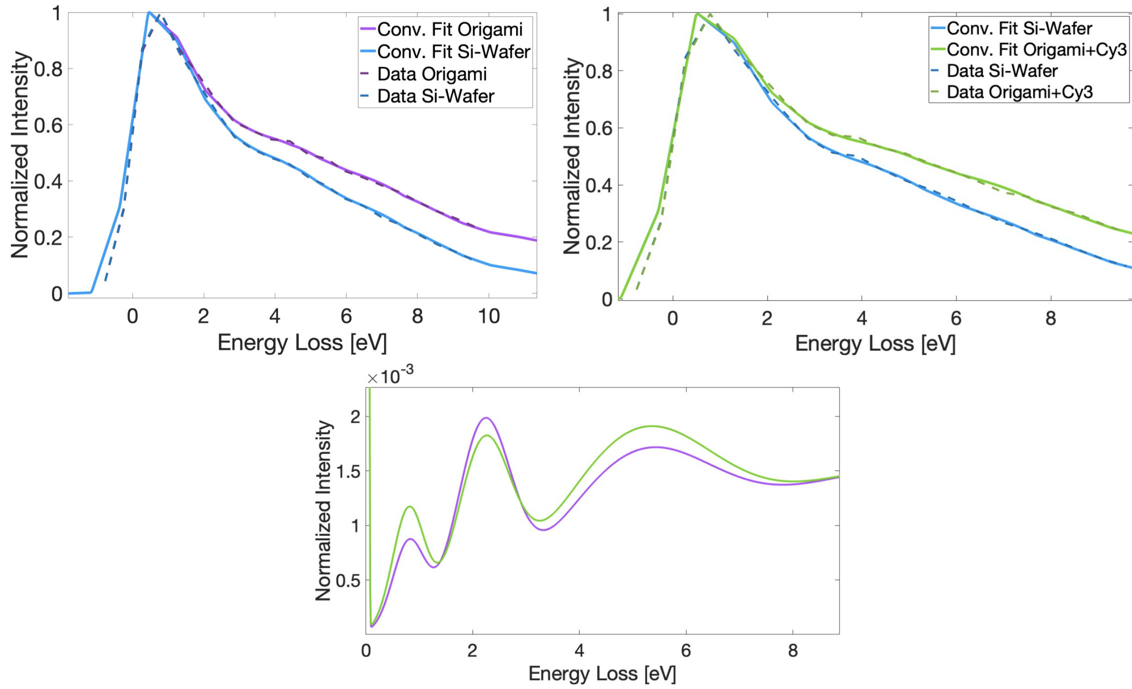


Figure 12.9: Model derived from LEE irradiation reference and convolution fits to the bsEELS measurements of the second batch at 40 eV primary energy. Left: Blank Origami. Right: Origami with Cy3. The used parameters for the fit model of Origami and silicon reference are listed in table B.2. Lower image shows the fit model part of the Origami for both samples.

## 12.2 Tetra-Phenyl Cumulenes [3]PH and [5]PH

Tetra-phenyl cumulenes were interesting as experimental reference since they have relatively 'simple' and 'tuneable' excitations. The work on these materials was performed by Giorgi King within his bachelor work in our group (King [2024]). Figure 12.10 shows the chemical structures, UV/Vis spectra and the measured bsEEL spectrum for [3]Ph. It is obvious that the overall form of the bsEEL spectra from [3]PH (and also [5]PH, see figure 12.11) is very similar to the $SiO_2$ spectrum. This indicates that the cumulenes indeed have only few excitations below 10 eV causing the small deviation from the silicon reference. Above 10 eV the signal of [3]PH increases so excitations are present there as well, however, for the fit and data analysis only the spectral information below 10 eV was included.
Within this experiment, a convolutional neural network (CNN) was set up by Giorgi King to perform the forward simulation fit of the UV/Vis reference data with the convolution of the ESF. The steps were the same as by the previously used 'brute force' fit by adjusting the free parameter by hand performed so far: First, the neural network fits the width of the ESF and width of the zero loss peak to fit the silicon wafer spectrum, where we not expect any excitations up to 10 eV. With the adjusted ESF width and zero-loss width, the features of the cumulenes expected from

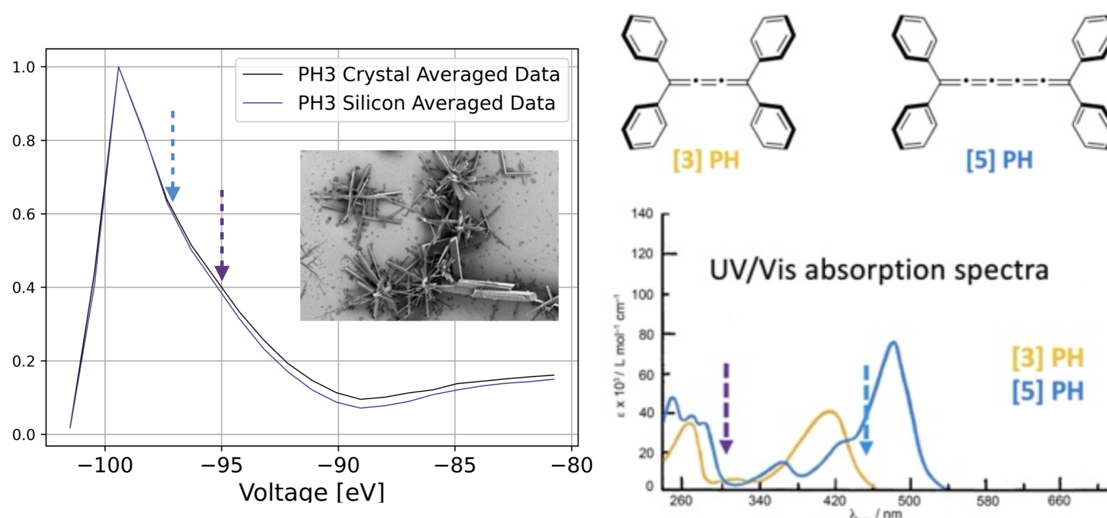


Figure 12.10: Overview on the bsEELS experiment on the tetra-phenyl cumulenes at 100 eV primary energy. Left: bsEEL spectra of [3]PH at 100 eV primary energy averaged over eight measurements. Inset BSE image shows the crystals on the silicon-wafer substrate. Right: Structures and UV/VIS spectra of both materials. Arrows indicate the onsets of the excitations which correspond to the onsets of the signal 'shoulders' in the bsEELS data. From King [2024]

the UV/Vis spectra were implemented in a simple gaussian model, there the excitation energies and width of the excitations were fixed and the only free parameter for the fit performed by the neural network were the amplitudes of the gaussian peaks. For detailed information to the performance and working principle of the neural network I refer to the bachelor thesis (King [2024]).
The fit results of the neural network are shown in figure 12.11. As mentioned above, the fit was restricted on the higher energy loss side by 8 eV energy loss since higher excitations are not known and not included in the model. The onset of the zero-loss peak had to be excluded for the fit as well, since otherwise the fit accuracy for the relevant features went down. This is due to the unknown difference of the measured ESF and the actual form of the ESF for this measurement. If the full zero-loss peak is included, the network tries to minimize the error of the peak form as well which leads to a worsened fit at the energy region of the excitations. Therefore the fit range is confined to the energy section shaded in red in the figure.
Although the fit range is confined and therefore the overall explanatory power is limited, the neural network ist able to converge to a stable output for a bsEEL spectrum with limited features. The fitted Gaussians show different intensities compared to the intensities of the UV/Vis absorption reference indicating that electrons have different cross-sections for these different excitations. This is in agreement to work we performed on organic polymers in the TEM (Kammerer et al. [2023]).

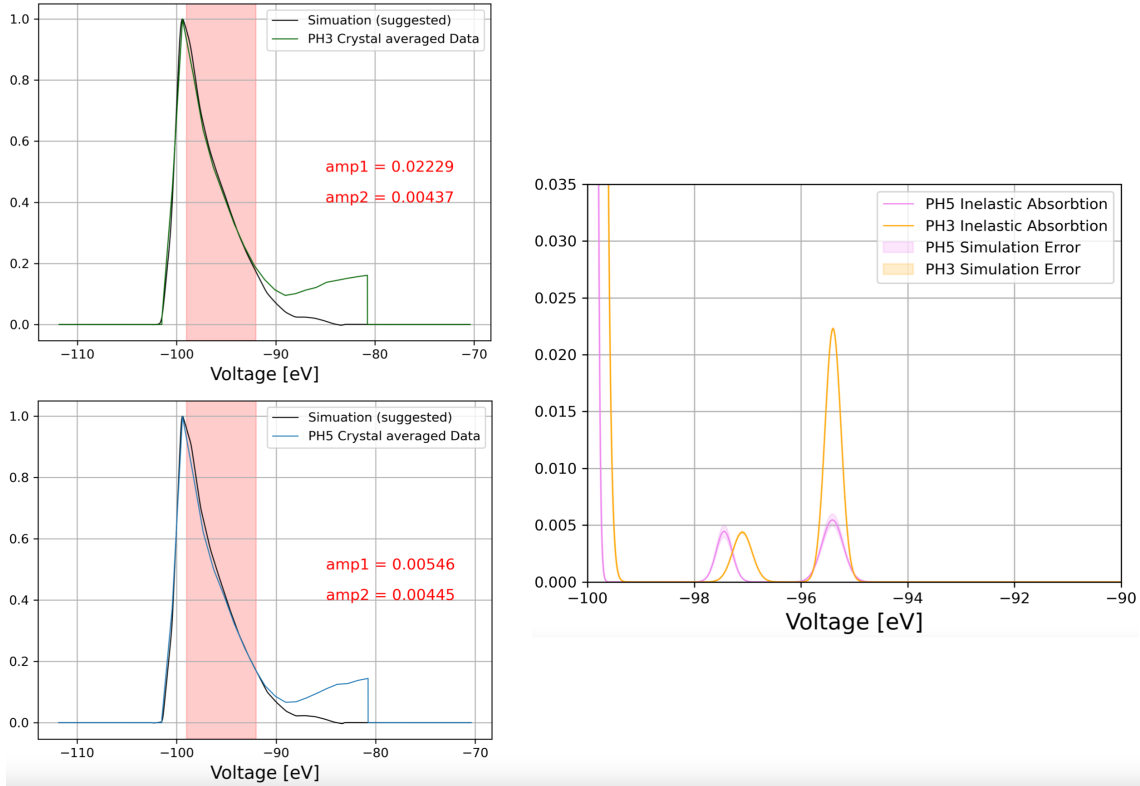


Figure 12.11: Result of the convolution fit performed by the neural network. Left: Measured data of [3]PH and [5]PH together with the fit curve. Red shading indicates the fit range for the neural network. Right: Plot of the resulting fit model for both materials. From King [2024]

To use this CNN approach to deconvolute our experimental spectra to high resolution EEL spectra, more information on the ESF is needed. In future the range of the neural network needs to be trained with more ground truth, i.e. data on different materials with known reference spectra. Still, this first experiment shows that a neural network can be successfully implemented in the simulation of a convoluted spectral system to retrieve high resolution informations on EEL spectra out of the convoluted data.

## 12.3 Polymere Microspheres

Microspheres have a wide range of applications from medicine to solar cells (Hossain et al. [2015], Kawaguchi [2000]), so the synthesis process and characterization of the products is of great importance to drive the field. Within our group we were performing TEM EELS analysis of synthesized polymeric microspheres, which could be functionalized after synthesis changing their chemical state and properties. Figure 12.12 shows an SEM image of the microspheres and the chemical structures of the polymerization and functionalization process.

The almost identical atomic composition of the eliminated and polyradical product of the functionalization implies that for a structural characterization different features than atomic contrast are needed. Within the TEM studies we could make use of differences in the electronic structures of the products, which lead to characteristic signals in the low loss electron energy spectrum. These signals were used for a high resolution characterization of the microspheres.

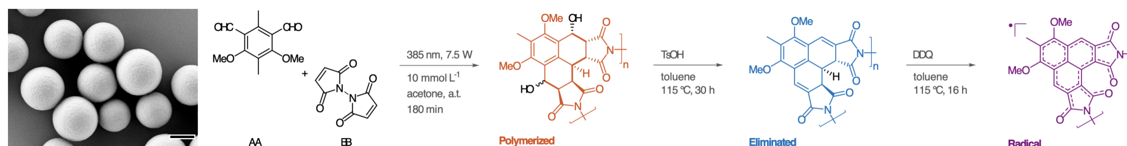


Figure 12.12: SEM image of the microspheres (scale bar 1 um) and the chemical structures of the polymerization and functionalization process (Kammerer et al. [2023]). Note that the Eliminated and Radical product vary in only one H Atom.

bsEELS can add value to the analysis of this kind for reasons, described in the motivation to this work (chapter 2), such as accessibility of bulk materials and signal confinement to a smaller volume. In this section I first want to show the bsEELS results on this material system in direct comparison to the TEM results and secondly, I want to show results of SE studies on this system with which we are able to add insights to the material properties as well.

### 12.3.1 bsEELS

The microspheres are embedded in EPON resin and cut into approximately 80 nm thick sections put on a silicon wafer. No silicon reference can therefore be used for the spectrum fit. Figure 12.13. shows the bsEEL spectra of the polyradical and eliminated spheres embedded in EPON. The image shows blurred edges of the spheres and shadows in between them indicating that the sample charges in-homogeneously. Also, different conductivity and charging is the reason we can see any contrast for the different materials at all. Dynamic charging and discharge of the sample could also explain the higher noise of the bsEEL spectra.

The overall signal intensity differs strongly between both types of the microspheres, the spectral form however shows only subtle differences. Figure 12.14 shows the

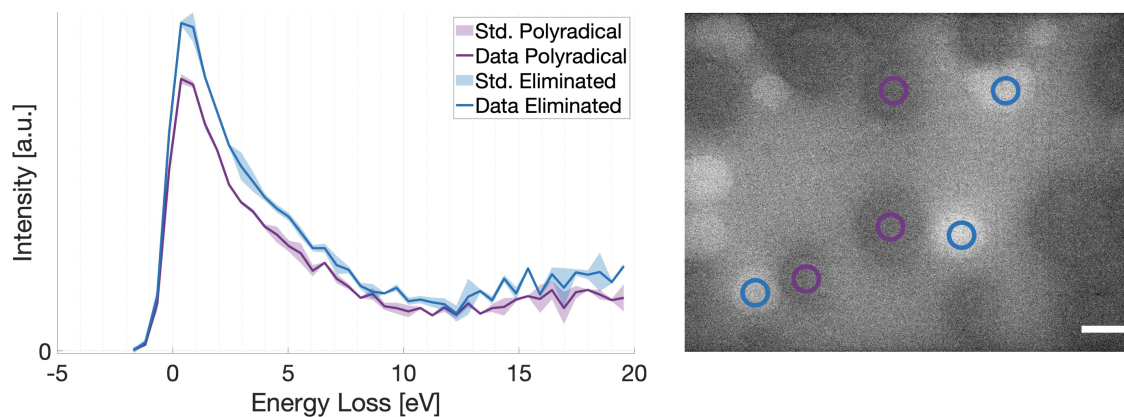


Figure 12.13: bsEEL spectra of the polyradical and eliminated microspheres averaged over two measurements from different areas. The spectra were taken at 80 eV primary energy. Right: BSE image of one image region with the selected spheres for the evaluation. Scale bar 1 um.

convolution fit for both materials. For these materials we do have a TEM EELS

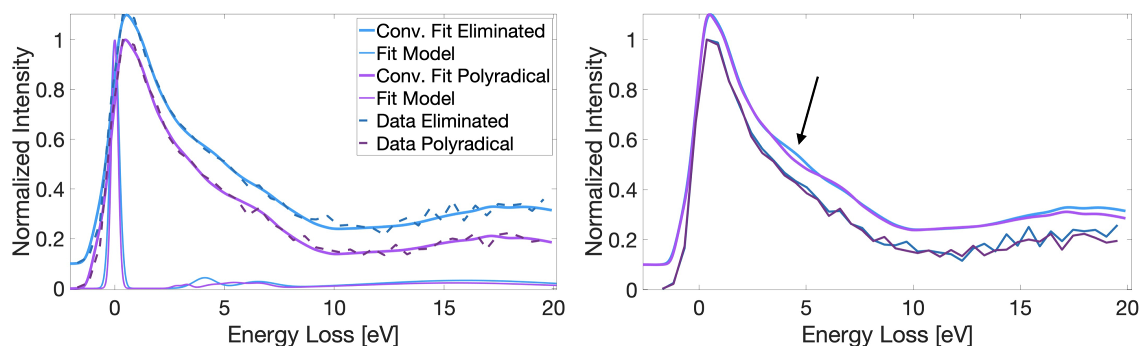


Figure 12.14: bsEEL spectra of the polyradical and eliminated microspheres together with the convolution fits for both materials. The same data is shown in two plot to compare the fit accuracy (left) and the signal differences (right). The arrow points to the main spectral difference between the materials.

reference at 60 keV from the exact same sample batch, which we used for the excitation energies in the fit model. The fitted model together with the direkt TEM reference is shown in figure 12.15.

Looking at the fits in figure 12.14, both fits represent the data well. Of course the data shows some noise especially towards the plateau, which adds more uncertainty to the fit. The eliminated spectrum has a slightly wider zero-loss peak which I took into account by a wider gaussian for the zero-loss peak in the fit. It is not surprising that the zero-loss width varies between the different microspheres since their conductivity and therefore surface potential differs, thus influencing the trajectories of the electrons. The main difference is around 4 eV. The fit shows a bigger signal

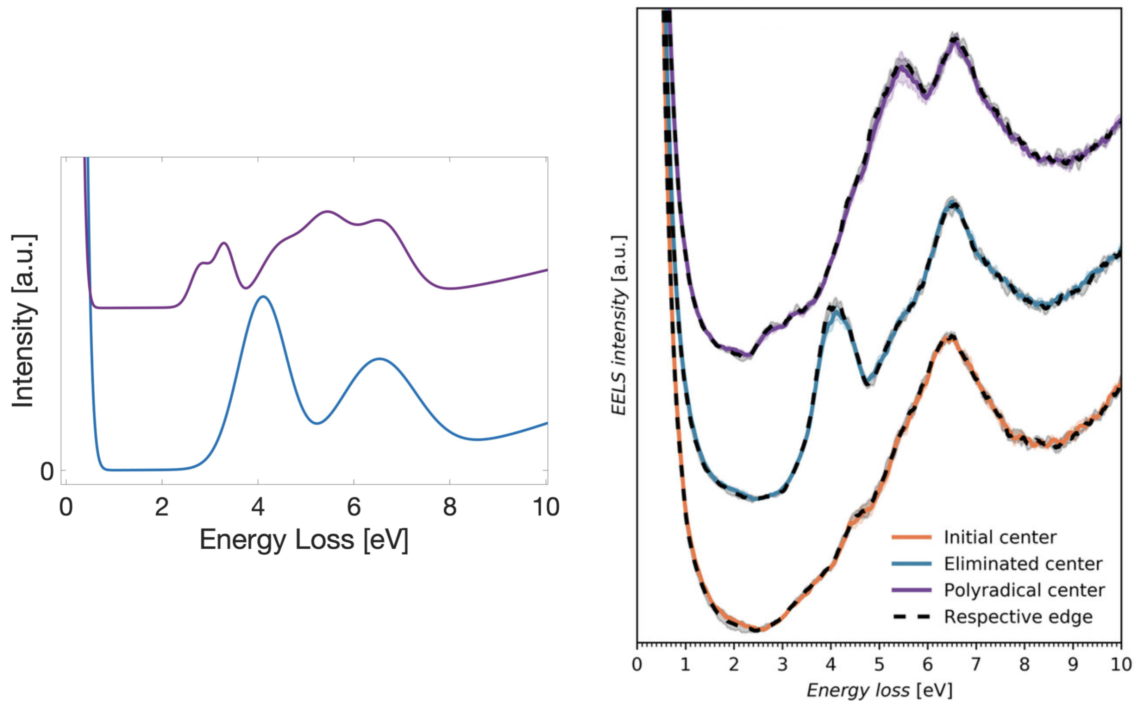


Figure 12.15: Fitted model for the polyradical (purple line) and eliminated (blue line) microspheres (left) together with the TEM EELS spectra (Kammerer et al. [2023]) (right) from the same sample preparation. The 'initial' state of the microspheres shown in the TEM plot was not studies in the bsEELS experiment.

difference there than it is is present in the bsEELS data. However, also in the data the signal from the eliminated spheres is constantly above the polyradical spheres from 3 eV to 5 eV energy loss. The signal difference is subtile and definitely smaller than the standard deviation. But, fitting the eliminated data without the reference peak at 4.1 eV (for instance using the same model as for the polyradical spheres) gives a worse fit which does not represent the data at this energy interval. This indicates that there is a real underlying signal difference between the bsEEL spectra of the different materials.
Comparing the resulting bsEELS fits and the reference TEM data, the same tendency is visible: Lower energy excitations seem to have a higher cross section in bsEELS compared to TEM EELS. For the polyradical, the peaks at 2.8 eV and 3.3 eV which have very low intensity in the TEM EEL spectrum, have high intensities in the bsEELS fit. Also the small shoulder at 4.4 eV has a higher signature in the bsEEL spectrum. The pronounce double peak in the TEM spectrum at 5.4 eV and 6.6 eV has relative to the other peaks a lower signal intensity in the bsEEL spectrum, also the signal intensity of the two peaks is inverted in the bsEELS signal and TEM EELS signal. The spectra of the eliminated microspheres show the same tendency: The first peak at 4.1 eV has a higher intensity in the bsEELS fit than the

6.5 eV peak, which is the other way around in the TEM data. The volume plasmon excitation at 15.5 eV and 16.0 eV for the polyradical and the eliminated peak respectively is higher for the eliminated spheres in the bsEEL spectra. The TEM data does unfortunately not include the volume plasmon peak, but the onset indicates that the volume plasmon has a higher intensity compared to the lower excitations in the TEM case. All resulting fit parameter are shown in table 12.3.

Table 12.3: Parameters for convolution fit of the microspheres in figure 12.14. ESF width reduced with width value = 5.

| | Mean | Sigma | Amplitude | Offset |
|---|---|---|---|---|
| Polyradical | | | | |
| Gauss Zero Loss | 0 | 0.15 | 1 | 0 |
| Gauss 1 | 2.8 | 0.2 | 0.01 | 0 |
| Gauss 2 | 3.3 | 0.2 | 0.015 | 0 |
| Gauss 3 | 4.4 | 0.4 | 0.012 | 0 |
| Gauss 4 | 5.4 | 0.5 | 0.021 | 0 |
| Gauss 5 | 6.6 | 0.5 | 0.018 | 0 |
| Gauss 6 | 15.5 | 4.2 | 0.022 | 0 |
| Eliminated | | | | |
| Gauss Zero Loss | 0 | 0.2 | 1 | 0 |
| Gauss 1 | 4.1 | 0.5 | 0.042 | 0 |
| Gauss 2 | 6.5 | 0.8 | 0.025 | 0 |
| Gauss 3 | 16.0 | 4.2 | 0.032 | 0 |

Although this experiment shows a larger uncertainty due to charging of the plastic sections and the signal difference between the two materials is smaller than the uncertainty, this result is encouraging since the fitted models show characteristic differences between both microspheres corresponding to a direct TEM reference of the same material system which fits the bsEELS measurements well.

### 12.3.2 Surface Charge Mapping with Secondary Electrons

The process of elimination and radicalization of the microspheres changes their properties so that polyradical state has a higher conductivity than the eliminated state (Kammerer et al. [2023]). We can use the secondary electron signal to evaluate the surface potential of the studied material and conclude a statement about the conductivity. Figure 12.16 shows inlens, backscattered and secondary electron images as well as the SE spectra of the different spheres and surrounding EPON at 700 eV, 500 eV and 150 eV primary energy.

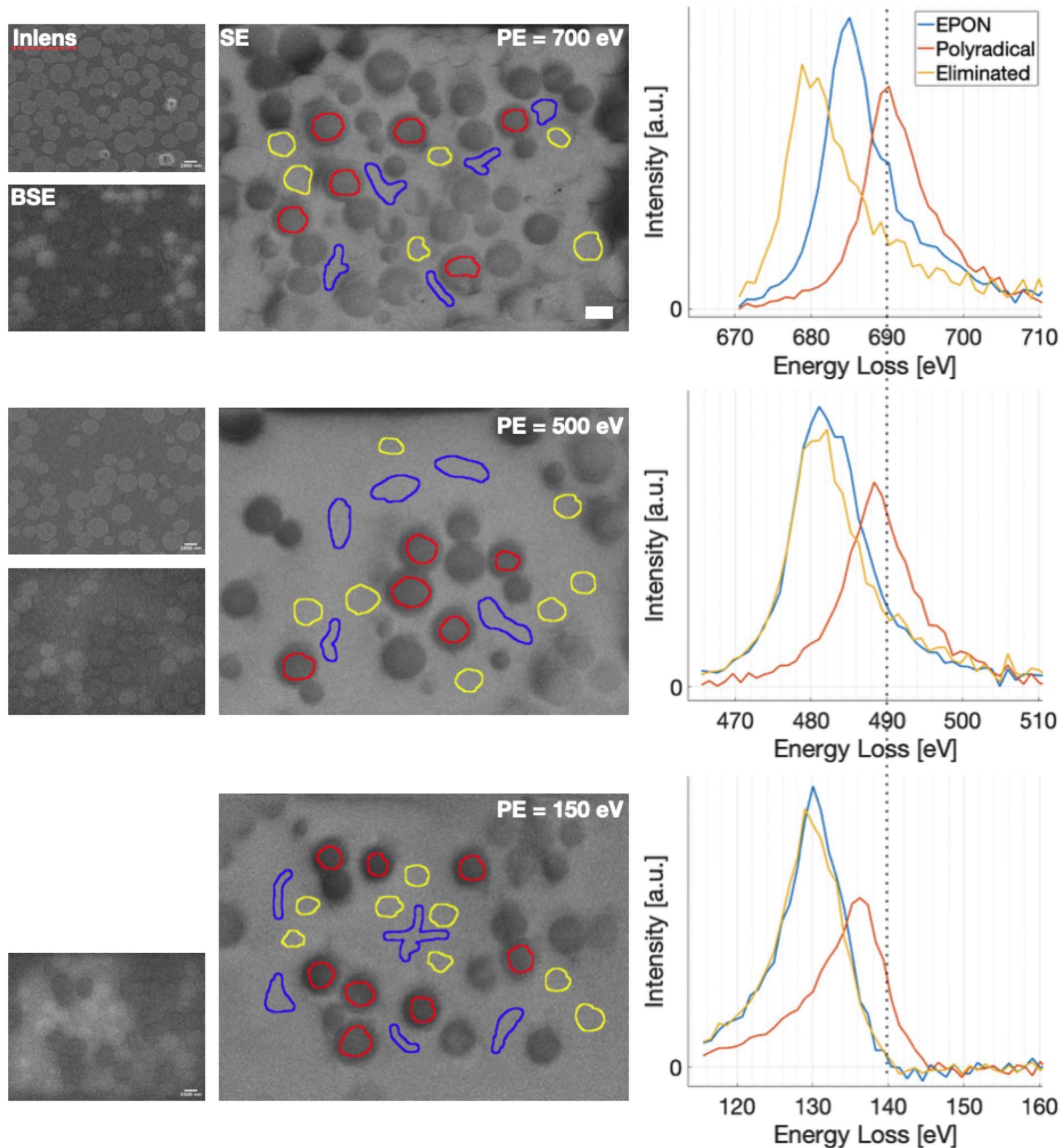


Figure 12.16: Secondary electron spectra of polyradical and eliminated microspheres embedded in EPON resin at 700 eV, 500 eV and 150 eV primary energy. SE images shown are recorded with DD grid at 30 V, BSE images at the onset of the SE peak with DD grid at −30 V. No inlens image can be recorded at 150 eV primary energy (see chapter 7). Scale bar = 1 µm.

A negatively charged surface gives emergent SE an additional acceleration towards the pole shoe, so that the energy of the SE is shifted towards higher energy – or lower energy loss in case of our axis. The SE peak of a conducting surface is located at 10 eV below the primary energy, so this is the 'neutral' position of the SE peak. At 700 eV the SE spectra show, that the polyradical material is not charged, whereas the eliminated polymer and the surrounding EPON charge nega-

tively of about −10 V and −5 V respectively indicated by the shift of the peaks. At 500 eV and 150 eV the eliminated spheres and the surrounding EPON show almost the same surface potential at about −10 V, while the SE peak of the polyradical is slightly shifted towards negative potential with decreasing primary energy as well. This effect might be explained by the penetration depth of the electrons: At higher primary energy the electrons penetrate the whole section and a larger fraction can easily reach the conducting support. At lower primary energy, more electrons are stopped closer to the surface of the section. The polyradical material has a higher conductivity, but still is not perfectly conductive, so if more electrons are deposited at the surface, they can not flow away quick enough to prevent a slight charging at lower primary energies. The difference in surface potential at 700 eV between eliminated polymer and EPON could also be explained by a difference in penetration depth of the electrons due to different density of the materials, or by a difference in the secondary electron yield dependent on the primary energy, which could cause the different surface potential.
The form of all SE peaks changes from 700 eV primary energy, where the left slope is steeper and towards lower energy at the right a flatter shoulder can be seen, to 150 eV, where it is the other way around and the higher energy side shows a flatter shoulder. This however, is most probably due to artifacts of the energy filter detector caused by the larger off-axis spread of the electrons at higher primary energy described in 9.1.
The SE images show a high contrast of the polyradical shares towards the surrounding EPON, whereas the eliminated spheres show almost no contrast. This makes a lot of sense due to the higher conductivity of the polyradical material and the equal non-conductivity of EPON and the eliminated material. Electrons accumulate in the non-conducting regions leading to a higher SE signal equal for both materials, while the radical materials can discharge towards the substrate leading to a lower SE output. The inlens images only show the high angle backscattering and there the contrast of the polyradical and eliminated spheres is identical, so they can not be distinguished. This shows that both microspheres are very similar in density and atomic composition, whereas the embedding EPON resin has a different composition.
The BSE signal shows an interesting and somewhat unexpected behavior: The eliminated spheres give a brighter contrast than the surrounding EPON and the polyradical spheres have the lowest signal intensity. We would have expected the same contrast for both spheres as in the case of the inlens images. On top of that, the BSE signal of the EPON resin from regions where more polyradical spheres are accumulated is darker and brighter where more eliminated spheres are present. This indicates that the surface potential or the presence/absence of accumulated electrons has an influence on the apparent backscattering coefficient. Even more interestingly, the surface potential has more influence on low angle backscattering (180° backscattering) shown in the BSE images from the Delta Detector than on high angle backscattering (90° parallel to the surface) shown in the inlens images.

More experiments like this might help to analyze the electron path from the sample into the detection path, an understanding necessary also for designing a model of the signal scrambling in our current instrument.
In addition, this experiment shows how the secondary electron signal can be used to characterize the surface potential of a multimaterial system and to compare the conductivity of the materials within the system. This was already successfully used to improve the characterization of charge carrier mobility in organic thin-film transistors (Zhang et al. [2021]).

# Part V

# Conclusion and Outlook

In this last part I will summarize the results and knowledge gained from the experiments and put them into perspective to the current state of the instrumental setup and the systematic uncertainties. Thereafter I will lay out possible steps to improve the current experimental state and to improve the performance of bsEELS experiments in order to develop this into a sophisticated, disruptive method for materials characterization.

# 13 Summary, further Discussion and Conclusion

Before I give a concise structured overview on the findings of this work, I want to point out the big result that was a bit shadowed by the details so far: **Energy Loss spectroscopy on backscattered electrons at high spatial resolution is indeed possible.** This is to our knowledge the first time this type of spectroscopy on BSE in a SEM is shown and that characteristic material spectra have been measured in the energy loss signal.

Figure 13.1 shows a direct comparison of spectra from Gold, Graphene and Silicon-

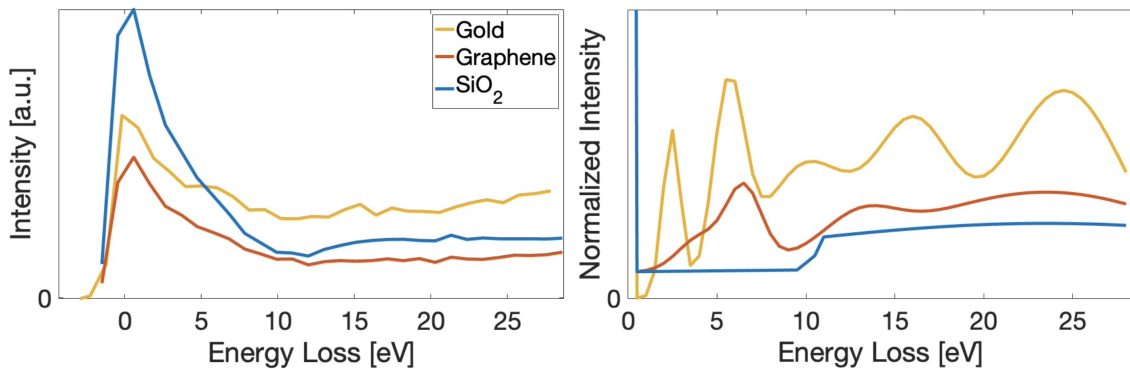


Figure 13.1: Experimental bsEEL spectra of Gold (at 80 eV PE), $SiO_2$ and Graphene (both at 100 eV PE) (left) together with the fitted models from TEM EELS references (right). The fitted spectra are shown and discussed in sections 9.3 ($SiO_2$), 10.1 (gold) and 11.1 (graphene).

wafer out of two different bsEELS experiments. The difference in the spectral form of the measured signal is obvious (figure 13.1, left panel) despite the limited energy resolution reduced by the effect of the ESF. We were able to fit the measured spectra with a model deduced from TEM EELS 'ground truth' (Keast and Bosman [2006] (gold), Wachsmuth et al. [2014] (graphene), Park et al. [2009] ($SiO_2$)) by fitting only the intensities of the excitations found in the reference data as free parameter to the bsEELS spectrum (figure 13.1, right panel). This clearly shows that BSE can be used for energy loss characterization equivalently to other electron spectroscopic methods. With this stated, let us discuss in more details the results described in the previous part.

### The ratio of cross-sections of different inelastic excitations is different in SEM compared to TEM

Throughout all experiments the data has shown that – comparing with TEM EELS at a typical primary energy of 100 keV – for bsEELS at 100 eV (order of magnitude) the inelastic cross-section for lower energy excitations (below 10 eV energy loss) is increased with respect to the excitations above 10 eV. In other words, **the mean energy loss[1] of low-energy electrons[2] is smaller in bsEELS experiments than in TEM EELS.**

This result may not be surprising - it is intuitive that with lower primary energy, the cross-section for higher energy excitations, where a large fraction of the incident energy has to be transferred, becomes smaller compared to lower energy excitations[3]. This means that the mean energy loss decreases with decreasing primary energy, which is in agreement with theory and REELS experiments as well (Tougaard [1997], see also section 4.2.3). It is an important feature of bsEELS that it is more sensitive for lowest energy excitations, i.e. optical transitions and surface plasmons. The former becomes very interesting in the study of organic and biological materials. As shown in the DNA experiments in section 12.1, the results suggest that fluorophore imaging with electrons could indeed be possible with bsEELS, which would allow a direct, high-resolution correlation of FM and EM images.

### Interaction volume, nature of interacting particle, and scattering geometry determines cross-sections

Regarding the intensity of surface plasmon excitations compared to volume plasmons, the small interaction at the surface should play a role as well. Compared to TEM EELS, where the electrons penetrate the whole volume, bsEELS is confined to the first few nanometers of the surface, so the signal of surface excitations should be higher in bsEELS compared to TEM EELS additionally to the lower mean energy loss of the electrons. Vice versa, volume plasmons at typical energies around 20 eV have a lower cross-section in bsEELS compared to TEM measurements.

When comparing spectral intensities of different experiments, we do also need to keep in mind that cross-sections differ for different scattering processes. Photons and electrons have different cross-sections for different interacting objects. The bsEELS spectra show this for instance in the tetra-phenyl cumulene results in section 12.2, where the UV/Vis spectra (excitation with photons) show different intensity-ratios of the excitation/absorption peaks than the bsEEL spectra. This is in agreement with HREELS experiments as well (Hoffmann et al. [2022]). But also within electron spectroscopic experiments, the cross-sections of different excitation 'channels' have different amplitudes depending on the experiment. Comparing the bsEELS

[1] The average energy loss of scattered electrons

[2] Scattered electrons with an energy below 100 eV

[3] With that said it is also trivial that excitations which would need more energy than available by the primary electron energy cannot be excited, their cross-section is zero for such electrons

and TEM EELS data in the case of gold (section 10.1) or the polymer microspheres (section 12.3), where multiple peaks are found in the first 10 eV energy loss, not only an intensity shift to lower energy excitations but also differences in the intensity ratios between different peaks can be observed. Note for instance the changed intensity of the 5.4 eV and 6.6 eV energy loss peaks of the polyradical microspheres in the bsEEL spectrum compared to the TEM EEL spectrum, while in contrast the peaks at 2.8 eV and 3.3 eV energy loss have similar ratios in both experiments.
Not only the difference in incident electron energy can play a role in the ratio of cross-sections for different excitations in a materials spectrum, but also the different scattering geometries: While for TEM EELS the electrons are scattered forward with near zero momentum transfer, we have up to full (180°) momentum transfer in the bsEELS case. This effect can be seen comparing HREELS (60° momentum transfer, Hoffmann et al. [2022]) and TEM EELS experiments as well, as is shown in figure 13.2. Comparing for example the intensity of the DAP $\alpha$-band transition at

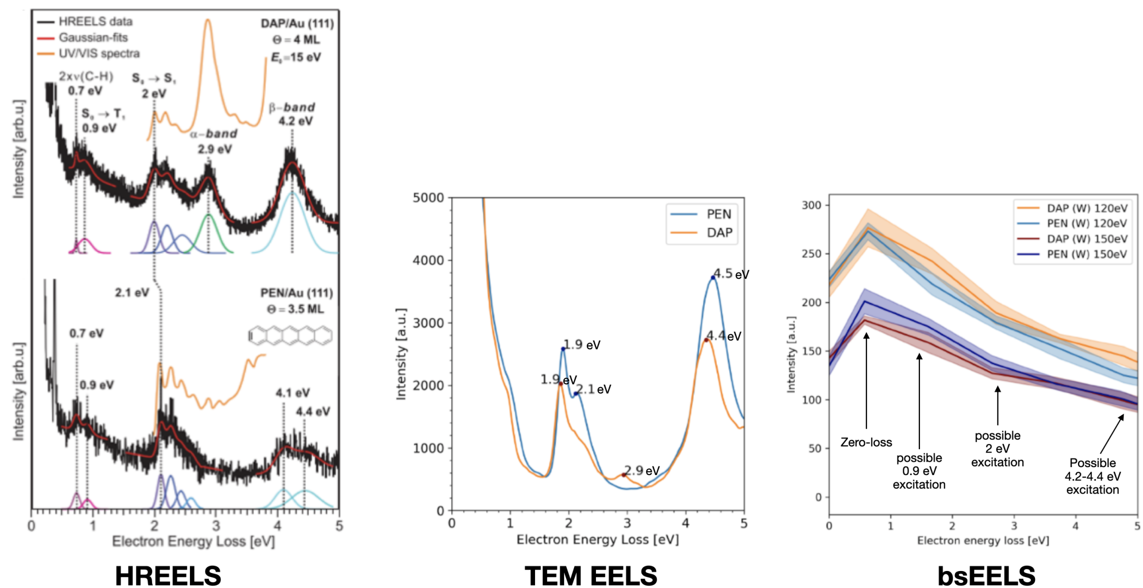


Figure 13.2: Comparison of the electron spectroscopic signal of pentacene and DAP with HREELS at 15 eV PE, TEM-EELS at 200 keV PE and bsEELS at 120 eV and 150 eV PE. (from Wrege [2022])

2.9 eV in the UV/Vis spectrum, HREEL and TEM-EEL spectrum with respect to the other excitations, it is obvious that the **ratio of the different excitations in a material vary significantly not only between photons and electrons, but also for electrons with different incident energy and momentum transfer.** Unfortunately, the bsEELS experiment for this specific material system did not yield sufficient signal to noise ratio due to strong surface charging for further evaluation of the data and was not included in the detailed simulation and discussion part of the experimental results for that reason. However, these preliminary data illustrate the differences to be expected between the different implementations of EEL spec-

troscopy.
bsEELS gives the capability to bridge studies between HREELS, which is mostly performed on few atomic layers of the material of interest deposited on a flat, bulk mono-crystalline surface and TEM-EELS on thin, freestanding layers on a grid-support. It is not possible to study one identical sample with HREELS and TEM-EELS, but samples from both methods can now be compared in the bsEELS setup, opening also more studies on electron interactions with different incident energy and momentum transfer.

### Limited energy resolution of the current bsEELS instrument

Moving on with the discussion of the bsEELS results in this work, it is undeniable that **the non-constant ESF**, which varies together with imaging parameters like surface potential and topography, **brings a large uncertainty with it, which is also difficult to asses at this stage.** The spectral form of the materials shown here in figure 13.1 can clearly be distinguished and carry significantly specifiable bsEELS signals. The differences in the bsEEL spectra are larger than the observed variation of the ESF for flat, conductive samples. So the confidence level is high comparing the fit results for these different materials.
When the bsEEL spectra are more similar, it helps to have an internal reference in the measurements. In our work we found the spectrum of $Si/SiO_2$ a very useful reference, as Si-wafers are a typical substrate for our samples. The Si-EEL spectrum has no excitations up to the band gap at about 9 eV to 10 eV. This way, the ESF form can be fitted to the zero- and low-loss part of the internal Si-wafer reference, directly accounting for imaging parameter related deviations of the ESF or contributions of residual contaminants. Thus, an effective ESF can be included in the spectrum fit of the material of interest. **With an internal, known reference spectrum, changes in the spectral response can be evaluated and considered in the simulation of the spectrum.** This made it possible to study, fit and compare the different spectra of graphene, carbon products of pyrolysis and DNA Origami experiments.

### Simulating experimental spectra, a first understanding of future deconvolution steps

The variation of the free parameters for the convolution fit was performed by hand, since we were not able to find and use automated protocols, like the least squares method, to produce a converging fit resembling the measured data. We have tried to find ways to fit the convolution problem, and were partially successful with the neural network fit shown in section 12.2, but had to confine the fit range to a small part of the spectrum there as well (King [2024]). For that reason we do not have a calculated variance of the fitted parameters as well, which makes the evaluation of the fit quality subjective to the observation of the plot. As already mentioned in the experimental part, a variation of the fitted intensities below about 50 % still gives a

decent fit, so a qualitative variance of 50 % can be assigned here. The influence of the variation of one fit parameter can be seen in appendix figure A.4 as an example. The energy loss values and widths of the peaks are taken as fixed parameters from reference measurement of other experiments, so are not varied during the fit. Nevertheless, the excitation amplitude (aka cross-section magnitude, see two paragraphs above) could in principle be different in case of this experimental setup, due to differences in sample preparation or due to the different contributions of the momentum transfer comparing TEM and bsEELS. This can also be seen in the shifted intensities in comparing HREELS and TEM-EELS in figure 13.2. So we need to keep in mind possible fit errors on the energy loss axis as well, which can not be quantified at this point.
With this said, we have to state that – while we clearly can measure a material dependent bsEELS signal with significantly different excitations like in the case of graphene on silicon (section 11.1) – **at this point of the experimental setup smaller differences between the models fitted to the measured data in the experiments on DNA with and without Cy3 (section 12.1) and on polymer microspheres (section12.3) are not significant.** It is encouraging that even small differences in the bsEELS data can be fitted with the corresponding reference excitations in a meaningful way, but the experimental setup needs to be improved in order to know the real form of the ESF and to reduce systematic uncertainties and noise.

### Will bsEELS be an analytical 3D method?

The experiments on the 3d-printed multicolor structures (section 10.2) and polymer microspheres (section 12.3) were in particularly interesting, since sectioning allows to study the inside of structures and devices with a surface sensitive method and the implementation of serial sectioning experiments (Array Tomography, Wacker and Schröder [2013]) would even allow large volume 3d reconstructions, which would be a big advantage over other electron spectroscopic methods.
The problem of imaging sections at ULV is surface charging. The common plastic resins used for embedding are not conductive, which is not a problem at conventional SEM beam energies of several keV, where most electrons penetrate through the 60 nm to 100 nm thick sections and can discharge through the support and sample holder. At ULV, however, all electrons accumulate at the surface of the section leading to charge accumulation and distortion of the image. In both examples shown in this work, the charging effect was acceptable since the embedded structures were at least partially conductive and allowed for a reasonable discharge of the surface. Still, the bsEEL spectra of the 3d-printed multicolor structures showed a large variance due to charging, which made it difficult to compare the spectra of different measurements. The conducting polyradical microspheres were more evenly distributed over the imaging area, which lead to a better charge distribution and more constant spectral results.
So at this stage we can say that **bsEELS can be used for studies on embed-**

**ded and sectioned materials – enabling volumetric and 3d-studies – if the embedded material of interest is sufficiently conductive to avert charging artifacts on the spectra.** A conductive embedding resin could enable the study of more, also non-conductive 3d structures, albeit the structures themself have to be small enough to enable a sufficient discharge by the surrounding resin.
For non-conductive materials, it would in principle be possible to find a so-called 'E-point' (Egerton et al. [2004]), a primary energy at which the net charging of a non-conductive sample becomes zero. However, these are not easy to find, especially for mixed material samples, and moreover the zero charging E-points are not necessarily at primary energies which give the best imaging conditions for bsEELS measurements. So there is no universal manual for bsEELS on non- or badly conductive materials, even though it is applicable for some structures and materials.

### bsEELS is highly surface sensitive

The experiments on graphene (section 11.1) and the flat DNA-origami (section 12.1) platelets show the high surface sensitivity of bsEELS. The contrast of few nanometer thick, light atom layers on silicon support is unprecedented for an electron probe characterization with nanometer spatial resolution. This is only achievable at ULV due to the small interaction volume and the evolution of the backscattering coefficient at low energies for these materials (see sections 4.2.2 and 4.2.1). The bsEEL spectra from free-standing single layer graphene and single layer graphene on support show no significant differences. Although we need to keep in mind that there is some amount of contamination on the backside of the imaged free-standing graphene, this clearly implies that **the signal of the bsEEL spectra at 80 eV PE stems from the single atomic layers of the sample**. An interesting question is, how many scattering events lead to the bsEEL signal – do we have an elastic backscattering event with preceding or subsequent inelastic scattering event resulting in the characteristic energy loss, or is it a combined/simultaneous inelastic backscattering event. Both should theoretically be possible. To answer the question we need to find a way to introduce contamination-free monolayer free-standing graphene into the microscope. Then the spectrum from a real monoatomic layer should only contain 'quasi single' scattering events, including a combined elastic/inelastic scattering channel.

### Can we detect the excitation of fluorescent organic molecules?

With the experiment on fluorescent quantum dots (section 10.2) we have shown that fluorescent excitations can be seen in the energy loss spectrum of BSE. The onset of the absorption spectrum of the quantum dots fits perfectly with the onset of the shoulder in the bsEEL spectrum, which is confirmed by the model fit. So if we now go to organic fluorophores, there should in principle be no difference regarding the interaction with the electronic system of the quantum dot or an organic molecule, bsEELS should show the signal of an organic fluorophore as well.
However, we need to state that we can not measure significant influence of Cy3

fluorophores bound to the DNA origami on the bsEELS signal compared to the reference data without bound Cy3 molecules at this point (see section 12.1). Although the convolution fits have shown a consistent change of the peak intensities – most notably at 0.8 eV energy loss, which would fit the energy of cis-trans isomerization of Cy3 bound to DNA (Spiriti et al. [2011]) – the intensity changes are not significant considering the variance of the fit. Still, this is an indication that bsEELS is sensitive enough to detect signal from organic fluorophores.
The main reason for the small signal from Cy3 molecules compared to the quantum dots is the small number of molecules: Only 12 Cy3 molecules were attached per origami, so the whole averaged spectrum contained the signal of at best 1500 molecules. A higher number and density of fluorescent molecules should give a more significant signal if the spectral differences originate from the fluorophore. New data from a master project by Felicitas Franke on fluorescent beads containing organic fluorophores with higher concentration show higher signal in the bsEEL spectrum, which needs to be confirmed yet. Another additional reason could be different excitation cross-sections between the quantum dots and Cy3. The quantum dots seem to have a distinct 'channel' at the absorption energy for the interaction with the electrons leading to a clear signal, whereas the Cy3-origami system has multiple 'excitation channels' leading to a signal harder to interpret after convolution with the ESF. We do also need to keep in mind that the quantum dots are less sensitive to beam damage compared to the organic molecules.

### Beam damage at ultra-low electron energies

The main source of beam damage in our setup is most probably chemical etching by the residual gas in the vacuum system. We have discussed in section 8.1 how this effect helps us to remove the surface contamination and measure a clean surface. For organic materials of course the chemical etching becomes a problem damaging the material of interest. It is currently not possible for us to distinguish between direkt beam damage of the electrons (i.e. direct bond breaking) and damage from chemical etching. The experiments in section 8.3 show that the beam damage is reduced with lower primary energy, a lower primary energy yet also has influence on the ionization rate of the residual gas and the acceleration of ions towards the sample surface (Toth et al. [2009]).
The typical dose with which we record bsEEL spectra before we start to see degradation of the sample in image or spectra in this work is 30 000 electrons per $nm^2$, which is higher than the critical dose for TEM studies on organic thin films for instance (Leijten et al. [2017]). So we can say that **beam damage for bsEELS measurements is reduced compared with TEM EELS.** To further reduce the beam damage the vacuum should be further improved. Also cooling the sample could help to reduce sample degradation, however, it could also lead to more accumulation of contamination on the cooled sample surface (water as well as hydrocarbons, depending on sample temperature), which then again would be counterproductive.

#### Secondary electron signal as additional information

In addition to the use of BSE we have shown that with the DELTA detector setup we can also **add information from secondary electrons.** In section 12.3 we have visualized the surface potential of polymer microspheres with almost identical atomic composition but different conductivity with help of the secondary electron spectrum.
The visualization of grain boundaries on the polycrystalline gold samples became apparent in an energy regime below 50 eV, where the signal of BSE and SE mix (see section 8.2.1). Therefore it is an interesting question here as well to which extent SE contribute to this effect.
As BSE, SE as well carry characteristic information, like Fermi energy and work function of the material (Cazaux [2010]). However, to extract this information a better understanding of the ESF in the range of the SE energy would be needed, for which we do not have any information at this point.

**To summarize, we were able to measure the bsEELS signal for a variety of different material systems. Moreover we were able to fit all measured spectra with a forward convolution of an experimental reference model from TEM EELS or UV/Vis data and a measured ESF of the microscope and detector system. This is the first time energy loss spectroscopy is performed on backscattered electrons in spatially resolved SEM spectral imaging. Although the experimental hardware and beam path design needs to be improved, the present data show the high potential of bsEELS to enhance the current possibilities of electron loss spectroscopic methods by adding surface sensitivity with nanometer spatial resolution. Measurements on bulk samples become accessible and high contrast can be accieved for organic and biological materials while reducing beam damage.**

# 14 Outlook

In this doctoral work spectroscopy with BSE in a SEM was studied for the first time. The study has brought detailed insight on how bsEELS can be approached with a SEM-like instrumentation and then used for spectral imaging on different materials and systems. It was essential to screen and study a variety of materials (i) to gain information about the spectral response of the detector system and to understand the influence of the ESF and (ii) to understand the influence of additional material characteristics – such as topography and conductivity – and thereby test the possible range of applications.

For the outlook we can now pursue two directions: One, how can we improve the experimental procedure in terms of sample preparation and measurement modalities in order to improve and expand the experimental outcome. And two, how to improve the experimental design – most importantly the detection system and data processing – in order to improve the energy resolution and reduce systematic uncertainties. The second point is crucial and probably indispensable in order to get reliable and significant results for real applications in materials and device characterization.

## 14.1 Improvement of the Experimental Procedure

For conductive materials, which are stable under beam irradiation and etching, the application of bsEELS is more or less straightforward and working well already at the current stage. The sample surface can be pre-cleaned by plasma treatment inside the microscope and leftover contaminants are removed by the beam-induced etching (see section 8.1). One improvement for these materials would be the implementation of a heating stage. This would give another possibility to remove contaminants from the surface inside the vacuum chamber of the SEM and also temperature dependent studies could be performed in-situ.

The capability of visualizing grain boundaries is a very interesting aspect which should be further studied on different material systems and could yield useful applications. Crystallinity is known to have an important impact on the performance of materials in different applications like capacitors, solar cells, photocatalysts and more (Cheng et al. [2020], Bansal et al. [2013], Di Paola et al. [2014]). Energy-filtered ULV SEM could enable a fast, large scale screening of the size and distribution of crystalline domains on a materials surface with nanometer resolution.

For organic, biological and other beam-sensitive materials the experimental approach needs more diligence due to the dose limitation. The implementation of a cryo-stage should be tested in order to reduce the beam damage, as it is successfully

done in TEM studies. One risk of this approach would be, however, that the cooling would introduce more contamination by trapping residual contaminants out of the chamber onto the sample. The instrument is currently equipped with a liquid nitrogen cryo-trap to improve the chamber vacuum – by subsequently cooling the trap and then the stage, an additional contamination of the sample surface might be prevented or at least reduced. This has to be tested. A general improvement of the chamber vacuum to UHV conditions would naturally improve the drawbacks of contamination and beam damage by etching, this, however, would require a new design of the specimen chamber and vacuum system which is not feasible at this point.
There is some room to improve the experimental outcome by finding the 'sweet spot' between contamination removal and sample damage during irradiation. In the work shown here, consecutive spectra were recorded on the same image region and the spectrum with the best image contrast – so with sufficient contamination removed but the material of interest (e.g. DNA-origami) still intact – was selected for further evaluation. This way a good measurement window was selected, but not necessarily the optimal point, since each spectrum introduced a rather large dose. By studying the development of contrast and sample texture of irradiated image surface with finer steps, an optimal dose might be found for the spectral acquisition with which the image is irradiated before the spectral measurement.
The results on fluorophore imaging (see section 12.1) were not conclusive since the difference between the sample with attached fluorophores and reference without was small with respect to the fitting variance. Reduced beam damage and finding the optimal point between surface cleaning and material damage as described in the paragraph above would certainly improve the signal. The change in the spectrum suggests that the cis-trans isomerization between DNA and Cy3 is excited and might be measured. To cross-check this other fluorophores with no possibility for isomerization need to be studied. Preliminary new data on polystyrene beads loaded with different fluorescent dyes show energy loss signals corresponding to their optical absorption energy.
If the imaging conditions can be further improved, single particle averaging (as known from Cryo-EM) on the Origami structures could help to reveal the fluorophore locations on the Origami. The great goal will be the direct detection of fluorophores with bsEELS to enable direct correlation of SEM images with high resolution FM methods.

The SE analysis shown in section 12.3.2 has demonstrated that we introduce negative charging when imaging on plastic sections at all primary energies for 100 eV to 1000 eV. This is contradicting to simulations shown by Cazaux [2005], where all studied plastics are supposed to show positive charging in that energy range. This is worth further investigations as well, since understanding the charging behavior is key for the studies of non-conductive materials. One approach for bsEELS experiments on non-conductive materials is to vary the primary energy to find the net-zero charging 'E-point', where the number of incoming and outgoing electrons is equal.

Positive charging can be dealt with by installation of a flood gun, which counters the positive charge by flooding the surface with low-energy electrons. These flood guns are usually used in X-ray photoelectron spectroscopy and ion beam analysis (Baer et al. [2002], Briggs et al. [1990]), but preliminary experiments performed in our group in a focussed ion beam SEM show that the implementation of a flood gun can have positive influence on SEM imaging of polymers as well (Bachelor Thesis Georgius [2023]). The influence of a flood-gun on bsEELS measurements with the DELTA SEM remains to be tested.

Overall bsEELS is a completely new method and approach and this work can only show a fraction of the accessible parameter range. Much more experiments need to be performed to understand the influence of different primary energies on the energy loss spectrum. In the present work, most experiments were performed at 80 eV primary energy since the contrast for organic materials is increased, BSE signal to noise ratio high and SE signal does not significantly contribute to the BSE signal (i.e. SEs can efficiently be separated from BSE in the recorded spectrum). But higher and lower PE might add more information, e.g. resulting from a higher cross-section for volume-plasmon excitations at higher incident electron energies. Also more studies at lowest achievable PE around 10 eV will definitely be interesting since this is the primary energy range equivalent to HREELS studies which then could be directly compared.
The range of different samples needs to be expanded as well in order to gain more and more experience on the experimental procedure and imaging possibilities. A lot has been learned during the experimental work on how to approach the search for optimized parameter settings, experimental measurement protocols and sample preparation; and there is for sure more to learn and improve by testing out more of the experimental parameter and material space.

But before starting more experiments, it would also be sensible to improve the detection system in order to get results which can be analyzed with a more sophisticated approach. One approach to achieve this will be discussed in the next section.

## 14.2 Detector Update and Implementation of Neural Network for Data Analysis

The shortcomings of the current design of the DELTA detector are explained in chapter 9. The best solution would be to redesign a corrected beam path towards the DELTA detector, so that the electrons are collimated on a defined trajectory and can be analyzed with an electric or magnetic field spectrometer in parallel. An electric or magnetic field spectrometer would be preferential over a retarding potential spectrometer because the spectrum can then be recorded in parallel instead of

cumulative, which would reduce the necessary electron dose, thus reducing possible beam damage.
This solution would require significant changes in the microscope hardware, which is costly and out of reach at present. A cheaper solution that can be implemented much faster is to exchange only the detector from the current single pixel scintillator to a 2D direct electron detector (and keeping the beam path as it is). This way more information per detector frame can be obtained including contributions of systematic errors from the retarding potential grid. This is illustrated in the schematic in figure 14.1.
There will be a radial distribution of hits from the statistical distribution of scat-

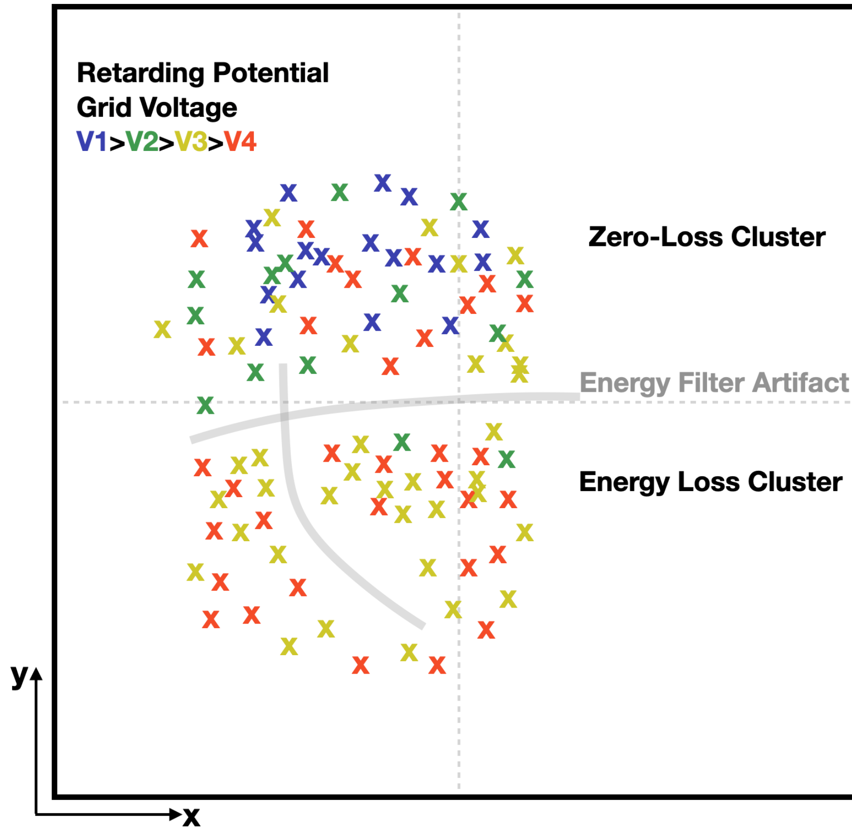


Figure 14.1: Schematic of the expected signal distribution on 2D detection for a single image pixel at different grid potentials (represented by the different colors) of the energy filter.

tering angles of the backscattered electrons. If this distribution shows a preferred direction this could be caused by a topographic orientation of the imaged structure, but also crystal orientation can influence the angular scattering distribution (Eves et al. [2000], Vos et al. [2010]).
This radial hit distribution will be stretched along the y-axis of the detector due to the energy dependent spreading of the electrons on the curved beam path toward the detector. In principle, a preferred energy loss signal should be detected as a

cluster on the 2D detector. If the energy filter is set close to the primary energy, only the zero-loss hit distribution should reach the detector (blue x's in the figure). The lower the grid voltage, the more electrons with different energies reach the detector and the higher should be the energy spread.
In addition to the above discussed expected hit distribution depending on energy, we expect systematic artifacts from the aberrations of the energy filter grid system which influence the hit distribution and is dependent on imaging settings such as primary energy, working distance and focus, but also on sample properties like charging and topography. As information about the hardware design from the manufacturing company Carl Zeiss Microscopy is very limited, we cannot calculate or model the exact beam path and the energy filter setup. Therefore, the distribution in the figure is just a schematic to explain the expected features on a 2D detector. The extent of the energy spreading might be much smaller and the artifacts different.
From basic optics, however, it is clear, that the whole hit cluster should move along the detector together with the beam deflection of the scan generator. At high magnifications – i.e. low scan deflection angles – the effect of shift should be small as well.

What is now gained with a 2d detector? If installed, we will have the possibility to read out additional informations from the sample/material (hit distribution, preferred angles, structure of the energy spread). But maybe more importantly, we will have additional information on the ESF from the structure of the artifacts observed in the hit distribution. The question will be, how to interpret the hit distributions to really gain information of the sample and detection process and to retrieve the high-resolution bsEEL spectrum from the spreading introduced by the detection system.
First ideas have been tested by implementation of an artificial neural network (ANN). ANNs have the advantage that explicit physical models for linking retrieved object features to a recorded signal are not necessarily needed if sufficient training data are available, which has been shown in resent applications (Wang et al. [2020a], Kalinin et al. [2022]). The results in section 12.2 show, that a simple convolutional neural network can be trained on available reference spectra and reference energy spread function to forward model the experimental spectrum with limited prior knowledge.
If enough training data can be collected with direct reference measurements from HREELS and/or TEM EELS, a well-designed ANN should be able to learn to separate the spectral material information from the introduced artifacts of the energy filter system and retrieve the materials EEL spectrum from the spectrum convoluted with the ESF.

# Part VI

# Appendix

# A Figures

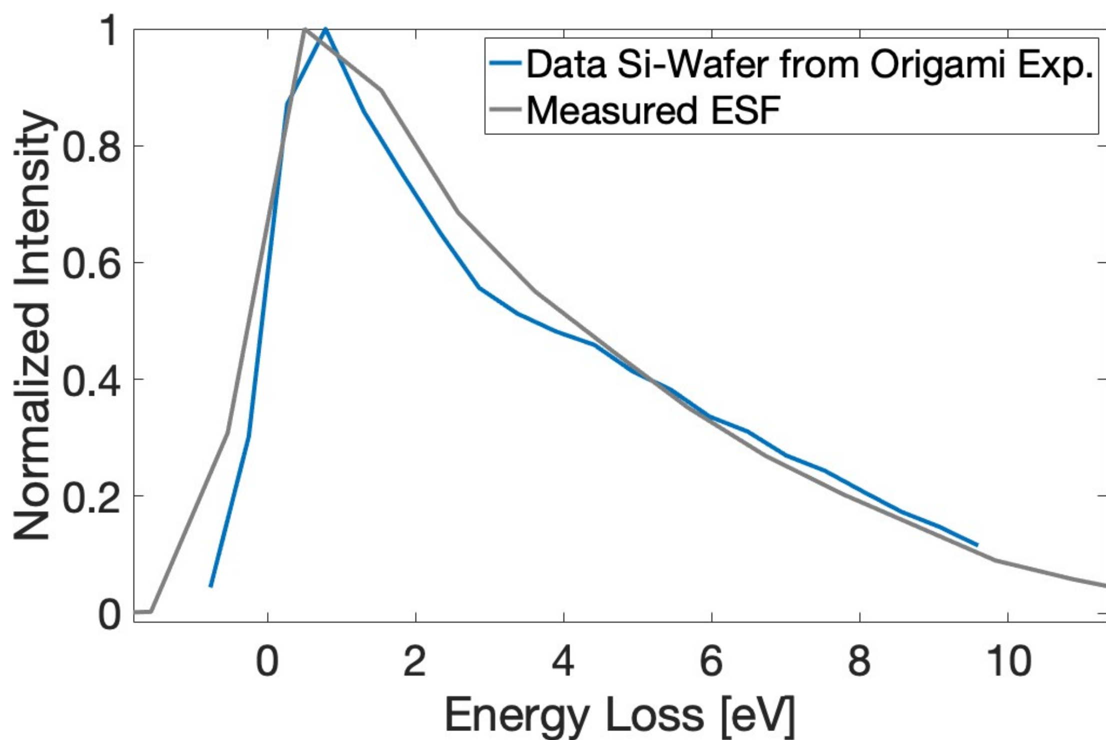


Figure A.1: Comparison of the Si-wafer spectrum from the DNA Origami experiment shown in figure 12.1 and the previously measured ESF. The ESF does not represent the width of the zero-loss Peak of the Si-wafer, thus the energy response is different in this experiement.

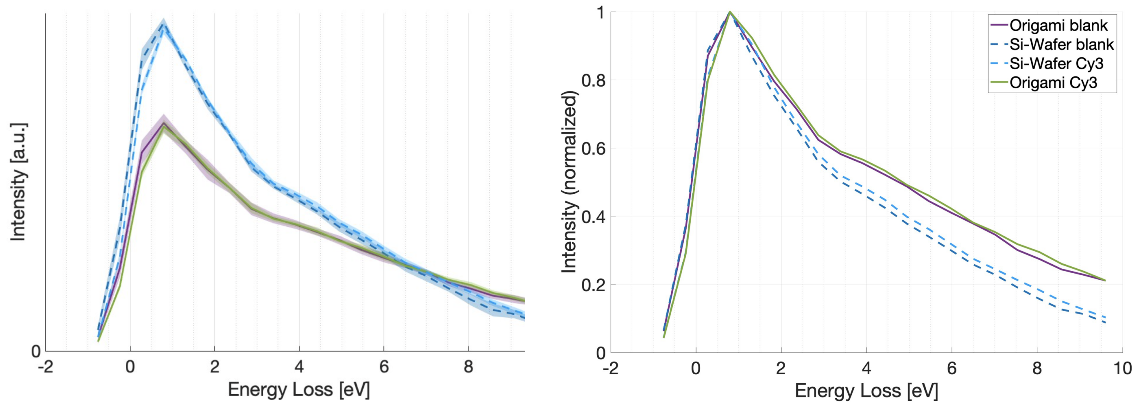


Figure A.2: bsEELS on DNA origami with and without Cy3 fluorophores at 80 eV from the second batch, each averaged over ten different measurements. Left: Raw spectra, right: normalized to the zero-loss peak. Corresponding to the fit evaluation shown in figure 12.8.

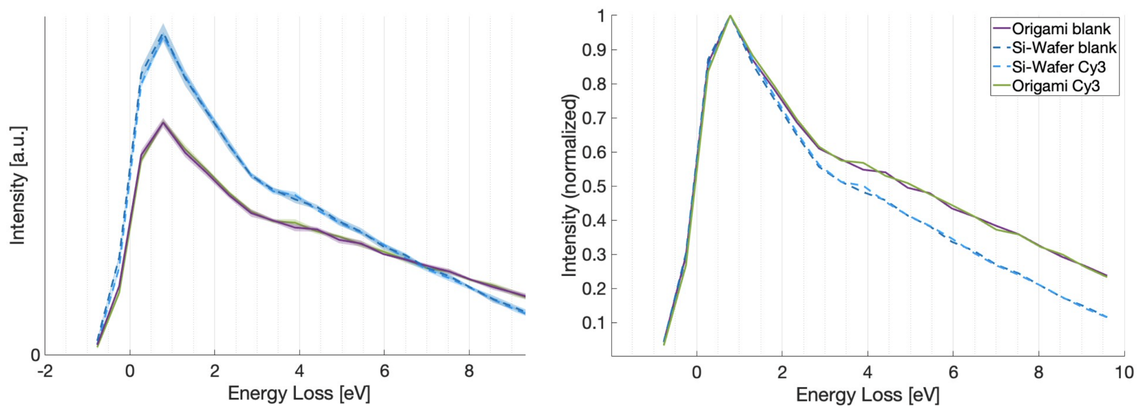


Figure A.3: bsEELS on DNA origami with and without Cy3 fluorophores at 40 eV from the second batch, each averaged over five different measurements. Left: Raw spectra, right: normalized to the zero-loss peak. Corresponding to the fit evaluation shown in figure 12.9.

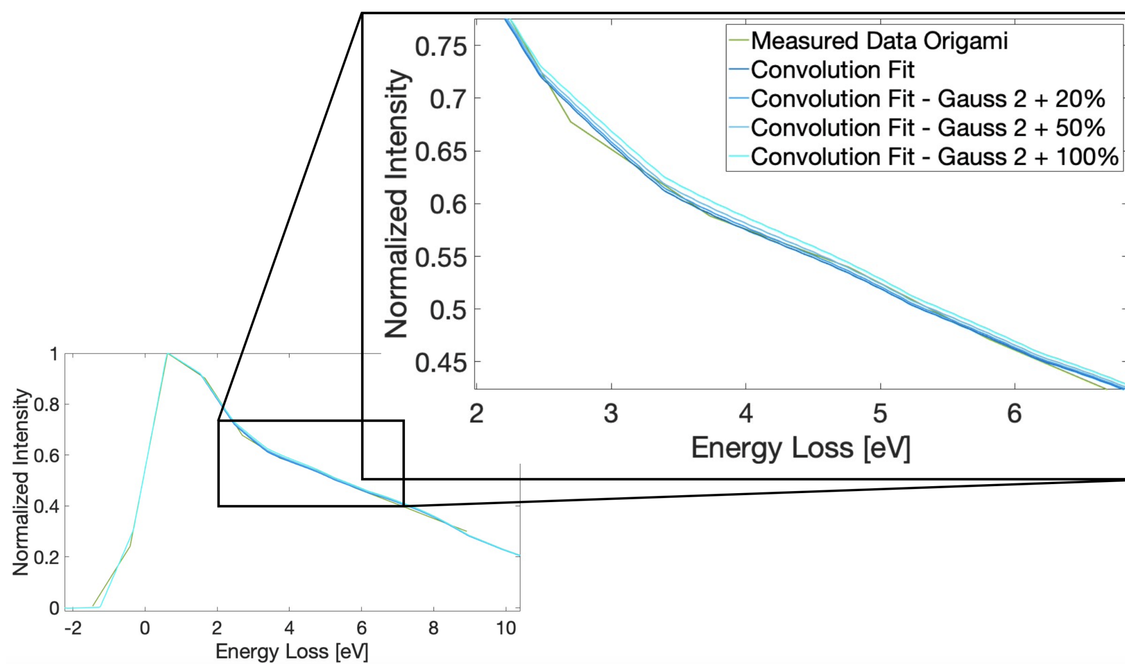


Figure A.4: Example of the influence from the variation of one fit parameter on the convolution fit. As exemplary data the origami with bound Cy3 from figure 12.6 was taken and the second excitation ('Gauss 2', 2.2 eV energy loss) was varied. A variation of 20 % still results in a decent fit. A variation of 50 % leads to the fit being constantly above the measured date in the fitting range. A variation of 100 % clearly does not represent the measured data.

# B Tables

Table B.1: Parameters for convolution fit in figure 12.8 (second batch, 80 eV).

| | Mean | Sigma | Amplitude | Offset |
|---|---|---|---|---|
| Silicon Wafer 'blank' (ESF width reduced by width value 5) | | | | |
| Gauss Zero Loss | 0 | 0.02 | 1 | 0 |
| Gauss 'Add' 1 | 4.0 | 0.5 | 0.0031 | 0 |
| Gauss 'Add' 2 | 6.5 | 1.0 | 0.0015 | 0 |
| Origami 'blank' (additional to $SiO_2$ signal) | | | | |
| **Gauss 1** | 0.8 | 0.3 | 0.0012 | 0 |
| **Gauss 2** | 2.2 | 0.5 | 0.0025 | 0 |
| Gauss 3 | 5.0 | 1.5 | 0.0014 | 0 |
| Gauss 4 | 10.0 | 3.0 | 0.0014 | 0 |
| Silicon Wafer 'Cy3' (ESF width reduced by width value 5) | | | | |
| Gauss Zero Loss | 0 | 0.02 | 1 | 0 |
| Gauss 'Add' 1 | 4.0 | 0.5 | 0.0037 | 0 |
| Gauss 'Add' 2 | 6.5 | 1.0 | 0.0017 | 0 |
| Origami 'Cy3' (additional to $SiO_2$ signal) | | | | |
| **Gauss 1** | 0.8 | 0.3 | 0.0017 | 0 |
| **Gauss 2** | 2.2 | 0.5 | 0.0021 | 0 |
| Gauss 3 | 5.0 | 1.5 | 0.0013 | 0 |
| Gauss 4 | 10.0 | 3.0 | 0.0012 | 0 |

Table B.2: Parameters for convolution fit in figure 12.9 (second batch, 40 eV).

| | Mean | Sigma | Amplitude | Offset |
|---|---|---|---|---|
| Silicon Wafer 'blank' (ESF width reduced by width value 5) | | | | |
| Gauss Zero Loss | 0 | 0.02 | 1 | 0 |
| Gauss 'Add' 1 | 4.0 | 0.5 | 0.0047 | 0 |
| Gauss 'Add' 2 | 6.5 | 1.0 | 0.0024 | 0 |
| Origami 'blank' (additional to $SiO_2$ signal) | | | | |
| **Gauss 1** | 0.8 | 0.3 | 0.0008 | 0 |
| **Gauss 2** | 2.2 | 0.5 | 0.0017 | 0 |
| Gauss 3 | 5.0 | 1.5 | 0.0013 | 0 |
| Gauss 4 | 10.0 | 3.0 | 0.0015 | 0 |
| Silicon Wafer 'Cy3' (ESF width reduced by width value 5) | | | | |
| Gauss Zero Loss | 0 | 0.02 | 1 | 0 |
| Gauss 'Add' 1 | 4.0 | 0.5 | 0.0045 | 0 |
| Gauss 'Add' 2 | 6.5 | 1.2 | 0.0022 | 0 |
| Origami 'Cy3' (additional to $SiO_2$ signal) | | | | |
| **Gauss 1** | 0.8 | 0.3 | 0.0011 | 0 |
| **Gauss 2** | 2.2 | 0.5 | 0.0015 | 0 |
| Gauss 3 | 5.0 | 1.5 | 0.0015 | 0 |
| Gauss 4 | 10.0 | 3.0 | 0.0015 | 0 |

# C Scripts for Data Evaluation

## C.1 Export Image Stack from Matlab File

```
1  function hd_exportSpectralImageStackToTiff( )
2  % export dd and inlense images and metadata to a directory
3
4  % 2017 Copyright Joerg Eisele, Universitaet Heidelberg
5
6  [inFileName, inPathName] = uigetfile('*.mat','Select the
     spectral image file');
7  outPath = uigetdir(inPathName, 'Select the output directory'
     );
8
9  inFullPath = strcat(inPathName, inFileName);
10 % spectral image structure
11 sis = open( inFullPath );
12
13 outBaseFileName = strcat( outPath, '/',  regexprep(
     inFileName, '\.mat$', ''), '__' );
14
15 % deactivated due to changes of the way how spectral images
     are saved
16 if false
17 % determine resolution
18 tempStrings = strsplit(parameters);
19 tempHit = regexp(tempStrings, 'Pixelsize=*');
20 for j = 1:length(tempHit)
21     if 1 == length( tempHit{1,j} )
22         pixelsize = regexprep( tempStrings(j), 'Pixelsize=',
             '');
23     end
24 end
25 tempHit = regexp(tempStrings, 'PixelSize=*');
26 for j = 1:length(tempHit)
27     if 1 == length( tempHit{1,j} )
28         pixelsize = regexprep( tempStrings(j), 'PixelSize=',
             '');
29     end
```

```
30 end
31
32 pixelsize = str2double(pixelsize);
33 pixelsizeUnit = 'm';
34
35 resolutionDPI = 1.0 / pixelsize / 0.0254;
36 resolutionDPIUnit = 'DPI';
37
38 resolutionDPM = 1.0 / pixelsize;
39 resolutionDPMUnit = 'dots per meter';
40 end % if
41
42 parameterString = strcat( ...
43     sis.ehtstring, '; ',    ...
44     sis.wdstring, '; ', ...
45     sis.magstring, '; ', ...
46     sis.pixelsizestring, '; ', ...
47     sis.SSstring, '; ', ...
48     sis.brightnessstring, '; ', ...
49     sis.contraststring, '; ', ...
50     sis.beamshiftstring, '; ', ...
51     sis.frametimestring, '; ', ...
52     sis.iebeforestring, '; ', ...
53     sis.ieafterstring, '; ', ...
54     sis.scmstatusstring, '; ', ...
55     sis.scmvaluestring ...
56   );
57
58 fid = fopen( strcat(outBaseFileName, 'description_tiff.txt')
     , 'w' );
59 % TODO: replace sis.parameters by more complete metadata
     description
60 fprintf(fid, 'Description of Images from Delta\n\nParameters
     \n**********\n\n%s\n%s\n%s\n%s\n%s\n%s\n%s\n%s\n%s\n%s\n%
     s\n%s\n%s\n\nVoltages\n********\n\n', ...
61     sis.ehtstring, ...
62     sis.wdstring, ...
63     sis.magstring, ...
64     sis.pixelsizestring, ...
65     sis.SSstring, ...
66     sis.brightnessstring, ...
67     sis.contraststring, ...
68     sis.beamshiftstring, ...
69     sis.frametimestring, ...
```

```
70      sis.iebeforestring, ...
71      sis.ieafterstring, ...
72      sis.scmstatusstring, ...
73      sis.scmvaluestring ...
74    );
75
76
77  for i = 1:length(sis.myimage)
78      %descriptionShort = strcat( 'voltage=', num2str(
          voltage_value(1,i)) );
79      descriptionShort = sprintf('DD; grid voltage=%d V; ',
          sis.voltage_value(1,i));
80      %descriptionLong  = strcat( {descriptionShort}, {
          parameters}, {'unit=m'} );
81      descriptionLong  = strcat( descriptionShort,
          parameterString );
82      %descriptionLong  = descriptionLong{1};
83      filename = sprintf('%s%s%03i%s%s%s', outPath, '/', i-1,
          '__' ,  regexprep(inFileName, '\.mat$', ''), '.tif');
84      %filename = sprintf('%s%s%06i%s', outBaseFileName, '
          ddImg', i-1, '.tif');
85      %imwrite(myimage{1,i}, filename, 'Description',
          descriptionLong, 'Resolution', resolutionDPI );
86      imwrite(sis.myimage{1,i}, filename, 'Description',
          descriptionLong);
87      [pathstr, name, ext] = fileparts(filename);
88      fprintf(fid, '%s%s: %d eV\n', name, ext, sis.
          voltage_value(1,i));
89  end
90  fclose(fid);
91
92  imwrite(sis.inlensimage{1,1}, strcat(outBaseFileName, '
      inlensImgBefore.tif'), 'Description', strcat('
      InlensBefore', parameterString) );
93  imwrite(sis.inlensimage{1,2}, strcat(outBaseFileName, '
      inlensImgAfter.tif'), 'Description', strcat('InlensAfter'
      , parameterString) );
```

## C.2 Replace Image Stack from Matlab File with Aligned Image Stack

```
1  function hd_replaceSpectralImagesByImageStack()
2
```

```
3 [inFileName, inPathName] = uigetfile('*.mat','Select
    spectral image file');
4 [stackFileName, stackPathName] = uigetfile('*.tif;*.tiff;*.
    png', 'Select the first image of the stack which will be
    used to replace the spectral images');
5 [outFileName, outPathName] = uiputfile('*.mat', 'Select the
    output file');
6
7 [pathstr, name, ext] = fileparts( strcat(stackPathName,
    stackFileName) );
8 stackBaseFileName = regexprep(name, '\d+$', '');
9 stackFirstIdString = regexp(name, '(?<idString>\d+$)', '
    names');
10 stackFirstIdString = stackFirstIdString.idString;
11 stackNumberOfIdDigits = length( stackFirstIdString );
12 stackFirstId = str2num( strcat( 'uint16(',
    stackFirstIdString, ')' ) );
13
14 % spectral image structure
15 sis = open( strcat(inPathName, inFileName) );
16 numberVoltages = length(sis.voltage_value);
17 if numberVoltages ~= length(sis.myimage)
18     error('Error: file not consistent');
19     return;
20 end
21
22 for i = 1:numberVoltages
23     formatString = strcat( '%s%s%0', int2str(
        stackNumberOfIdDigits), 'i', ext ) ;
24     newImageFileName = sprintf( formatString, stackPathName,
         stackBaseFileName, stackFirstId+i-1 );
25     newImage = imread( newImageFileName );
26     sis.myimage{1, i} = newImage;
27 end
28 save( strcat(outPathName, outFileName), '-struct', 'sis' );
```

## C.3 Export the Averaged Spectrum by Means of the Mapped Regions in the Mask-Files

```
1 function hd_exportAveragedSpectrumOfMappedRegionsFromFolder
    ()
2
3 [inFileName, inPathName] = uigetfile('*.mat','Select the
```

```
    spectral image file');
4 FileList = dir(fullfile(uigetdir(inPathName), '*.tif'));
5 for k = 1:length(FileList)
6   maskFileName = FileList(k).name;
7   maskPathName = strcat(FileList(k).folder, '/');
8   [filepathTIF,nameTIF,extTIF] = fileparts(maskFileName);
9   csvFileName = strcat(nameTIF, '.csv');
10  csvPathName = strcat(inPathName, 'Spektren/'); %Zielordner
       muss im Dateipfad angelegt sein
11 [pathstr, name, ext] = fileparts( strcat(csvPathName,
    csvFileName) );
12 csvDiffFileName = strcat(name, '_diff.csv');
13
14 % spectral image structure
15 sis = open( strcat(inPathName, inFileName) );
16 numberVoltages = length(sis.voltage_value);
17 if numberVoltages ~= length(sis.myimage)
18      error('Error: file not consistent');
19      return;
20 end
21
22 mask = imread( strcat(maskPathName, maskFileName) );
23 %maskMin = min(min(mask));
24 maskMax = max(max(mask));
25 maskSelector = NaN;
26 if 0 ~= maskMax
27      maskSelector = maskMax;
28 end
29 selection = (mask == maskSelector);
30 %selectionArea = sum(sum(selection));
31
32 averaged = NaN( 1, length(sis.myimage) );
33 for i = 1:numberVoltages
34      averaged(1, i) = mean( sis.myimage{1,i}(selection) );
35 end
36
37 midPositions = ( sis.voltage_value(1:(numberVoltages-1)) +
    sis.voltage_value(2:numberVoltages) )/2;
38 diff = ( averaged(2:numberVoltages) - averaged(1:(
    numberVoltages-1)) );
39
40 csvMatrix = NaN(numberVoltages, 2);
41 csvMatrix(1:numberVoltages, 1) = sis.voltage_value;
42 csvMatrix(1:numberVoltages, 2) = averaged;
```

```
43 csvwrite( strcat(csvPathName, csvFileName), csvMatrix );
44
45 csvDiffMatrix = NaN(numberVoltages−1, 2);
46 csvDiffMatrix(1:numberVoltages−1, 1) = midPositions;
47 csvDiffMatrix(1:numberVoltages−1, 2) = diff;
48 csvwrite( strcat(csvPathName, csvDiffFileName),
     csvDiffMatrix );
49 end
```

## C.4 Script for the Convolution Fit

Definition of the Gauss function in MatLab:

```
1 function yGauss = hd_SimpleGaussFunction(x,mu,sig,amp,vo)
2 %mu ist Mittelwert
3 %sig ist Standardabweichung
4 %amp ist Amplitude
5 %vo ist Offset
6 yGauss = amp*exp(−(((x−mu).^2)/(2*sig.^2)))+vo;
7
8 end
```

Script for the Convolution Fit:

```
1 %Define step size of the plot − use 0.01 if width of ESF has
      to be demagnified
2 x = −2:StepSize:28;
3 StepSize = 0.01;
4
5 %Spezial Model for the band gap onset of the SiO^2 TEM EELS
     Spectrum with
6 %StepSize = 0.5
7 ystep =
     [0.1,0.1,0.1,0.1,0.1,0.1,0.1,0.1,0.1,0.1,0.1,0.1,0.1,0.1,0.1,0.1,0.1,0

8 ySi = ystep.*(hd_SimpleGaussFunction(x,23.5,15.7,0.021,0.0))
     ;
9
10 %Set number of excitations and parameter values
     corresponding to reference
11 %model and fit.
12 yModel = hd_SimpleGaussFunction(x,0,0.02,1,0.00)+
     hd_SimpleGaussFunction(x,0.8,.3,0.0008,0.00)+
     hd_SimpleGaussFunction(x,2.2,.5,0.0017,0.00)+
     hd_SimpleGaussFunction(x,5,1.5,0.0013,0.00)+
     hd_SimpleGaussFunction(x,10,3,0.0015,0.0);
```

```
13
14 %Interpolate measured Energy Spread Function to defined step
      size
15 xq = 1:StepSize:33;
16 vq = interp1(ESF(:,2),xq);
17
18 %if necessary, reduce width of ESF by removing every n'th
     entry with ShortValue n
19 vqShort = vq;
20 ShortValue = 5;
21 for n = 1:(floor(length(xq)/ShortValue))
22     vqShort(:,(floor(length(vq)-n*ShortValue))) = [];
23 end
24 vqNew = [vqShort,zeros(1,floor(length(xq)/ShortValue))];
25
26 %Convolution of Fit Model with ESF
27 ySiConv = conv(ySi,vqNew);
28 yModelConv = conv(yModel,vqNew);
```

# D Lists

## D.1 List of Figures


2.1 Illustration of the signal mixing when imaging bulk material mixtures with different TEM and SEM methods. a) (S)TEM imaging of atomic layers introduces no signal mixing and produces a distinct atomic resolution signal. b) Bulk material mixtures need to be thinned below 100 nm and the projection though the sample leads to mixing of the signal from overlapping areas. c) For Standard SEM energies the interaction volume due to multiple scattering is still large in order of tens to hundreds of nanometer leading to signal mixing if the domains are smaller. d) With ultra-low voltage (ULV) SEM the interaction volume decreases to nanometer size, allowing to distinguish material domains at the surface down to nanometer resolution. . . . . . . . . . 14

4.1 Interaction of the electron probe with the sample in the SEM, generating secondary electrons (SE), backscattered electrons (BSE), and Photons (X). Hawkes and Reimer [2013] . . . . . . . . . . . . . . . . . 19

4.2 Electron spectrum generated in a SEM. SE: secondary electrons, AE: auger electrons, BSE: backscattered electrons, LLE: low-loss electrons. Hawkes and Reimer [2013] . . . . . . . . . . . . . . . . . . . . 20

4.3 Backscattering coefficient as a function of (a) energy for different materials, (b) atomic number for different primary energies. Hawkes and Reimer [2013] . . . . . . . . . . . . . . . . . . . . . . . . . . 21

4.4 Backscattering coefficient fitted for several experimental references versus primary electron energy for carbon, silicon and gold from Cazaux [2012]. . . . . . . . . . . . . . . . . . . . . . . . . . . . . . . 22

4.5 Origin of zero-loss BSEs (BS1) and BSEs with energy loss (BS2). Joy [1991] . . . . . . . . . . . . . . . . . . . . . . . . . . . . . . . . 23

4.6 Monte Carlo plots of electron scattering in carbon at nominal density of 1 g $cm^{-3}$ and for beam energies 1.5 keV, 5 keV and 20 keV. Joy and Pawley [1992] . . . . . . . . . . . . . . . . . . . . . . . . . . . 24

4.7 (a) Stopping power variation as a function of energy for an electron traveling through carbon. Joy and Joy [1996] (b) Variation of electron range as a function of energy. Goldstein et al. [2017] . . . . . . . . . . 25

4.8 Mean energy loss of electrons with kinetic energy E in different elements (Fitting et al. [2001]). . . . . . . . . . . . . . . . . . . . . . . . 26

4.9 Total electron yield $(\delta + \eta)$ and surface potential $V_S$ in a poorly conducting bulk specimen or thin film (dashed curve), as a function of incident-beam energy $E_0$. Egerton et al. [2004] . . . . . . . . . . . . . . 28

5.1 Schematic setup of a conventional SEM. (Wikipedia contributors [2019]) 31

5.2 (a) Picture of the DELTA Microscope, (b) schematic of the beam path through the components. Source: Carl Zeiss Microscopy (Oberkochen, Germany) (description edited). . . . . . . . . . . . . . . . . . . . . . . . 33

5.3 Schematic of the working principle of the Delta Detector. Only electrons with a kinetic energy above the grid potential can be detected. . 34

5.4 Example graph for spectral data acquisition (image of a serial section slice of mouse muscle) with the DD at 1 keV primary energy. For DD-Grid voltage below −1000 eV (threshold higher than the primary energy) no electrons can pass the grid, therefore only noise is measured. The Graph shows the intensity (gray value [a.u.]) averaged over all image pixels for each DD-Grid voltage step with a step size of 1 V. . . . . . . . . . . . . . . . . . . . . . . . . . . . . . . . . . 35

5.5 (a) Cumulative example BSE spectrum and (b) differentiated spectrum averaged over the whole image of a serial section slice of mouse muscle. . . . . . . . . . . . . . . . . . . . . . . . . . . . . . . . . . 36

5.6 (a) Cumulative and (b) differentiated single pixel spectrum of the example graph in figure 5.5. Intensity of each spectral point is averaged over five image scans (5 SpS), dwell time 3.2 µs per pixel. Note the extreme noise of such experimental data. . . . . . . . . . . . . . . . . 36

6.1 FM image of the functionalized PETA stucture with fluorescent markers after electron irradiation. Regions for the evaluation of the survival rate are exemplarily indicated (see text). . . . . . . . . . . . . 41

6.2 Example of manually created masks for further spectrum evaluation from DNA-origami and silicon wafer. Note that the distribution and size of the selected silicon wafer regions is on purpose distributed over the whole image to approximately match the size and distribution of the origamis in order to exclude systematic differences from spectral artifacts (‘anisochromaticity’, see chapter 7). . . . . . . . . . . . . . . 42

7.1 Schematic of the beam path through the components. Source: Carl Zeiss Microscopy (Oberkochen, Germany) (description edited). . . . . 44

7.2 Schematic of the trajectories of scattered electrons towards the inlens detector and ’Delta Detector’. . . . . . . . . . . . . . . . . . . . . . . . 45

7.3 Left: Inlens detector Images of a Si-wafer at 1000 eV and 80 eV at lowest magnification (Scale bar equals 200 µm). Note that the dark central circle is diffuse at 1000 eV whereas it has a clear edge at 80 eV. Areas indicate the evaluation area of the radial profile plot using Fiji plugin 'Radial Profile Angle' (Schindelin et al. [2012]). Right: Radial profile plots of the indicated areas. For 80 eV the intensity increases from 5 % to 80 % over a radial distance of 85 µm. For 1000 eV the same increase is over 305 µm. . . . . . . . . . . . . . . . . . . . . . . . 46

8.1 Electron beam induced processes affecting surface contamination. . . 49

8.2 (a) Overview of the experimental setup for AFM study of beam induced contamination change in the SEM. A grid pattern was etched onto the Si-wafer to relocate and correlate the irradiated areas from the SEM to the AFM. One can see the frames irradiation series inside the pattern. (b) AFM image of an electron-irradiated region from the SEM – ablation depth and wall hight were extracted and analyzed for different SEM imaging conditions (Schmidt-Kaler [2021]). . . . . . . . 50

8.3 Ablation of contamination in the central part of the SEM image versus primary beam energy under different conditions: black – normal chamber conditions, no sample treatment; red – improved vacuum by factor 2 with $LN_2$ cooled cryo-pump; blue – sample treated with plasma inside the microscope before irradiation; green – plasma-treatment before irradiation and improved vacuum with cryo-pump. Irradiation time was 10 min at 100 pA and 0.62 nm pixel size, corresponding to 1.24 million electrons per nm$^2$. . . . . . . . . . . . . . . . 51

8.4 Images of DNA-Origami platelets on Si-wafer after different numbers of scans. Each scan equals a dose of 2800 electrons per nm$^2$. At the first scan, the image is clearly blurry due to overlying contamination. With increasing scans, the contrast of the Origami increases – the contamination in the central image region reduces and the contamination frame at the edges builds up as expected. At scan 15 the contrast of the origami vanishes due to beam damage. Scale bar (frame scan 15) represents 100 nm. . . . . . . . . . . . . . . . . . . . . 52

8.5 Images of a polycrystalline gold surface under different imaging parameters. Backscattered electron image at 1000 eV (conventional SEM energy) shows no contrast in the spectral energy filter detector. Inset image at 1000 eV is recorded with the inlens detector in parallel and shows the gold domains and that the image is in focus. Note that all images are acquired with the same electron dose – contrast changes drastically under different imaging parameters at ULV with the spectral energy filter detector. Scale bars represent 100 nm. . 53

8.6 Top: Schematic and dimensions of the used DNA origami in this study (kindly provided by May Tran from AG Prof. Kerstin Göpfrich). The yellow string in the schematic represents surplus unfolded DNA material, which can also be observed in the images. Below are images of the origami on Si-wafer substrate recorded with different primary electron energies and filtered for backscattered electrons. The image at 1000 eV (conventional SEM energy) shows almost no contrast although it is in focus. White arrows point to gold fiducials. (The size of the origamis are 80x80 nm providing an intrinsic scale bar). . . . . 55

8.7 Graphene on carbon quantifoil imaged with different parameters. . . . 57

8.8 Graphene flakes on different substrates images at 80 eV PE and filtered for BSE. Left image is on carbon quantifoil substrate, middle image on gold quantifoil, right image on silicon wafer. . . . . . . . . . 57

8.9 Electron dose plotted agains the survival rate of Rhodamine B fluorescence after electron irradiation in the SEM for different primary energies. Rhodamine B was embedded in Epoxide resin and cut in 60 nm sections. Inset image shows a section with irradiated areas. Bange [2020] . . . . . . . . . . . . . . . . . . . . . . . . . . . . . . 60

8.10 Monte Carlo simulation of the penetration depth of electrons in epoxide resin. While the electrons penetrate almost the entire 60 nm section at 1 keV, only about 10 nm are reached at 250 eV. . . . . . . . . 61

8.11 Left: Schematic of the sample and a fluorescence image of the structures. Cy5 is used as fluorophore. Right: Survival rate of the fluorescence plotted as a function of the primary electron energy for two irradiation times. Scalebar represents 20 µm. . . . . . . . . . . . . . . 61

9.1 (a) Scheme of the working principle of the retarding grid spectrometer. The grid system is set to a voltage giving an energy potential which only electrons with sufficient kinetic energy are able to pass. By running the grid potential stepwise from the energy of the primary electrons to a target end step, an image stack with the information of a cumulative energy spectrum is recorded, which is illustrated with an example measurement (b). Two onsets can be seen, one is the elastic and inelastic BSE signal at zero/low energy loss, one the SE signal at highest energy loss. . . . . . . . . . . . . . . . . . . . . . . . 63

9.2 Schematic of the beam path towards the Delta Detector. Left side demonstrates the electron backscattering from the sample – the interaction volume and off-axis spread is much larger for conventional primary energy (top) compared to ultra-low voltage (bottom). Right side demonstrates the energy dependent spread due to Lorentz force on the beam path towards the detector. . . . . . . . . . . . . . . . . . . 64

9.3 A defect in a quantifoil hole gets charged and acts as a mirroring potential and thereby mapping the beam path through the grid system. Left image shows the charged area at the end voltage of the corresponding spectra at the right taken at 20 eV landing energy. Right spectra show the signal produced by different regions on the grid path and a averaged spectrum over the whole grid. . . . . . . . . . . . . . 65
9.4 Schematic representing the difference of a mirrored beam to scattered. The left side shows the charged defect at which the mirrored beam only takes one trajectory, so all electrons of an image point arrive at one point on the detector system. In contrast, for a scattered beam (right image) all trajectories are possible dependent on scattering angle and energy, so in general electrons from each image point can arrive on the whole detector surface. . . . . . . . . . . . . . . . . . . . 66
9.5 BSE and SE spectra of **Si-wafer** ($SiO_2$) from 16 eV to 50 eV. Spectra are normalized to their integral so the total signal is equal for all spectra. 67
9.6 BSE and SE spectra of polycrystalline **gold** from 16 eV to 50 eV. Spectra are normalized to their integral so the total signal is equal for all spectra. . . . . . . . . . . . . . . . . . . . . . . . . . . . . . . . . 68
9.7 SE-BSE ratio plot for $SiO_2$ and $Au$. . . . . . . . . . . . . . . . . . . . . 69
9.8 Example spectra of $SiO_2$ and $Au$. SE peak on the left, BSE on the right. . . . . . . . . . . . . . . . . . . . . . . . . . . . . . . . . . . . 69
9.9 Measured Energy Spread Function (full black line) which is caused by the beam spread on the path towards the Delta Detector described in detail in section 9.1. Dashed line is the result of a convolution of the colored gauss functions in the plot; it is just meant to illustrate and remind that the ESF results from the superposition of many different spectral signatures from different beam paths through the delta detector. . . . . . . . . . . . . . . . . . . . . . . . . . . . . . . 70
9.10 (a) Normalized Delta spectrum of a silicon wafer ($SiO_2$) at 80 eV PE. (b) Reference TEM EELS data used to model the spectral features (Park et al. [2009]). Onset energy of the bandgap signal (8.9 eV) is a fixed parameter, intensity of the plateau is a free parameter. . . . . . 71
9.11 Measured Delta spectrum of a Si wafer and convolution fit of the modeled TEM EELS reference with the ESF. . . . . . . . . . . . . . 72
9.12 Measured Delta spectrum of a contaminated Si wafer surface and convolution fit of the modeled TEM EELS reference with the ESF. The hydrocarbon contamination gives an additional wide signal at 5 eV (black arrows). . . . . . . . . . . . . . . . . . . . . . . . . . . . 73

10.1 Measured bsEELS spectrum at 80 eV primary energy and reference TEM EELS experiment (Keast and Bosman [2006]) on the upper right. Bottom right: Zoom in of fit model and TEM EELS reference; peak positions are set from the reference data, peak intensities are fitted to the bsEELS measurement. . . . . . . . . . . . . . . . . . . . . 76

10.2 bsEELS spectra at 80 eV primary energy from bright (grain surface) and dark (grain gaps) image parts of polycrystalline gold surface. Right images show the evaluated image regions (top: dark; bottom: bright). Evaluation regions were selected by thresholding the 20 % lowest and highest gray values respectively. . . . . . . . . . . . . . . . 77

10.3 Overview on the bsEELS experiment on 3d-printed structure quantum dot fluorophores. On the top the 3d-printed structure is shown (left) containing different fluorescent image layers (see Ref Mayer), a confocal LM image of the correlated layer (middle) and an EM image of the section containing the structure. The letter "E" can be seen on the section which was used to correlate to the corresponding layer and identify the structures containing the blue quantum dots. On the bottom: Averaged bsEEL spectra from four different measurements of the structure containing the QDots and the surrounding epoxide resin (EPON) with the standard deviation of the measurements. One exemplary image of an evaluated region is shown next to the graph. The spectra were taken at 100 eV primary energy with a total spectrum dose of 57 000 electrons per $nm^2$. . . . . . . . . . . . . . . . . . . . 79

10.4 Single measurements with corresponding image evaluation regions used to calculate the averaged spectrum in figure 10.3. . . . . . . . . 80

10.5 Convolution fit to the measured averaged spectrum in figure 10.3 assuming the excitation of the quantum dot absorption process. UV-Vis absorption spectrum used as fit reference is shown on the upper right (Elkabbash et al. [2019]), lower right shows the zoom in of the used gauss model. . . . . . . . . . . . . . . . . . . . . . . . . . . 81

11.1 bsEELS spectra recorded with 100 eV primary energy from graphene and the silicon wafer support. The indicated errors are the standard deviation of five consecutive measurements on the same area. Left: raw data. Middle: Data normalized to the integrated signal. Right: Reference image with the evaluated regions of interest. (From Wrege [2022]) . . . . . . . . . . . . . . . . . . . . . . . . . . . . . . . . 83

11.2 Model derived from TEM EELS (Wachsmuth et al. [2014]) and convolution fit to the bsEELS measurement in figure 11.1. The used parameters for the fit model of graphene are listed in table 11.1. Right panel shows a zoom in of the fit model. . . . . . . . . . . . . . . . . . 83

11.3 bsEELS spectra recorded with 80 eV primary energy from graphene and the silicon wafer support. The indicated errors are the standard deviation of five consecutive measurements on the same area. Left: raw data. Middle: Data normalized to the integrated signal. Right: Reference image with the evaluated regions of interest. (From Wrege [2022]) . . . . . . . . . . . . . . . . . . . . . . . . . . . . . . . . 84

11.4 Model derived from TEM EELS (Wachsmuth et al. [2014]) and convolution fit to the bsEELS measurement in figure 11.3. The used parameters for the fit model of graphene are listed in table 11.2. Right image shows a zoom in of the fit model with the fit model of the 100 eV measurement (dashed) as reference. . . . . . . . . . . . . . 85

11.5 bsEELS on graphene on a gold TEM grid at 80 eV primary energy. (a) evolution of the imaged region with increasing electron dose. Between each shown image are are about 220 image scans with a total dose of 2.685 million electrons per $nm^2$. (b) calculated images out of the spectral image stack (see text). The bright image parts have a larger contribution of the red shadowed area (graphene plasmon) and the dark image parts a larger contribution of the purple shadowed area (zero-loss) in the spectrum in c. (c) bsEEL spectra normalized to the integrated signal from the regions of interest showed on the right with the corresponding colors. . . . . . . . . . . . . . . . . . . . . . . . . 87

11.6 Model derived from TEM EELS reference and convolution fit to the bsEELS measurement of graphene and gold grid in figure 11.5. The used parameters for the fit model of graphene and gold are listed in table 11.3. Right image shows a zoom in of the fit model with the fit model. . . . . . . . . . . . . . . . . . . . . . . . . . . . . . . . . 89

11.7 Overview images taken at 150 eV primary energy. Left: Including SE signal. The image shows artifacts due to charging. Right: BSE image (DD-grid voltage at −50 V filtering out the SE). . . . . . . . . . . . 90

11.8 Images and bsEEL spectra from different products of the graphitization process with convolution fits to the carbon structure and underlying silicon wafer support. The two forms of carbon show different surface plasmon excitation in the fit. . . . . . . . . . . . . . . . . . . 91

12.1 bsEEL spectra together with the standard deviation taken at 40 eV of DNA origami on silicon wafer averaged over five different measurements. Right: Exemplary image of one measurement (scale bar 100 nm). . . . . . . . . . . . . . . . . . . . . . . . . . . . . . . . . 93

12.2 Measured ESF and ESF with reduced width to fit the data of origami on silicon wafer. . . . . . . . . . . . . . . . . . . . . . . . . . . . . 94

12.3 bsEEL spectra taken at 40 eV primary energy from origami and the silicon wafer substrate with convolution fits. Convolution models are shown to the right. . . . . . . . . . . . . . . . . . . . . . . . . . . 94

12.4 FM images (555 nm excitation wavelength, 3 s illumination time, scale bar 100 um) of DNA origami drop-cast on silicon wafer without (left) and with (right) Cy flourophores covalently bound. Below the FM images are exemplary SEM images of areas used for bsEELS analysis at 80 eV primary energy (scale bar 100 nm). . . . . . . . . . . . . . 95

12.5 bsEELS on DNA origami with and without Cy3 fluorophores at 80 eV each averaged over five different measurements. Left: Raw spectra, right: normalized to the zero-loss peak. . . . . . . . . . . . . . . . . . . 96
12.6 Model derived from LEE irradiation reference and convolution fits to the bsEELS measurements in figure 12.5. Left: Blank Origami. Right: Origami with Cy3. The used parameters for the fit model of Origami and silicon reference are listed in table 12.2. Lower image shows a zoom in of the fit model part of the Origami for both samples. 97
12.7 FM images (555 nm excitation wavelength, 3 s illumination time, scale bar 100 um) of a second batch of DNA origami drop-cast on silicon wafer without (left) and with (right) Cy flourophores covalently bound. Below the FM images are exemplary SEM images of areas used for bsEELS analysis at 80 eV primary energy (scale bar 100 nm). 99
12.8 Model derived from LEE irradiation reference and convolution fits to the bsEELS measurements of the second batch at 80 eV primary energy. Left: Blank Origami. Right: Origami with Cy3. The used parameters for the fit model of Origami and silicon reference are listed in table B.1. Lower image shows the fit model part of the Origami for both samples. . . . . . . . . . . . . . . . . . . . . . . . . . . . . . 100
12.9 Model derived from LEE irradiation reference and convolution fits to the bsEELS measurements of the second batch at 40 eV primary energy. Left: Blank Origami. Right: Origami with Cy3. The used parameters for the fit model of Origami and silicon reference are listed in table B.2. Lower image shows the fit model part of the Origami for both samples. . . . . . . . . . . . . . . . . . . . . . . . . . . . . . 101
12.10 Overview on the bsEELS experiment on the tetra-phenyl cumulenes at 100 eV primary energy. Left: bsEEL spectra of [3]PH at 100 eV primary energy averaged over eight measurements. Inset BSE image shows the crystals on the silicon-wafer substrate. Right: Structures and UV/VIS spectra of both materials. Arrows indicate the onsets of the excitations which correspond to the onsets of the signal 'shoulders' in the bsEELS data. From King [2024] . . . . . . . . . . . . . . . . . . 102
12.11 Result of the convolution fit performed by the neural network. Left: Measured data of [3]PH and [5]PH together with the fit curve. Red shading indicates the fit range for the neural network. Right: Plot of the resulting fit model for both materials. From King [2024] . . . . . 103
12.12 SEM image of the microspheres (scale bar 1 um) and the chemical structures of the polymerization and functionalization process (Kammerer et al. [2023]). Note that the Eliminated and Radical product vary in only one H Atom. . . . . . . . . . . . . . . . . . . . . . . . . . . 104
12.13 bsEEL spectra of the polyradical and eliminated microspheres averaged over two measurements from different areas. The spectra were taken at 80 eV primary energy. Right: BSE image of one image region with the selected spheres for the evaluation. Scale bar 1 um. . . . . . 105

12.14 bsEEL spectra of the polyradical and eliminated microspheres together with the convolution fits for both materials. The same data is shown in two plot to compare the fit accuracy (left) and the signal differences (right). The arrow points to the main spectral difference between the materials. . . . 105

12.15 Fitted model for the polyradical (purple line) and eliminated (blue line) microspheres (left) together with the TEM EELS spectra (Kammerer et al. [2023]) (right) from the same sample preparation. The 'initial' state of the microspheres shown in the TEM plot was not studies in the bsEELS experiment. . . . 106

12.16 Secondary electron spectra of polyradical and eliminated microspheres embedded in EPON resin at 700 eV, 500 eV and 150 eV primary energy. SE images shown are recorded with DD grid at 30 V, BSE images at the onset of the SE peak with DD grid at −30 V. No inlens image can be recorded at 150 eV primary energy (see chapter 7). Scale bar = 1 µm. . . . 108

13.1 Experimental bsEEL spectra of Gold (at 80 eV PE), $SiO_2$ and Graphene (both at 100 eV PE) (left) together with the fitted models from TEM EELS references (right). The fitted spectra are shown and discussed in sections 9.3 ($SiO_2$), 10.1 (gold) and 11.1 (graphene). . . . 112

13.2 Comparison of the electron spectroscopic signal of pentacene and DAP with HREELS at 15 eV PE, TEM-EELS at 200 keV PE and bsEELS at 120 eV and 150 eV PE. (from Wrege [2022]) . . . 114

14.1 Schematic of the expected signal distribution on 2D detection for a single image pixel at different grid potentials (represented by the different colors) of the energy filter. . . . 123

A.1 Comparison of the Si-wafer spectrum from the DNA Origami experiment shown in figure 12.1 and the previously measured ESF. The ESF does not represent the width of the zero-loss Peak of the Si-wafer, thus the energy response is different in this experiement. . . . 126

A.2 bsEELS on DNA origami with and without Cy3 fluorophores at 80 eV from the second batch, each averaged over ten different measurements. Left: Raw spectra, right: normalized to the zero-loss peak. Corresponding to the fit evaluation shown in figure 12.8. . . . 127

A.3 bsEELS on DNA origami with and without Cy3 fluorophores at 40 eV from the second batch, each averaged over five different measurements. Left: Raw spectra, right: normalized to the zero-loss peak. Corresponding to the fit evaluation shown in figure 12.9. . . . 127

A.4 Example of the influence from the variation of one fit parameter on the convolution fit. As exemplary data the origami with bound Cy3 from figure 12.6 was taken and the second excitation ('Gauss 2', 2.2 eV energy loss) was varied. A variation of 20 % still results in a decent fit. A variation of 50 % leads to the fit being constantly above the measured date in the fitting range. A variation of 100 % clearly does not represent the measured data. . . . . . . . . . . . . . . . . . . . . . . 128

## D.2 List of Tables

3.1 List of acronyms and abbreviations. . . . . . . . . . . . . . . . . . . . . . 17

4.1 $E_2$ values for different materials (Rau et al. [2008]). . . . . . . . . . . 29

6.1 Concentrations of the origami solutions. . . . . . . . . . . . . . . . . . 38

10.1 Parameters for convolution fit in figure 10.1. . . . . . . . . . . . . . . . 77
10.2 Comparison of peak amplitudes of the convolution fits between the 'bright' grain surfaces and 'dark' interspaces from figure 10.2. . . . . . 78
10.3 Parameters for convolution fit in figure 10.1. . . . . . . . . . . . . . . . 81

11.1 Parameters for convolution fit in figure 10.1. . . . . . . . . . . . . . . . 84
11.2 Parameters for convolution fit in figure 10.1. . . . . . . . . . . . . . . . 85
11.3 Parameters for convolution fit in figure 10.1. . . . . . . . . . . . . . . . 88
11.4 Parameters for convolution fit in figure 11.8. . . . . . . . . . . . . . . . 91

12.1 Parameters for convolution fit in figure 12.3. ESF width was reduced with Width Value = 5 . . . . . . . . . . . . . . . . . . . . . . . . . . . 95
12.2 Parameters for convolution fit in figure 12.6. . . . . . . . . . . . . . . . 98
12.3 Parameters for convolution fit of the microspheres in figure 12.14. ESF width reduced with width value = 5. . . . . . . . . . . . . . . . . 107

B.1 Parameters for convolution fit in figure 12.8 (second batch, 80 eV). . . 129
B.2 Parameters for convolution fit in figure 12.9 (second batch, 40 eV). . . 130

# E Publications Including the Author of this Thesis

[1] Jochen A. Kammerer, Florian Feist, Daniel Ryklin, Abhishek Sarkar, Christopher Barner-Kowollik, and Rasmus R. Schröder. Direct visualization of homogeneous chemical distribution in functional polyradical microspheres. Advanced Materials, 35(14), February 2023. ISSN 1521-4095. doi: 10.1002/adma.202211074. URL http://dx.doi.org/10.1002/adma.202211074.

[2] Frederik Mayer, Daniel Ryklin, Irene Wacker, Ronald Curticean, Martin Calkovsky, Andreas Niemeyer, Zheqin Dong, Pavel A. Levkin, Dagmar Gerthsen, Rasmus R. Schröder, and Martin Wegener. 3d two-photon microprinting of nanoporous architectures. Advanced Materials, 32(32), June 2020. ISSN 1521-4095. doi: 10.1002/adma.202002044. URL http://dx.doi.org/10.1002/adma.202002044.

[3] Irene Wacker, Ronald Curticean, Daniel Ryklin, Britta Weidinger, Frederik Mayer, Li-Yu Huang, Julian Hoffmann, Monsur Islam, Nadine von Coelln, Tanja Schmitt, Christian Huck, Petra Tegeder, Florian Feist, Jochen A. Kammerer, Christopher Barner-Kowollik, Martin Wegener, Eva Blasco, Ulrich Gengenbach, and Rasmus R. Schröder. Deconstructing 3d structured materials by modern ultramicrotomy for multimodal imaging and volume analysis across length scales. Advanced Functional Materials, July 2023. ISSN 1616-3028. doi: 10.1002/adfm.202302025. URL http://dx.doi.org/10.1002/adfm.202302025.

[4] Daniel Ryklin, Deborah Wrege, Giorgi King, Franz Schmidt-Kaler, Ronald Curticean, Irene Wacker, Rasmus R. Schröder. bsEELS: A new method for Electron Energy Loss Spectroscopy on backscattered electrons inside a Scanning Electron Microscope. In preparation, 2024.

[5] Daniel Ryklin, Franz Schmidt-Kaler, Deborah Wrege, Enrico Domenico Lemma,Kerstin Göpfrich, Irene Wacker, Rasmus Schröder. Imaging and Spectroscopy of Backscattered Electrons at Ultra-Low Energies—A New Characterization Approach for Beam Sensitive Organic Functional Materials. Oral presentation 2022 MRS Spring Meeting. URL https://www.mrs.org/meetings-events/presentation/2022_mrs_spring_meeting/2022_mrs_spring_meeting-3672642

[6] Daniel Ryklin,Jochen Kammerer,Rasmus Schroeder. Backscattered Electron Energy Loss Spectroscopy with an Analytical High-Resolution Ultra-Low-Voltage SEM. Oral presentation 2023 MRS Fall Meeting. URL https://www.mrs.org/meetings-events/presentation/2023_mrs_fall_meeting/2023_mrs_fall_meeting-3956025

Use of publications in this thesis:
From [1] reference TEM spectra were used to fit the bsEELS data in section 12.3 and to compare the bsEELS data with the TEM EELS data.
From [3] samples prepared with ultramicrotomy were used in the results shown in 10.2, 11.2 and 12.3.
A paper containing the results on bsEELS shown in this thesis is in preparation and is planned to be sent to one of the Nature series journals in June of 2024 [4].
Results from this work were presented at international conferences ([5],[6]).
The work from [2] is not used in this thesis.

# F Bibliography

E. T. Arakawa, S. M. Dolfini, J. C. Ashley, and M. W. Williams. Arc-evaporated carbon films: Optical properties and electron mean free paths. *Phys. Rev. B*, 31: 8097–8101, Jun 1985. doi: 10.1103/PhysRevB.31.8097. URL https://link.aps.org/doi/10.1103/PhysRevB.31.8097.

Clay B. Arrington, Daniel A. Rau, Johanna A. Vandenbrande, Maruti Hegde, Christopher B. Williams, and Timothy E. Long. 3d printing carbonaceous objects from polyimide pyrolysis. *ACS Macro Letters*, 10(4):412–418, March 2021. ISSN 2161-1653. doi: 10.1021/acsmacrolett.1c00032. URL http://dx.doi.org/10.1021/acsmacrolett.1c00032.

D. R. Baer, M. H. Engelhard, D. J. Gaspar, A. S. Lea, and C. F. Windisch. Use and limitations of electron flood gun control of surface potential during xps: two nonâhomogeneous sample types. *Surface and Interface Analysis*, 33(10-11):781–790, October 2002. ISSN 1096-9918. doi: 10.1002/sia.1454. URL http://dx.doi.org/10.1002/sia.1454.

Lukas Bange. Analyzing sample damage in scanning electron microscopy by studying the loss of fluorescence observed after electron irradiation. Master's thesis, Fakultät für Physik und Astronomie, Ruprecht-Karls-Universität Heidelberg, 2020.

Neha Bansal, Luke X. Reynolds, Andrew MacLachlan, Thierry Lutz, Raja Shahid Ashraf, Weimin Zhang, Christian B. Nielsen, Iain McCulloch, Dylan G. Rebois, Thomas Kirchartz, Michael S. Hill, Kieran C. Molloy, Jenny Nelson, and Saif A. Haque. Influence of crystallinity and energetics on charge separation in polymer-inorganic nanocomposite films for solar cells. *Scientific Reports*, 3(1), March 2013. ISSN 2045-2322. doi: 10.1038/srep01531. URL http://dx.doi.org/10.1038/srep01531.

H. Bethe. Zur theorie des durchgangs schneller korpuskularstrahlen durch materie. *Annalen der Physik*, 397(3):325–400, 1930. ISSN 1521-3889. doi: 10.1002/andp.19303970303. URL http://dx.doi.org/10.1002/andp.19303970303.

A. Bogner, P.-H. Jouneau, G. Thollet, D. Basset, and C. Gauthier. A history of scanning electron microscopy developments: Towards "wet-stem" imaging. *Micron*, 38(4):390 – 401, 2007. ISSN 0968-4328. doi: https://doi.org/10.1016/j.micron.2006.06.008. URL http://www.sciencedirect.com/science/article/pii/S0968432806001016. Microscopy of Nanostructures.

R. Böngeler, U. Golla, M. Kässens, L. Reimer, B. Schindler, R. Senkel, and M. Spranck. Electron-specimen interactions in low-voltage scanning electron microscopy. *Scanning*, 15(1):1–18, 1993. doi: https://doi.org/10.1002/sca.4950150102. URL https://onlinelibrary.wiley.com/doi/abs/10.1002/sca.4950150102.

D. Briggs, M. J. Hearn, I. W. Fletcher, A. R. Waugh, and B. J. McIntosh. Charge compensation and high-resolution tofsims imaging of insulating materials. *Surface and Interface Analysis*, 15(1):62–65, January 1990. ISSN 1096-9918. doi: 10.1002/sia.740150111. URL http://dx.doi.org/10.1002/sia.740150111.

R. E. Burge and D. L. Misell. Electron energy loss spectra for evaporated carbon films. *Philosophical Magazine*, 18(152):251–259, August 1968. ISSN 0031-8086. doi: 10.1080/00318086.1968.11716228. URL http://dx.doi.org/10.1080/00318086.1968.11716228.

J Cazaux. A new model of dependence of secondary electron emission yield on primary electron energy for application to polymers. *Journal of Physics D: Applied Physics*, 38(14):2433–2441, July 2005. ISSN 1361-6463. doi: 10.1088/0022-3727/38/14/020. URL http://dx.doi.org/10.1088/0022-3727/38/14/020.

J. Cazaux. Electron back-scattering coefficient below 5 keV: Analytical expressions and surface-barrier effects. *Journal of Applied Physics*, 112(8):084905, 10 2012. ISSN 0021-8979. doi: 10.1063/1.4759367. URL https://doi.org/10.1063/1.4759367.

Jacques Cazaux. Material contrast in sem: Fermi energy and work function effects. *Ultramicroscopy*, 110(3):242–253, 2010. ISSN 0304-3991. doi: https://doi.org/10.1016/j.ultramic.2009.12.002. URL https://www.sciencedirect.com/science/article/pii/S0304399109002721.

M.H. Chakrabarti, N.P. Brandon, S.A. Hajimolana, F. Tariq, V. Yufit, M.A. Hashim, M.A. Hussain, C.T.J. Low, and P.V. Aravind. Application of carbon materials in redox flow batteries. *Journal of Power Sources*, 253:150–166, 2014. ISSN 0378-7753. doi: https://doi.org/10.1016/j.jpowsour.2013.12.038. URL https://www.sciencedirect.com/science/article/pii/S0378775313020065.

J.P. Cheng, S.Q. Gao, P.P. Zhang, B.Q. Wang, X.C. Wang, and F. Liu. Influence of crystallinity of cuco2s4 on its supercapacitive behavior. *Journal of Alloys and Compounds*, 825:153–984, 2020. ISSN 0925-8388. doi: https://doi.org/10.1016/j.jallcom.2020.153984. URL https://www.sciencedirect.com/science/article/pii/S0925838820303479.

Christian Colliex. From electron energy-loss spectroscopy to multi-dimensional and multi-signal electron microscopy. *Journal of Electron Microscopy*, 60(suppl 1):S161–S171, 08 2011. ISSN 0022-0744. doi: 10.1093/jmicro/dfr028. URL https://doi.org/10.1093/jmicro/dfr028.

Wikipedia contributors. Scanning electron microscope, March 2019. URL https://en.wikipedia.org/w/index.php?title=Scanning_electron_microscope&oldid=886462964.

Maurizio Dapor, Robert C. Masters, Ian Ross, David G. Lidzey, Andrew Pearson, Isabel Abril, Rafael Garcia-Molina, Jo Sharp, Marek Unčovský, Tomas Vystavel, Filip Mika, and Cornelia Rodenburg. Secondary electron spectra of semi-crystalline polymers – a novel polymer characterisation tool? *Journal of Electron Spectroscopy and Related Phenomena*, 222:95–105, 2018. ISSN 0368-2048. doi: https://doi.org/10.1016/j.elspec.2017.08.001. URL http://www.sciencedirect.com/science/article/pii/S0368204817300695.

Swarup Dey, Chunhai Fan, Kurt V. Gothelf, Jiang Li, Chenxiang Lin, Longfei Liu, Na Liu, Minke A. D. Nijenhuis, Barbara SaccÃ, Friedrich C. Simmel, Hao Yan, and Pengfei Zhan. Dna origami. *Nature Reviews Methods Primers*, 1(1), January 2021. ISSN 2662-8449. doi: 10.1038/s43586-020-00009-8. URL http://dx.doi.org/10.1038/s43586-020-00009-8.

Agatino Di Paola, Marianna Bellardita, Leonardo Palmisano, Zuzana Barbieriková, and Vlasta Brezová. Influence of crystallinity and oh surface density on the photocatalytic activity of tio2 powders. *Journal of Photochemistry and Photobiology A: Chemistry*, 273:59–67, 2014. ISSN 1010-6030. doi: https://doi.org/10.1016/j.jphotochem.2013.09.008. URL https://www.sciencedirect.com/science/article/pii/S101060301300419X.

Hideto Dohi and Pieter Kruit. Design for an aberration corrected scanning electron microscope using miniature electron mirrors. *Ultramicroscopy*, 189:1–23, 2018. ISSN 0304-3991. doi: https://doi.org/10.1016/j.ultramic.2018.03.009. URL https://www.sciencedirect.com/science/article/pii/S0304399117305235.

T. Eberlein, U. Bangert, R. R. Nair, R. Jones, M. Gass, A. L. Bleloch, K. S. Novoselov, A. Geim, and P. R. Briddon. Plasmon spectroscopy of free-standing graphene films. *Phys. Rev. B*, 77:233–406, Jun 2008. doi: 10.1103/PhysRevB.77.233406. URL https://link.aps.org/doi/10.1103/PhysRevB.77.233406.

R.F. Egerton, P. Li, and M. Malac. Radiation damage in the tem and sem. *Micron*, 35(6):399–409, 2004. ISSN 0968-4328. doi: https://doi.org/10.1016/j.micron.2004.02.003. URL https://www.sciencedirect.com/science/article/pii/S0968432804000381. International Wuhan Symposium on Advanced Electron Microscopy.

Mohamed M. El-Gomati and Christopher G.H. Walker. Chapter one - toward quantitative scanning electron microscopy. volume 183 of *Advances in Imaging and Electron Physics*, pages 1–40. Elsevier, 2014. doi: https://doi.org/10.1016/

B978-0-12-800265-0.00001-1. URL https://www.sciencedirect.com/science/article/pii/B9780128002650000011.

Mohamed Elkabbash, Ermanno Miele, Ahmad Fumani, Michael Wolf, Angelo Bozzola, Elisha Haber, Tigran Shahbazyan, Jesse Berezovsky, Francesco De angelis, and Giuseppe Strangi. Cooperative energy transfer controls the spontaneous emission rate beyond field enhancement limits, 01 2019. URL https://www.researchgate.net/publication/330357872_Cooperative_energy_transfer_controls_the_spontaneous_emission_rate_beyond_field_enhancement_limits.

B. J. Eves, F. Festy, K. Svensson, and R. E. Palmer. Scanning probe energy loss spectroscopy: Angular resolved measurements on silicon and graphite surfaces. *Applied Physics Letters*, 77(25):4223–4225, December 2000. ISSN 1077-3118. doi: 10.1063/1.1333404. URL http://dx.doi.org/10.1063/1.1333404.

R. Fink, M.R. Weiss, E. Umbach, D. Preikszas, H. Rose, R. Spehr, P. Hartel, W. Engel, R. Degenhardt, R. Wichtendahl, H. Kuhlenbeck, W. Erlebach, K. Ihmann, R. Schlögl, H.-J. Freund, A.M. Bradshaw, G. Lilienkamp, Th. Schmidt, E. Bauer, and G. Benner. Smart: a planned ultrahigh-resolution spectromicroscope for bessy ii. *Journal of Electron Spectroscopy and Related Phenomena*, 84(1):231–250, 1997. ISSN 0368-2048. doi: https://doi.org/10.1016/S0368-2048(97)00016-9. URL https://www.sciencedirect.com/science/article/pii/S0368204897000169.

H.-J Fitting. Six laws of low-energy electron scattering in solids. *Journal of Electron Spectroscopy and Related Phenomena*, 136(3):265–272, 2004. ISSN 0368-2048. doi: https://doi.org/10.1016/j.elspec.2004.04.003. URL https://www.sciencedirect.com/science/article/pii/S0368204804002683.

H.-J. Fitting, E. Schreiber, J.-Ch. Kuhr, and A. von Czarnowski. Attenuation and escape depths of low-energy electron emission. *Journal of Electron Spectroscopy and Related Phenomena*, 119(1):35–47, 2001. ISSN 0368-2048. doi: https://doi.org/10.1016/S0368-2048(01)00232-8. URL https://www.sciencedirect.com/science/article/pii/S0368204801002328.

Ludvék Frank, Ilona Müllerová, Kenji Matsuda, and Susumu Ikeno. Cathode lens mode of the sem in materials science applications. *MATERIALS TRANSACTIONS*, 48(5):944–948, 2007. ISSN 1347-5320. doi: 10.2320/matertrans.48.944. URL http://dx.doi.org/10.2320/matertrans.48.944.

Yingxia Gao, Yi Zheng, and Léon Sanche. Low-energy electron damage to condensed-phase dna and its constituents. *International Journal of Molecular Sciences*, 22(15), 2021. ISSN 1422-0067. doi: 10.3390/ijms22157879. URL https://www.mdpi.com/1422-0067/22/15/7879.

Frederik René Georgius. Reducing positive charging on non conducting specimen in lvsem using a flood gun. Master's thesis, Department of Physics and Astronomy, Heidelberg University, 2023.

J.I. Goldstein, D.E. Newbury, J.R. Michael, N.W.M. Ritchie, J.H.J. Scott, and D.C. Joy. *Scanning Electron Microscopy and X-Ray Microanalysis*. Springer New York, 2017. ISBN 9781493966769. URL https://books.google.de/books?id=D0I_DwAAQBAJ.

F. S. Hage, G. Radtke, D. M. Kepaptsoglou, M. Lazzeri, and Q. M. Ramasse. Single-atom vibrational spectroscopy in the scanning transmission electron microscope. *Science*, 367(6482):1124–1127, 2020. doi: 10.1126/science.aba1136. URL https://www.science.org/doi/abs/10.1126/science.aba1136.

J.L. Hart, A.C. Lang, Y. Li, S. Shahrezaei, D.D. Alix-Williams, M.L. Falk, S.N. Mathaudhu, A.I. Frenkel, and M.L. Taheri. Revealing local order via high energy eels. *Materials Today Nano*, 21:100298, 2023. ISSN 2588-8420. doi: https://doi.org/10.1016/j.mtnano.2022.100298. URL https://www.sciencedirect.com/science/article/pii/S2588842022001262.

P.W. Hawkes and L. Reimer. *Scanning Electron Microscopy: Physics of Image Formation and Microanalysis*. Springer Series in Optical Sciences. Springer Berlin Heidelberg, 2013. ISBN 9783540389675. URL https://books.google.de/books?id=ulrvCAAAQBAJ.

Silvia Hernandez-Ainsa, Nicholas A. W. Bell, Vivek V. Thacker, Kerstin Göpfrich, Karolis Misiunas, Maria Eugenia Fuentes-Perez, Fernando Moreno-Herrero, and Ulrich F. Keyser. Dna origami nanopores for controlling dna translocation. *ACS Nano*, 7(7):6024–6030, June 2013. ISSN 1936-086X. doi: 10.1021/nn401759r. URL http://dx.doi.org/10.1021/nn401759r.

Marvin Hoffmann, Mohsen Ajdari, Felix Landwehr, Olena Tverskoy, Uwe H. F. Bunz, Andreas Dreuw, and Petra Tegeder. Influence of n-introduction in pentacene on the electronic structure and excited electronic states. *Physical Chemistry Chemical Physics*, 24(6):3924–3932, 2022. ISSN 1463-9084. doi: 10.1039/d1cp05273j. URL http://dx.doi.org/10.1039/D1CP05273J.

Kazi M. Zakir Hossain, Uresha Patel, and Ifty Ahmed. Development of microspheres for biomedical applications: a review. *Progress in Biomaterials*, 4(1):1–19, Mar 2015. ISSN 2194-0517. doi: 10.1007/s40204-014-0033-8. URL https://link.springer.com/content/pdf/10.1007/s40204-014-0033-8.pdf.

H. Ibach and J. Rajeswari. Electron energy loss spectrometers: An advanced operation mode for the lens system and the quantitative calculation of solid angle and transmission. *Journal of Electron Spectroscopy and Related Phenomena*, 185(3):61–70, 2012. ISSN 0368-2048. doi: https://doi.org/10.1016/j.elspec.

2012.01.001. URL https://www.sciencedirect.com/science/article/pii/S0368204812000059.

Monsur Islam, Joshua Flach, and Rodrigo Martinez-Duarte. Carbon origami: A method to fabricate lightweight carbon cellular materials. *Carbon*, 133: 140–149, 2018. ISSN 0008-6223. doi: https://doi.org/10.1016/j.carbon.2018.03.033. URL https://www.sciencedirect.com/science/article/pii/S0008622318302768.

Kevin Jahnke, Maja Illig, Marlene Scheffold, Mai P. Tran, Ulrike Mersdorf, and Kerstin Göpfrich. Dna origami signaling units transduce chemical and mechanical signals in synthetic cells. *Advanced Functional Materials*, June 2023. ISSN 1616-3028. doi: 10.1002/adfm.202301176. URL http://dx.doi.org/10.1002/adfm.202301176.

H Jaksch. The contrast mechanisms of ll-bse electrons in fe-sem characterization of polymer, single proteins, and oxidization states of elements. *Microscopy and Microanalysis*, 17(S2):902–903, Jul 2011. ISSN 1435-8115. doi: 10.1017/s1431927611005381. URL http://dx.doi.org/10.1017/S1431927611005381.

H. Jaksch. Hybridisation and band gap contrast from ll-bse electrons. *Microscopy and Microanalysis*, 18(S2):704–705, Jul 2012. ISSN 1435-8115. doi: 10.1017/s1431927612005375. URL http://dx.doi.org/10.1017/S1431927612005375.

David W. Johnson, Ben P. Dobson, and Karl S. Coleman. A manufacturing perspective on graphene dispersions. *Current Opinion in Colloid and Interface Science*, 20(5):367–382, 2015. ISSN 1359-0294. doi: https://doi.org/10.1016/j.cocis.2015.11.004. URL https://www.sciencedirect.com/science/article/pii/S135902941500093X.

D. C. Joy and S. Luo. An empirical stopping power relationship for low-energy electrons. *Scanning*, 11(4):176–180, 1989. ISSN 0161-0457. doi: 10.1002/sca.4950110404. URL http://dx.doi.org/10.1002/sca.4950110404.

David C. Joy. The theory and practice of high-resolution scanning electron microscopy. *Ultramicroscopy*, 37(1):216 – 233, 1991. ISSN 0304-3991. doi: https://doi.org/10.1016/0304-3991(91)90020-7. URL http://www.sciencedirect.com/science/article/pii/0304399191900207.

David C. Joy and Carolyn S. Joy. Low voltage scanning electron microscopy. *Micron*, 27(3):247 – 263, 1996. ISSN 0968-4328. doi: https://doi.org/10.1016/0968-4328(96)00023-6. URL http://www.sciencedirect.com/science/article/pii/0968432896000236.

David C. Joy and James B. Pawley. High-resolution scanning electron microscopy. *Ultramicroscopy*, 47(1):80 – 100, 1992. ISSN 0304-3991. doi: https://doi.org/10.

1016/0304-3991(92)90186-N. URL http://www.sciencedirect.com/science/article/pii/030439919290186N.

Sergei V. Kalinin, Colin Ophus, Paul M. Voyles, Rolf Erni, Demie Kepaptsoglou, Vincenzo Grillo, Andrew R. Lupini, Mark P. Oxley, Eric Schwenker, Maria K. Y. Chan, Joanne Etheridge, Xiang Li, Grace G. D. Han, Maxim Ziatdinov, Naoya Shibata, and Stephen J. Pennycook. Machine learning in scanning transmission electron microscopy. *Nature Reviews Methods Primers*, 2(1), March 2022. ISSN 2662-8449. doi: 10.1038/s43586-022-00095-w. URL http://dx.doi.org/10.1038/s43586-022-00095-w.

Jochen Kammerer, Riva Alkarsifi, Christine Videlot-Ackermann, Olivier Margeat, Bernd Schindler, Irene Wacker, Joerg Ackermann, Rasmus R Schroeder, and Martin Pfannmoeller. Statistical analysis of secondary electron spectroscopic images using ultra-low energies reveal nanoscale surface morphology of functional organic blends. *Microscopy and Microanalysis*, 24(S1):628–629, Aug 2018. ISSN 1435-8115. doi: 10.1017/s143192761800363x. URL http://dx.doi.org/10.1017/S143192761800363X.

Jochen A. Kammerer, Florian Feist, Daniel Ryklin, Abhishek Sarkar, Christopher Barner-Kowollik, and Rasmus R. Schröder. Direct visualization of homogeneous chemical distribution in functional polyradical microspheres. *Advanced Materials*, 35(14), February 2023. ISSN 1521-4095. doi: 10.1002/adma.202211074. URL http://dx.doi.org/10.1002/adma.202211074.

Myron D. Kapetanakis, Wu Zhou, Mark P. Oxley, Jaekwang Lee, Micah P. Prange, Stephen J. Pennycook, Juan Carlos Idrobo, and Sokrates T. Pantelides. Low-loss electron energy loss spectroscopy: An atomic-resolution complement to optical spectroscopies and application to graphene. *Phys. Rev. B*, 92:125–147, Sep 2015. doi: 10.1103/PhysRevB.92.125147. URL https://link.aps.org/doi/10.1103/PhysRevB.92.125147.

Haruma Kawaguchi. Functional polymer microspheres. *Progress in Polymer Science*, 25(8):1171–1210, 2000. ISSN 0079-6700. doi: https://doi.org/10.1016/S0079-6700(00)00024-1. URL https://www.sciencedirect.com/science/article/pii/S0079670000000241.

P. Kazemian, S.A.M. Mentink, C. Rodenburg, and C.J. Humphreys. Quantitative secondary electron energy filtering in a scanning electron microscope and its applications. *Ultramicroscopy*, 107(2):140–150, 2007. ISSN 0304-3991. doi: https://doi.org/10.1016/j.ultramic.2006.06.003. URL https://www.sciencedirect.com/science/article/pii/S0304399106001227.

Hiroyoshi Kazumori, Kazuhiro Honda, Miyuki Matsuya, Masaru Date, and Charles Nielsen. Field emission sem with a spherical and chromatic aberration corrector. *Microscopy and Microanalysis*, 10(S02):1370–1371, Aug 2004. ISSN 1435-

8115. doi: 10.1017/s1431927604881352. URL http://dx.doi.org/10.1017/S1431927604881352.

V Keast and Michel Bosman. Electron energy-loss spectroscopy: Measuring optical properties at the nanometre scale. *2006 NSTI Nanotechnology Conference and Trade Show - NSTI Nanotech 2006 Technical Proceedings*, 1, 01 2006.

Ye-Jin Kim, Levi D. Palmer, Wonseok Lee, Nicholas J. Heller, and Scott K. Cushing. Using electron energy-loss spectroscopy to measure nanoscale electronic and vibrational dynamics in a tem. *The Journal of Chemical Physics*, 159(5), August 2023. ISSN 1089-7690. doi: 10.1063/5.0147356. URL http://dx.doi.org/10.1063/5.0147356.

Giorgi King. Machine learning enhanced simulation of backscattered eel spectra from tetrahydrocummulenes. Master's thesis, Department of Physics and Astronomy, Heidelberg University, 2024.

E. Knapek and J. Dubochet. Beam damage to organic material is considerably reduced in cryo-electron microscopy. *Journal of Molecular Biology*, 141(2):147–161, 1980. ISSN 0022-2836. doi: https://doi.org/10.1016/0022-2836(80)90382-4. URL https://www.sciencedirect.com/science/article/pii/0022283680903824.

J.-Ch. Kuhr and H.-J. Fitting. Monte-carlo simulation of low energy electron scattering in solids. *physica status solidi (a)*, 172(2):433–450, April 1999. ISSN 1521-396X. doi: 10.1002/(sici)1521-396x(199904)172:2<433::aid-pssa433>3.0.co;2-x. URL http://dx.doi.org/10.1002/(SICI)1521-396X(199904)172:2<433::AID-PSSA433>3.0.CO;2-X.

Zino J. W. A. Leijten, Arthur D. A. Keizer, Gijsbertus de With, and Heiner Friedrich. Quantitative analysis of electron beam damage in organic thin films. *The Journal of Physical Chemistry C*, 121(19):10552–10561, May 2017. ISSN 1932-7455. doi: 10.1021/acs.jpcc.7b01749. URL http://dx.doi.org/10.1021/acs.jpcc.7b01749.

Enrico Domenico Lemma, Roberta Tabone, Kai Richler, Ann-Kathrin Schneider, Claudia Bizzarri, Franco Weth, Christof M. Niemeyer, and Martin Bastmeyer. Selective positioning of different cell types on 3d scaffolds via dna hybridization. *ACS Applied Materials and Interfaces*, February 2023. ISSN 1944-8252. doi: 10.1021/acsami.2c23202. URL http://dx.doi.org/10.1021/acsami.2c23202.

Martin Linck, Peter Hartel, Stephan Uhlemann, Frank Kahl, Heiko Müller, Joachim Zach, Max. Haider, Marcel Niestadt, Maarten Bischoff, Johannes Biskupek, Zhongbo Lee, Tibor Lehnert, Felix Börrnert, Harald Rose, and Ute Kaiser. Chromatic aberration correction for atomic resolution tem imaging from 20 to 80 kv. *Phys. Rev. Lett.*, 117:076101, Aug 2016. doi: 10.1103/PhysRevLett.117.076101. URL https://link.aps.org/doi/10.1103/PhysRevLett.117.076101.

Alejandra Londono-Calderon, Md Mir Hossen, Pierre E. Palo, Lee Bendickson, Sandra Vergara, Marit Nilsen-Hamilton, Andrew C. Hillier, and Tanya Prozorov. Imaging of unstained dna origami triangles with electron microscopy. *Small Methods*, 3(12), August 2019. ISSN 2366-9608. doi: 10.1002/smtd.201900393. URL http://dx.doi.org/10.1002/smtd.201900393.

David G. Lowe. Distinctive image features from scale-invariant keypoints. *International Journal of Computer Vision*, 60(2):91–110, November 2004. ISSN 0920-5691. doi: 10.1023/b:visi.0000029664.99615.94. URL http://dx.doi.org/10.1023/B:VISI.0000029664.99615.94.

Friedrich Maass, Mohsen Ajdari, Fairoja Cheenicode Kabeer, Maximilian Vogtland, Alexandre Tkatchenko, and Petra Tegeder. Nonadditivity of the adsorption energies of linear acenes on au(111): Molecular anisotropy and many-body effects. *The Journal of Physical Chemistry Letters*, 10(5):1000–1004, February 2019. ISSN 1948-7185. doi: 10.1021/acs.jpclett.9b00265. URL http://dx.doi.org/10.1021/acs.jpclett.9b00265.

E. Materna Mikmeková, I. Müllerová, L. Frank, A. Paták, J. Polčák, S. Sluyterman, M. Lejeune, and I. Konvalina. Low-energy electron microscopy of graphene outside uhv: electron-induced removal of pmma residues used for graphene transfer. *Journal of Electron Spectroscopy and Related Phenomena*, 241:146–873, 2020. ISSN 0368-2048. doi: https://doi.org/10.1016/j.elspec.2019.06.005. URL https://www.sciencedirect.com/science/article/pii/S0368204818302068. Sources, Interaction with Matter, Detection and Analysis of Low Energy Electrons (SIMDALEE2).

Frederik Mayer, Stefan Richter, Johann Westhauser, Eva Blasco, Christopher Barner-Kowollik, and Martin Wegener. Multimaterial 3d laser microprinting using an integrated microfluidic system. *Science Advances*, 5(2):eaau9160, 2019. doi: 10.1126/sciadv.aau9160. URL https://www.science.org/doi/abs/10.1126/sciadv.aau9160.

Frederik Mayer, Daniel Ryklin, Irene Wacker, Ronald Curticean, Martin Calkovsky, Andreas Niemeyer, Zheqin Dong, Pavel A. Levkin, Dagmar Gerthsen, Rasmus R. Schröder, and Martin Wegener. 3d two-photon microprinting of nanoporous architectures. *Advanced Materials*, 32(32), June 2020. ISSN 1521-4095. doi: 10.1002/adma.202002044. URL http://dx.doi.org/10.1002/adma.202002044.

Joseph R. Michael. High resolution at low beam energy in the sem: resolution measurement of a monochromated sem. *Scanning*, 33(3):147–154, May 2011. ISSN 1932-8745. doi: 10.1002/sca.20254. URL http://dx.doi.org/10.1002/sca.20254.

Lorenzo Mino, Elisa Borfecchia, Jaime Segura-Ruiz, Cinzia Giannini, Gema Martinez-Criado, and Carlo Lamberti. Materials characterization by synchrotron

x-ray microprobes and nanoprobes. *Rev. Mod. Phys.*, 90:025007, Jun 2018. doi: 10.1103/RevModPhys.90.025007. URL https://link.aps.org/doi/10.1103/RevModPhys.90.025007.

David A. Muller. Structure and bonding at the atomic scale by scanning transmission electron microscopy. *Nature Materials*, 8(4):263–270, Apr 2009. ISSN 1476-4660. doi: 10.1038/nmat2380. URL http://dx.doi.org/10.1038/nmat2380.

H. Müller, D. Preikszas, and H. Rose. A beam separator with small aberrations. *Journal of Electron Microscopy*, 48(3):191–204, 01 1999. ISSN 0022-0744. doi: 10.1093/oxfordjournals.jmicro.a023670. URL https://doi.org/10.1093/oxfordjournals.jmicro.a023670.

I. Müllerová and L. Frank. Very low energy microscopy in commercial sems. *Scanning*, 15(4):193–201, 1993. doi: https://doi.org/10.1002/sca.4950150403. URL https://onlinelibrary.wiley.com/doi/abs/10.1002/sca.4950150403.

H. Niedrig. Physical background of electron backscattering. *Scanning*, 1(1):17–34, 1978. ISSN 0161-0457. doi: 10.1002/sca.4950010103. URL http://dx.doi.org/10.1002/sca.4950010103.

Jucheol Park, Sung Heo, Jae-Gwan Chung, Heekoo Kim, HyungIk Lee, Kihong Kim, and Gyeong-Su Park. Bandgap measurement of thin dielectric films using monochromated stem-eels. *Ultramicroscopy*, 109(9):1183–1188, 2009. ISSN 0304-3991. doi: https://doi.org/10.1016/j.ultramic.2009.04.005. URL https://www.sciencedirect.com/science/article/pii/S0304399109001181.

James B. Pawley. *LVSEM for Biology*, pages 27–106. Springer New York, New York, NY, 2008. ISBN 978-0-387-72972-5. doi: 10.1007/978-0-387-72972-5_2. URL https://doi.org/10.1007/978-0-387-72972-5_2.

Michael. T. Postek. An approach to the reduction of hydrocarbon contamination in the scanning electron microscope. *Scanning*, 18(4):269–274, June 1996. ISSN 1932-8745. doi: 10.1002/sca.1996.4950180402. URL http://dx.doi.org/10.1002/sca.1996.4950180402.

É. I. Rau, E. N. Evstaf'eva, and M. V. Andrianov. Mechanisms of charging of insulators under irradiation with medium-energy electron beams. *Physics of the Solid State*, 50(4):621–630, Apr 2008. ISSN 1090-6460. doi: 10.1134/s1063783408040057. URL http://dx.doi.org/10.1134/S1063783408040057.

Ludwig Reimer. *Image Formation in Low-Voltage Scanning Electron Microscopy*. SPIE, February 1993. ISBN 9781510607996. doi: 10.1117/3.2265074. URL http://dx.doi.org/10.1117/3.2265074.

Daniel Ryklin. Studying the spectral signal of backscattered electrons in the delta scanning electron microscope: First experimental results and their implications

for imaging of fluorescent dyes and segmentation of biological tissue samples. Master's thesis, Department of Physics and Astronomy, University of Heidelberg, 2019.

D. R. McKenzie S. D. Berger and P. J. Martin. Eels analysis of vacuum arc-deposited diamond-like films. *Philosophical Magazine Letters*, 57(6):285–290, 1988. doi: 10.1080/09500838808214715. URL https://doi.org/10.1080/09500838808214715.

Léon Sanche. *Low Energy Electron Damage To DNA*, pages 531–575. Springer Netherlands, 2008. ISBN 9781402081842. doi: 10.1007/978-1-4020-8184-2_19. URL http://dx.doi.org/10.1007/978-1-4020-8184-2_19.

Lothar Schermelleh, Alexia Ferrand, Thomas Huser, Christian Eggeling, Markus Sauer, Oliver Biehlmaier, and Gregor P. C. Drummen. Super-resolution microscopy demystified. *Nature Cell Biology*, 21(1):72–84, January 2019. ISSN 1476-4679. doi: 10.1038/s41556-018-0251-8. URL http://dx.doi.org/10.1038/s41556-018-0251-8.

Johannes Schindelin, Ignacio Arganda-Carreras, Erwin Frise, Verena Kaynig, Mark Longair, Tobias Pietzsch, Stephan Preibisch, Curtis Rueden, Stephan Saalfeld, Benjamin Schmid, Jean-Yves Tinevez, Daniel James White, Volker Hartenstein, Kevin Eliceiri, Pavel Tomancak, and Albert Cardona. Fiji: an open-source platform for biological-image analysis. *Nature Methods*, 9(7):676–682, June 2012. ISSN 1548-7105. doi: 10.1038/nmeth.2019. URL http://dx.doi.org/10.1038/nmeth.2019.

Franz Schmidt-Kaler. Beam - sample interaction at ultralow electron energies between 20ev and 2kev in the delta scanning electron microscope. Master's thesis, Department of Physics and Astronomy, University of Heidelberg, 2021.

Rasmus R. Schroeder, Bernd Schindler, Michael Schnell, Christian Hendrich, Jakob Wensorra, Wen-Shan Zhang, Joerg Eisele, Lisa Veith, Jochen Kammerer, Martin Pfannmoeller, and et al. Delta - a novel ultra-low voltage sem for electron spectroscopic imaging. *Microscopy and Microanalysis*, 24(S1):626–627, Aug 2018. ISSN 1435-8115. doi: 10.1017/s1431927618003628. URL http://dx.doi.org/10.1017/S1431927618003628.

H Seiler. Secondary electron emission in the scanning electron microscope. *Journal of Applied Physics*, 54(11):R1–R18, Nov 1983. ISSN 1089-7550. doi: 10.1063/1.332840. URL http://dx.doi.org/10.1063/1.332840.

J. Spence, W. Qian, and X. Zhang. Contrast and radiation damage in point-projection electron imaging of purple membrane at 100 v. *Ultramicroscopy*, 55(1):19 – 23, 1994. ISSN 0304-3991. doi: https://doi.org/10.1016/0304-3991(94)90076-0. URL http://www.sciencedirect.com/science/article/pii/0304399194900760.

Justin Spiriti, Jennifer K. Binder, Marcia Levitus, and Arjan van der Vaart. Cy3-dna stacking interactions strongly depend on the identity of the terminal basepair. *Biophysical Journal*, 100(4):1049–1057, 2011. ISSN 0006-3495. doi: https://doi.org/10.1016/j.bpj.2011.01.014. URL https://www.sciencedirect.com/science/article/pii/S0006349511000609.

Qing Sun, Christian Dolle, Chantal Kurpiers, Kristian Kraft, Monsur Islam, Ruth Schwaiger, Peter Gumbsch, and Yolita M. Eggeler. In situ pyrolysis of 3d printed building blocks for functional nanoscale metamaterials. *Advanced Functional Materials*, July 2023. ISSN 1616-3028. doi: 10.1002/adfm.202302358. URL http://dx.doi.org/10.1002/adfm.202302358.

John Clark Sutherland and Kathleen Pietruszka Griffin. Absorption spectrum of dna for wavelengths greater than 300 nm. *Radiation Research*, 86(3):399, June 1981. ISSN 0033-7587. doi: 10.2307/3575456. URL http://dx.doi.org/10.2307/3575456.

Maria-Magdalena Titirici, Robin J. White, Nicolas Brun, Vitaliy L. Budarin, Dang Sheng Su, Francisco del Monte, James H. Clark, and Mark J. MacLachlan. Sustainable carbon materials. *Chemical Society Reviews*, 44(1):250–290, 2015. ISSN 1460-4744. doi: 10.1039/c4cs00232f. URL http://dx.doi.org/10.1039/C4CS00232F.

Milos Toth, Charlene J. Lobo, Michael J. Lysaght, Andras E. Vladar, and Michael T. Postek. Contamination-free imaging by electron induced carbon volatilization in environmental scanning electron microscopy. *Journal of Applied Physics*, 106 (3):034306, 08 2009. ISSN 0021-8979. doi: 10.1063/1.3187926. URL https://doi.org/10.1063/1.3187926.

Sven Tougaard. Universality classes of inelastic electron scattering cross-sections. *Surface and Interface Analysis*, 25(3):137–154, March 1997. ISSN 1096-9918. doi: 10.1002/(sici)1096-9918(199703)25:3<137::aid-sia230>3.0.co;2-l. URL http://dx.doi.org/10.1002/(SICI)1096-9918(199703)25:3<137::AID-SIA230>3.0.CO;2-L.

A Vladar and M Postek. Electron beam-induced sample contamination in the sem. *Microscopy and Microanalysis*, 11(S02):764–765, 08 2005. ISSN 1431-9276. doi: 10.1017/S1431927605507785. URL https://doi.org/10.1017/S1431927605507785.

Andras E. Vladar. Measurement of contamination rate and stage drift in scanning electron microscopes. In Bhanwar Singh, editor, *Metrology, Inspection, and Process Control for Microlithography XII*. SPIE, June 1998. doi: 10.1117/12.308789. URL http://dx.doi.org/10.1117/12.308789.

Maarten Vos, Koceila Aizel, and Aimo Winkelmann. Experimental observation of the strong influence of crystal orientation on electron rutherford backscattering

spectra. *Surface Science*, 604(11):893–897, 2010. ISSN 0039-6028. doi: https://doi.org/10.1016/j.susc.2010.02.016. URL https://www.sciencedirect.com/science/article/pii/S0039602810000695.

P. Wachsmuth, R. Hambach, G. Benner, and U. Kaiser. Plasmon bands in multilayer graphene. *Phys. Rev. B*, 90:235–434, Dec 2014. doi: 10.1103/PhysRevB.90.235434. URL https://link.aps.org/doi/10.1103/PhysRevB.90.235434.

I. Wacker, Irene and Rasmus R. Schröder. Array tomography. *Journal of Microscopy*, 252(2):93–99, September 2013. ISSN 1365-2818. doi: 10.1111/jmi.12087. URL http://dx.doi.org/10.1111/jmi.12087.

Irene Wacker, Ronald Curticean, Daniel Ryklin, Britta Weidinger, Frederik Mayer, Li-Yu Huang, Julian Hoffmann, Monsur Islam, Nadine von Coelln, Tanja Schmitt, Christian Huck, Petra Tegeder, Florian Feist, Jochen A. Kammerer, Christopher Barner-Kowollik, Martin Wegener, Eva Blasco, Ulrich Gengenbach, and Rasmus R. Schröder. Deconstructing 3d structured materials by modern ultramicrotomy for multimodal imaging and volume analysis across length scales. *Advanced Functional Materials*, July 2023. ISSN 1616-3028. doi: 10.1002/adfm.202302025. URL http://dx.doi.org/10.1002/adfm.202302025.

Feng Wang, Alberto Eljarrat, Johannes Müller, Trond R. Henninen, Rolf Erni, and Christoph T. Koch. Multi-resolution convolutional neural networks for inverse problems. *Scientific Reports*, 10(1), March 2020a. ISSN 2045-2322. doi: 10.1038/s41598-020-62484-z. URL http://dx.doi.org/10.1038/s41598-020-62484-z.

Guanyu Wang, Yujie Dai, Haiping Yang, Qingang Xiong, Kaige Wang, Jinsong Zhou, Yunchao Li, and Shurong Wang. A review of recent advances in biomass pyrolysis. *Energy and Fuels*, 34(12):15557–15578, November 2020b. ISSN 1520-5029. doi: 10.1021/acs.energyfuels.0c03107. URL http://dx.doi.org/10.1021/acs.energyfuels.0c03107.

Z.L. Wang and J.M. Cowley. Reflection electron energy loss spectroscopy (reels): A technique for the study of surfaces. *Surface Science*, 193(3):501–512, 1988. ISSN 0039-6028. doi: https://doi.org/10.1016/0039-6028(88)90449-9. URL https://www.sciencedirect.com/science/article/pii/0039602888904499.

Dominik Wendinger and Rik R. Tykwinski. Odd [n]cumulenes (n = 3, 5, 7, 9): Synthesis, characterization, and reactivity. *Accounts of Chemical Research*, 50(6): 1468–1479, May 2017. ISSN 1520-4898. doi: 10.1021/acs.accounts.7b00164. URL http://dx.doi.org/10.1021/acs.accounts.7b00164.

Deborah Wrege. bseels of carbon materials. Master's thesis, Department of Physics and Astronomy, University of Heidelberg, 2022.

Hanfei Yan and Yong S. Chu. Optimization of multilayer laue lenses for a scanning x-ray microscope. *Journal of Synchrotron Radiation*, 20(1):89–97, November 2012.

ISSN 0909-0495. doi: 10.1107/s0909049512044883. URL http://dx.doi.org/10.1107/S0909049512044883.

Zuozhao Zhai, Lihui Zhang, Tianmin Du, Bin Ren, Yuelong Xu, Shasha Wang, Junfeng Miao, and Zhenfa Liu. A review of carbon materials for supercapacitors. *Materials and Design*, 221:111017, 2022. ISSN 0264-1275. doi: https://doi.org/10.1016/j.matdes.2022.111017. URL https://www.sciencedirect.com/science/article/pii/S0264127522006396.

Wen-Shan Zhang, Maik Matthiesen, Benjamin Günther, Jakob Wensorra, Daniel Fischer, Lutz H. Gade, Jana Zaumseil, and Rasmus R. Schröder. Visualizing the active paths in morphologically defective organic thin-film transistors. *Advanced Electronic Materials*, 7(11), August 2021. ISSN 2199-160X. doi: 10.1002/aelm.202100400. URL http://dx.doi.org/10.1002/aelm.202100400.

Xinming Zhang, Xi Cen, Rijuta Ravichandran, Lauren A Hughes, and Klaus van Benthem. Simultaneous Scanning Electron Microscope Imaging of Topographical and Chemical Contrast Using In-Lens, In-Column, and Everhart-Thornley Detector Systems. *Microscopy and Microanalysis*, 22(3):565–575, 05 2016. ISSN 1431-9276. doi: 10.1017/S1431927616000751. URL https://doi.org/10.1017/S1431927616000751.

Weilie Zhou, Robert P. Apkarian, Zhong Lin Wang, and David Joy. Fundamentals of scanning electron microscopy. *Scanning microscopy for nanotechnology*, pages 1–40, 2006.

Y. Zhu, H. Inada, K. Nakamura, and J. Wall. Imaging single atoms using secondary electrons with an aberration-corrected electron microscope. *Nature Materials*, 8 (10):808–812, September 2009. ISSN 1476-4660. doi: 10.1038/nmat2532. URL http://dx.doi.org/10.1038/nmat2532.

# G Acknowledgements

This work would not have been possible without the persistent support of many people around me, whom I want to give a special thank you:

- To my supervisor Rasmus R. Schröder, who gave me the opportunity to work in this project, supported me in all questions and showed great patience with me and my extensive hobbies.
- To Irene Wacker, who supported this work in many ways, especially with the preparation of different samples and discussion of the experiments.
- To Ronald Curticean, who became my companion on the campus from the beginning of my time in the group and a close friend, helping me in all regards.
- To all group members during my time in the group discussing projects and contributing to the results: Jochen Kammerer, Jörg Eisele, Götz Hofhaus, Wolfgang Köntges, Wen-Shan Zhang, Lukas Berner, Deborah Wrege, Giorgi King, Franz Schmidt-Kaler, Felicitas Franke, Lukas Bange, Frederick Georgius.
- To the organization of the excellence cluster '3dmm2o' for accepting me in the graduate school, for all events and retreats and the funding of my work by the Deutsche Forschungsgemeinschaft (DFG, German Research Foundation) under Germany's Excellence Strategy via the Excellence Cluster 3D Matter Made to Order (EXC-2082/1-390761711).
- To my cluster mentoring committee Martin Wegener, Kerstin Göpfrich and Dario Mager for feedback and advice during my work.
- To Zeiss Microscopy, most notably Bernd Schindler and Michael Schnell who supported in all questions concerning the microscope.
- To Wolfram Pernice for accepting to be the second referee of this thesis and to Petra Tegeder and Arthur Hebecker for accepting to be examiners.
- Last but not least to my family and friends, for keeping me on track and distracting me in the right moments.

Erklärung:

Ich versichere, dass ich diese Arbeit selbstständig verfasst habe und keine anderen als die angegebenen Quellen und Hilfsmittel benutzt habe.

Heidelberg, den 26.04.2024 ....................................................